UNIVERSITY OF CALIFORNIA, MERCED

Atomistic Study of Ternary Oxides as High-Temperature Solid Lubricants

A dissertation submitted in partial satisfaction of the requirements
for the degree Doctor of Philosophy

in

Mechanical Engineering

by

Hongyu Gao

Committee in charge:

Prof. Ashlie Martini, Advisor

Prof. Gerardo C. Diaz

Prof. Yanbao Ma

Prof. Erin R. Johnson

2016

The Dissertation of *Hongyu Gao* is approved, and it is acceptable in quality and form for publication on microfilm and electronically:

Ashlie Martini (Advisor)	Date
Gerardo C. Diaz	Date
Yanbao Ma	Date
Erin R. Johnson	Date

University of California, Merced

2016

This dissertation is dedicated to my parents, my wife, and my lovely son.

Acknowledgments

I would like to express my deepest appreciation to my advisor, Dr. Ashlie Martini, for the patient guidance and mentorship she provided to me over the past four years. She walked me into the world of *Tribology*, letting me experience the beauty of this subject. Without her support and mentoring, I would not be stepping on the path of becoming a research scientist from a graduate apprentice. What I learned from her is far beyond knowledge in tribology, but an attitude of how to do research and a spirit of dedication in scientific research. Here, I would also like to convey my appreciations to my committee members, Drs. Gerardo Diaz, Erin Johnson and Yanbao Ma, for the friendly guidance, thought provoking suggestions that each of them offered to me.

In addition, I would like to convey my gratitude to my extraordinary collaborators, Drs. Samir Aouadi, Erin Johnson, Thomas Scharf, Christopher Muratore, D'Arcy Stone, Alberto Otero-de-la-Roza, Chirawat Chantharangsi, Chutima Paksunchai, Hamidreza Mohseni, Maia Bischof, David Jaeger and Ms. Jingjing Gu, for the technical supports from either experimental or first-principles theory aspect on the main project during my Ph.D. Likewise, I would like to recognize Drs. Wilfred Tysoe, Gary Doll, Gerardo Diaz, Bin Zhao, Jun Qu, Yalin Dong, Chang Ye, Danny Perez, Philip Egberts, Chun Tang, Dustin Olson and *et al.* as great collaborators for those side projects that I have worked or have been working on during the past few years. I would also like to appreciate the valuable suggestions from and pleasant discussions with former and current group members of Martini Research Lab: Drs. Chun Tang, Taeil Yi, Yalin Dong, Xiawa Wu, and Zhijiang Ye, Xiaoli Hu, Uma Ramasamy, Michelle Len, Duval Johnson and Sean Lantz. I also had great time while assisting undergraduates in our micro-tribology lab on summer projects with Matthew McDaniel, Gregory Rozema, Jose Garcia, Shelby Skelton, Cory Mercer and Julio Dos Santos.

I acknowledge supports by the Air Force Office of Scientific Research (AFOSR) award No. FA9550-12-1-0221 and the National Science Foundation under Grant Numbers CMMI-1265742 and CMMI-1265594. Also, I appreciate the awards or fellowships titled: *Chinese Government Award for Outstanding Self-Financed Student Abroad* from the China Scholarship Council; the *Graduate Dean's Dissertation Year Fellowship* from University of California-Merced (UC Merced) Graduate Division; the *STLE Young Tribologist Award* from Society of Tribologists and Lubrication Engineers (STLE); the *STLE Northern California Research Scholarship* from STLE Northern California Section; and other forms of financial supports from UC Merced. Also, I appreciate all kinds of supports from the Mechanical Engineering Department, Instructional Lab and Stem Cell Instrumentation Foundry at UC Merced. Special thanks to Drs. Tao Ye and Vincent Tung for their generous supports with their lab facilities.

Finally, I would thank my GREAT wife and parents for their enormous sacrifices in shouldering the parenting and household burdens while I pursued this final degree.

Abstract

Atomistic Study of Ternary Oxides as High-Temperature Solid Lubricants

by

Hongyu Gao

Doctor of Philosophy in Mechanical Engineering

University of California, Merced

2016

Professor Ashlie Martini, Advisor

Friction and wear are important tribological phenomena tightly associated with the performance of tribological components/systems such as bearings and cutting machines. In the process of contact and sliding, friction and wear lead to energy loss, and high friction and wear typically result in shortened service lifetime. To reduce friction and wear, solid lubricants are generally used under conditions where traditional liquid lubricants cannot be applied. However, it is challenging to maintain the functionality of those materials when the working environment becomes severe. For instance, at elevated temperatures (i.e., above 400 °C), most traditional solid lubricants, such as MoS_2 and graphite, will easily oxidize or lose lubricity due to irreversible chemical changes. For such conditions, it is necessary to identify materials that can remain thermally stable as well as lubricious over a wide range of temperatures.

Among the currently available high-temperature solid lubricants, Ag-based ternary metal oxides have recently drawn attention due to their low friction and ability to resist oxidation. A recent experimental study showed that the Ag-Ta-O ternary exhibited an extremely low coefficient of friction (~0.06) at 750 °C. To fully uncover the lubricious nature of this material as a high-temperature solid lubricant, a series of tribological investigations were carried out based on one promising candidate – silver tantalate ($AgTaO_3$). The study was then extended to alternative materials, Cu-Ta-O ternaries, to accommodate a variety of application requirements. We aimed to understand, at an atomic level, the effects of physical and chemical properties on the thermal, mechanical and tribological behavior of these materials at high temperatures. Furthermore, we investigated potassium chloride films on a clean iron surface as a representative boundary lubricating system in a non-extreme environment. This investigation complemented the study of Ag/Cu-Ta-O and enhanced the understanding of lubricious mechanisms of solid lubricants in general. Molecular dynamics (MD) simulations was used as the primary tool in this research, complemented by density-functional theory and experiments from our colleagues.

In this research, we first developed empirical potential parameters for $AgTaO_3$ and later Cu-Ta-O ternaries using the modified embedded-atom method (MEAM) formalism. With those parameters, we explored the sliding mechanisms of $AgTaO_3$, $CuTaO_3$ and $CuTa_2O_6$ at elevated temperatures. Particularly on $AgTaO_3$, we investigated the effects of applied loads as well as surface

terminations on friction and wear as functions of temperature. In addition, to optimize the tribological performance of $AgTaO_3$, film reconstruction mechanisms were investigated on Ta_2O_5/Ag films with varying amounts of Ag. For the potassium chloride-iron system, we studied the effect of contact pressure on interfacial structure, based on which the origin of the commonly observed pressure-dependent shear strengths was explored. We hope this research will benefit the design and development of solid lubricant materials for a wide range of applications.

Contents

List of Figures

List of Tables

Chapter 1

Introduction

1.1 Solid Lubricants

1.1.1 At High Temperature

For dynamic components, working performance and stability are very important. This is a challenge for any component, but particularly so in extreme environments. For example, satellites in the vacuum of space are exposed to moisture during launch as well as large temperature fluctuations. Under these severe conditions, material properties at the contact region are critical. In most tribological applications, liquid or grease lubricants are used to decrease friction and wear primarily by velocity accommodation between surfaces in relative motion by shearing of the oil molecules across the solid-liquid-solid interface [5–7]. However, most liquid lubricants will evaporate at high temperatures, which may lead to failure of the lubricated component since losing lubricating substance may lead to increase of friction and wear. Furthermore, decomposition products of oils at elevated temperatures can build up at interfaces and inhibit lubrication effects in a process referred to as coking [5]. In addition, liquid lubricants may not be appropriate in applications where the liquid can settle due to migration from aging (dormancy) leaving some parts unprotected before high-temperature operation.

Solid lubricants, on the other hand, can be utilized for high-temperature applications to reduce friction and wear where traditional liquid lubricants cannot be applied. Vapor pressure of solid lubricants is low and, hence, sublimation does not contribute to the degradation of the system components. However, many traditional solid lubricants will easily oxidize or lose function at elevated temperatures (i.e., above 400 °C) [8]. Therefore, remaining thermally stable and lubricious over a wide range of temperature are necessities for solid lubricants used in high-temperature environments. To qualify as an effective solid lubricant, the friction coefficient needs to be < 0.2 in most applications. An irreversible deformation of the contact surfaces is likely to occur for friction values in excess of 0.2. A very common application for solid lubricants is moving components that operate at high temperatures; such conditions are common in a variety applications including aerospace equipment, tooling, materials-forming, and nuclear power industries [9–14]. Two examples of applications of particular interest to high-temperature friction reduction are: (1) air foil bearings for high mach aerospace engines and (2) high-speed machine tools. Both applications involve different loading profiles with times up to minutes prior to contacts for the bearings, with intermittent high loading and high pass frequency in comparison to constant high-speed contact with relatively low

loads for machine tools.

Solid lubricants can be classified in a number of ways in terms of their crystal structures, chemical compositions, application scopes and etc. According to the role of working environments in triggering lubricity, solid lubricants could be divided into [5, 15]: (1) *intrinsic* lubricants, which possess an atomic structure that shears easily to facilitate interfacial sliding (e.g., MoS_2 and soft metals); and (2) *extrinsic* lubricants, which require the influence of an additive from the surroundings to activate a low shear mechanism (e.g., friction on graphite significantly decreases as it exposes in a high-humidity environment). Most *intrinsic* and *extrinsic* solid lubricants that operate at low temperatures (25 to 300 °C or so) cease to be lubricious at higher temperatures (> ~300 °C) since they oxidize and become abrasive, and hence, lose their lubricity. In general, solid lubricants can be classified into the following sub-categories in terms of their material characteristics:

(1) lamellar solid lubricant;
(2) lubricious oxides, fluorides, and sulfates;
(3) diamond-like carbon and diamond;
(4) soft materials;
(5) polymers;
(6) composites.

Among these sub-categories, metal oxides, fluorides and soft metals plastically deform and/or form low-shear-strength surfaces at elevated temperatures. They are, however, not lubricious at relatively low temperatures and researchers have combined them with low-temperature lubricants to create chameleon coatings that adapt their surface during temperature cycling from 25 to 1000 °C to reduce friction in this temperature range [5, 6, 14, 16–18]. In this chapter, we briefly introduce three categories of these materials, i.e. lamellar solid lubricants, oxides and soft materials, since the mechanisms by which these types of material functions are relevant to the focus of this research.

1.1.2 Lamellar Solid Lubricants

Lamellar solid materials are widely used solid lubricants in industry and well studied by scientists [13]. The representative materials in this class are transition-metal dichalcogenides (e.g. MoS_2), graphite, HBN and H_3BO_3, which all have layer-like crystal structures. Atoms lying on the same layer are closely packed and strongly bonded to each other. While, the layers themselves are relatively far apart, and the forces that bond them (e.g. van der Waals) are weak. During sliding, these parallel layers slide over one another with relatively low friction. In addition, strong interatomic bonding and packing in each layer is thought to help reduce wear damage [19]. This mechanism is largely responsible for low friction and is essential for long life. However, certain chemical adsorbates are able to affect shear in most solids. For example, transition-metal dichalcogenides provide low friction coefficients in dry and vacuum environments [20, 21]. When sliding in humid air, dangling or unsaturated bonds on the edge of basal planes react with moisture and oxygen in the environment leading to higher friction and eventual failure [22]. In addition, the lubricity of graphite depends strongly on the presence of certain condensable vapors since the adsorbed mass further weakens the interlayer bonding resulting in the easy shear and transfer of the crystalline platelets of the material onto the mating surfaces [23, 24].

1.1.3 Soft Materials

Certain pure metals (e.g., In, Sn, Pb, Ag, Au, Pt, Sn, etc.) are soft materials that can provide low friction on sliding surfaces because of their low shear strengths and rapid recovery from strain hardening as well as recrystallization [13, 14, 25]. They are used mainly as solid lubricants because of the unique properties they possess. For example, in addition to its soft nature, silver has excellent electrical and thermal conductivity, oxidation resistance, good transfer-film-forming tendency, and a relatively high melting point [5]. Soft metals are generally produced as thin films on surfaces to be lubricated. Film-to-substrate adhesion is extremely critical for achieving long wear life or durability, and the thickness of the soft metallic films also plays a major role in both friction and wear [26]. Also, the friction coefficients of most soft metals tend to decrease as the ambient temperature increases, mainly because of additional softening and rapid recovery from strain hardening. Highly thermally conductive films like silver are able to decrease wear rate at the sliding interface mainly because frictional heat is dissipated rapidly from the sliding interface. Silver and other soft metallic coatings can also protect the sliding surfaces against environmental and/or tribochemical degradation under dry and oil-lubricated sliding contact conditions [27, 28]. One of the major shortcomings of metallic solid lubricants is that most of them react with sulfur and chlorine (if present in the operating environment) and they may undergo rapid corrosive wear [29]. In addition, to avoid immediate loss from the contact, a process such as ion-plating is necessary that ensures adequate adhesion to the substrate surfaces [30].

1.1.4 Oxides

For applications at temperatures above 500 °C, it is unrealistic to expect materials to resist oxidation for prolonged times and most of the lamellar solids lose their lubricity and become useless [5]. Thin oxide films that form on the sliding surfaces may, in turn, determine the fiction and wear behavior of these interfaces. Therefore, studies of the shear rheology of lubricious oxides have been carried out. Certain oxides (e.g., Re_2O_7, MoO_3, PbO, B_2O_3, NiO, $CaSO_4$, $BaSO_4$, and $SrSO_4$) become soft and highly shearable at elevated temperatures and hence can be used as lubricants [10, 31]. The easy-shearing feature of those oxides can be attributed to (1) screening of cations by surrounding anions (crystal chemical model) [32, 33], (2) material softening that occurs when the working temperature is between 0.4 and 0.7 of the absolute melting point (T_m), which corresponds to the brittle-to-ductile transition of most oxides [34], (3) melting of the oxide by exceeding T_m [35], (4) creation of a material with a lamellar crystal structure with weak inter-planar cohesive bonds (similar to the shear mechanism that occurs in graphite and molybdenum disulfide) [36], (5) shearing in textured nanocrystalline grains due to dislocation glide resulting in intra-crystalline slip [37, 38]. When applied as coatings, these solids can provide acceptable levels of friction coefficients and long wear life. Mixed oxides (e.g., CuO-Re_2O_7, CuO-MoO_3, PbO-B_2O_3, PbO-MoO_3, CoO-MoO_3, Cs_2O-MoO_3, NiO-MoO_3) can provide wider operational ranges and can be prepared as alloys or composite structures to provide longer durability. At high temperatures, as the oxide layer is depleted from the surface by wear, the alloying ingredients diffuse toward the surface where the oxygen potential is higher; they oxidize again to replenish the consumed lubricious layers that have low shear strength and/or surface energy to decrease friction [39]. On the other hand, Magnéli phases are a homologous series of transition metal compounds with formula Me_nO_{2n-1}, Me_nO_{3n-1}, or Me_nO_{3n-2} (Me–metal) that have planar lattice faults. It has been suggested that Magnéli phases are principally the result of tribo-oxidation and that, once formed, they can dominate the tribological

behavior of sliding ceramic interfaces, mainly because of their unique shear properties [40–43].

1.2 Ternary Metal Oxides

Oxides exhibit a full spectrum of electronic, optical, and magnetic behavior: insulating, semiconducting, metallic, superconducting, ferroelectric, pyroelectric, piezoelectric, ferromagnetic, multiferroic, and nonlinear optical effects [44]. The unparalleled variety of physical properties of oxides holds great promise for many applications in optics, magnetism, and electronics. Among oxides, those that possess layered crystal structure offer additional functionality since they inherently display anisotropic properties as a result of their non-symmetrical crystal structure. A significant number of layered oxides that have been synthesized so far belong to the ABO_3 structural family known as perovskites [44]. The perovskite structure can accommodate by substitution some 30 elements on the A site and over half the periodic table on the B site [44]. The flexibility of their structural skeleton offers a great opportunity to create new materials with designed functionality.

The initial candidate for high-temperature applications in this research is a subset of perovskites called intrinsically layered ternary metal oxides. In addition to having desirable bulk material properties, layered ternary oxides were recently shown to exhibit superior temperature behavior with low friction coefficients (0.1–0.3) when tested at temperatures > 400 °C [34, 35, 45–47]. The target material of this research must be simple and sufficiently well defined to enable accurate and realistic atomistic models, yet also have been shown to have potential for real high-temperature applications. Based on these criteria, we focused on silver tantalate, $AgTaO_3$. Recently, $AgTaO_3$ was reported to exhibit an extremely low coefficient of friction (CoF = 0.06) at 750 °C [48].

1.3 Review of $AgTaO_3$

Until recently, material studies on the tribological properties of $AgTaO_3$ have been very limited. Previously, this was because of challenges with material synthesis and high cost [49]. Recently, though, synthesis issues have been addressed by the development of simple processing routes involving only conventional solid-state reaction and sintering in an environment with a high oxygen pressure [50]. Also, although tantalum remains a relatively expensive material, its market price has decreased in recent years due to competition from other materials (ceramics, aluminum, niobium) and because device miniaturization has led to the need for less material in its most common applications [49]. The removal of these synthesis and cost barriers has lead to increased interest and research into the properties and applications of silver tantalate.

Crystallographic measurements of $AgTaO_3$ were reported by Francombe and Lewis in 1958 [51]; its basic crystal structure is shown in figure 1.1. Then in the 1980s, a series of studies were performed that yielded structural parameters with more accuracy and over a wider range of temperatures; two of these from 1987 are still widely cited today [1, 52] (reference to the complete set of papers by these groups is available in a recent review [49]). These studies reported a low-temperature rhombohedral phase with transitions to monoclinic, then tetragonal and finally cubic. At present, it is believed that the material is rhombohedral until 685 K, monoclinic from 650 to 703

K, tetragonal from 685 to 780 K and cubic above 780 K [50]. Note the coexistence of multiple phases – rhombohedral and monoclinic from 650 to 685 K, and monoclinic and tetragonal from 685 to 703 K – means that exact transition temperatures are not well defined.

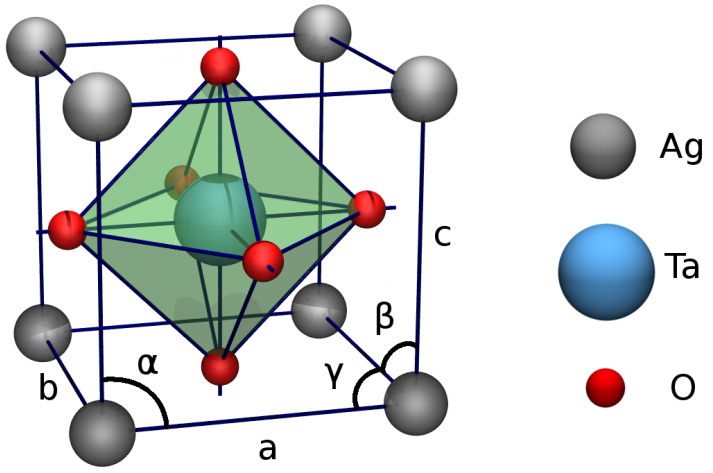

Figure 1.1: Cubic-like approximation to the perovskite crystal structure of $AgTaO_3$. At low temperatures, the octahedron shown twists relative to its neighbors, leading to a lower-symmetry structure. On heating, the depicted structure is recovered. (This figure was provided by our colleagues *A. Otero-de-la-Roza and E.R. Johnson*)

Apart from crystal structure measurements, there have been very few experimental studies of silver tantalate alone (although more research activity has focused on the solid solution silver tantalate-niobate; see, for example, [53, 54]). Isolated silver tantalate studies have been centered on the subtleties of the temperature-dependent structural phase changes and the dielectric properties of the material. For example, application of uniaxial pressure to the crystal resulted in changes to the material's dielectric properties, based on which it was hypothesized that pressure decreases the distance between ions which can shift the phase transition temperature [55]. In another example, it was found that the phase transition from rhombohedral to monoclinic is soft-mode dependent, which indicated that the transition involves only rotation of oxygen octahedra (shaded green region shown in figure 1.1) [50]. However, studies on tribological properties of $AgTaO_3$ can rarely be found. To study this material as a high-temperature solid lubricant, computational modeling is used in this research, and will be introduced in the following.

1.4 Atomic-Scale Modeling

Computational modeling and simulations play an important role in the study of solid lubricants because they provide a means of fundamentally understanding experimental observations and also enable predictions to be made for properties and phenomena not easily measured experimentally. Further, computational approaches offer a means of identifying trends to guide experiments, since it is not possible or advisable to experimentally examine all potential oxide candidates and all their crystal structures. Realistic modeling of complex materials systems is now possible due to the rapid increase of readily-available computational power and the development of new algorithms.

Generally speaking, model-based tools for predicting friction and wear in solid-solid contacts include finite element (see for example [56]), thermodynamic (see for example [57]), empirical (see for example [58]) and atomistic (see for example [59]) methods. The first three of these are typically applied at the component/interface scale and so are ideal for capturing macroscopic phenomena. The limitation of such models is that they rely on existing knowledge of material properties and, in some cases, parameters fit from an experiment. To our knowledge, they have not been applied specifically to describe the sliding behavior of metal oxide solid lubricants in high-temperature environments. An alternative is atomistic simulation, in which models explicitly describe the atomic structure of a given material. This approach provides a fundamental understanding of how the structure/chemistry of a material is related to its behavior in a sliding interface and so can lead to atomic-level design of solid lubricants. Two of the mostly widely-used modeling approaches in these studies are density-functional theory (DFT) and molecular dynamics (MD) simulation. DFT is an approach based on quantum mechanics that is widely recognized as a powerful tool for the study of material properties at the atomistic/electronic level. In this research, MD simulations will be the primary tool used and discussed in detail next.

Molecular dynamics simulation describes the dynamic behaviors of moving atoms in successive configurations of a system [60]. The trajectory of each particle varies with time according to Newton's laws of motion. Atomic interactions are governed by semi-empirical potential energy functions (also called force fields) in terms of material electronic and mechanical properties that can be obtained from first-principles calculations or experiments. Such models enable prediction of the dynamic properties of larger (on the order of hundreds of nanometers) and more complex systems. This provides a means of investigating many relevant tribological properties (e.g. friction and wear) on length scales accessible to some experimental methods [61]. However, the range of applicability of MD is restricted by the need for high quality interatomic potentials, which limits the number of materials systems that can be explored. This issue can be partially addressed by *ab initio*, or first-principles molecular dynamics, which integrates the dynamics of MD with the accuracy of DFT [62, 63]. The other significant issue of MD in terms of tribology research is its time scale, which, due to the femtosecond time step, limits the total simulation time to nanoseconds. As the development of computer technology and computing algorithm, however, these issues will be resolved. In general, by using MD, we can obtain information about material properties and gain a better understanding of the mechanisms underlying tribological behaviors.

1.5 MD Modeling of Oxide Solid Lubricants

Oxides are important materials that have received a tremendous increase in interest in the research community due to their thermal stability and inertness. In the last two decades, they have been proposed and studied as high-temperature solid lubricants. Many oxides are abrasive at low temperature but shear more easily at higher temperatures due to oxide softening or by control of grain size and defect structure. Researchers have discovered new designs and mechanisms that allow them to create effective solid lubricants at elevated temperatures. Atomistic modeling of binary and ternary oxides as coating materials will be reviewed in this section.

1.5.1 Binary Oxides

Binary oxide coatings can be loosely divided into two categories: lubricious materials with low shear resistance and hard materials with high wear resistance. The most common low shear binary oxide coatings are Magnéli phases. Most of these materials have been studied using DFT and focused on calculation of binding energies, vibration frequency, and surface stability [40–42]. Such studies provide insights on the mechanistic relationship between the structure and the static properties of the materials, but cannot predict their dynamic response to loading or shear. This issue can be addressed by MD simulations. However, currently, MD-based studies of the response of Magnéli phase materials to normal and shear stresses have been limited to TiO_2. Simulations of TiO_2 in contact with a nanoscale probe revealed that strong adhesive forces result in the probe snapping into contact with the surface [64]. Simulations of more severe loading during indentation of TiO_2 showed the resulting surface wear was dependent on the crystal surface orientation [65]. That model was then extended to slide the nanoscale probe laterally across the surface and predicted that the friction coefficient, between 0.28 and 0.38, was independent of the TiO_2 polymorph (note that this range is larger than expected of low friction solid lubricants on larger length scales because the contribution of adhesion is more significant in nano-scale contacts) [65].

Next, we discuss hard coatings. To complement the studies of surface terminations of hard coatings, MD-based simulations have been developed to explicitly model the sliding alumina interface. Many of these have focused on the effect of sliding speed on friction and revealed that speed not only affects the magnitude of friction but the mechanisms underlying sliding resistance and the associated energy dissipation [66–69]. Other studies showed that friction of alumina is affected by normal load [66], commensurability of the two surfaces [68, 70], surface stiffness [71], and the degree of hydroxylation [69]. There are also a few other binary hard oxide coatings that have been the subject of computational studies of note are MgO and SiO_2. MD simulation of the contact between a nanoscale probe and a MgO surface revealed strong adhesive forces leading to the characteristic snap-to-contact [72] and provided insight into the relationship between adhesive hysteresis and energy dissipation [73, 74]. Most modeling studies of SiO_2 have focused on its role as a substrate material for another coating [75] or self-assembled monolayers [76–78].

In general, computational modeling has lagged behind experimental efforts in understanding the tribological properties of binary oxides. Many DFT-based efforts have provided new understand of their structure and static properties, but MD studies that can capture dynamics have been more limited. However, with the availability of more and better potentials for these materials, such as recently-developed parameter sets for the ReaxFF force field for the vanadium [79], aluminum [80]

and silicon [81] oxides, we anticipate that more MD-based studies will be performed in the future.

1.5.2 Ternary Oxides

Computational studies on tribological properties of ternary oxides are even less common than those of binary oxides. This may, in part, be due to the lack of empirical potentials. The complexity and time required to develop a new potential increases dramatically with the number of elements in the structure so there are few potentials available for these important materials. To avoid this issue, *ab initio* MD simulations were used to investigate high-temperature tribological performance of $Ag_2Mo_2O_7$ and Ag_2WO_4 [36]. It was found that dispersed Ag and Ag_2 fragments moved closer to each other and formed large linear clusters at temperatures near the melting point. These simulations provided new understanding of the important role of silver and bond strength, but were limited to relatively small sizes and times.

There have been no prior computational studies on the tribological properties of $AgTaO_3$. Investigation of silver tantalate using model-based methods has been limited to a small number of first-principles studies used to characterize electric and optical properties [82, 83]. However, such studies are restricted to very small-scale, static systems. To address this issue, empirical models are often introduced so that MD simulation can be used to make predictions about the dynamic properties and evolution of larger systems. In recent years, a number of MD-based studies have been performed on other perovskite materials which predicted various thermophysical, thermomechanical and transport properties quite successful [84–88]. The ability of MD to make accurate predictions relies on using an interatomic potential function that faithfully represents the material. Until now, however, no such function has been available for $AgTaO_3$.

1.6 Research Objectives

In this research, the lubricious nature of ternary oxide $AgTaO_3$ as a high-temperature solid lubricant is explored computationally using molecular dynamics simulation. The objective is to understand, at an atomic level, the physical and chemical properties that influence the thermal, mechanical and tribological behavior of this material. We carry out a systematic investigation to provide the fundamental understanding that is needed to enable $AgTaO_3$ to fulfill its tremendous potential for high-temperature applications. Molecular dynamics simulation is used to explore the physical/chemical properties of this material and understand the underlying lubricating mechanisms. The ultimate goal of this research is to apply the newly acquired fundamental knowledge to enable design of novel materials for high-temperature applications. Specific research objectives include:

(1) develop and validate a predictive atomic-scale model of $AgTaO_3$;
(2) characterize the material response to thermal, mechanical and tribological stresses;
(3) investigate how the chemical and structural evolution of the material imparts its function;
(4) use this understanding to optimize the high-temperature performance of $AgTaO_3$;
(5) explore alternative materials to accommodate various high-temperature applications;
(6) fully understand the lubricating mechanisms via complimentary study of a boundary lubricating system in a non-extreme environment.

1.7 Scope of This Dissertation

This dissertation consists of ten chapters. In Chapter 1, we generally introduced solid lubricants and discussed the target material of this research in specific, followed by a review of previous modeling work on binary/tenary oxides. From Chapter 2 to Chapter 7, we summarize the accomplished research outcomes for this project. Specifically, we (a) developed empirical potential parameters for $AgTaO_3$ (Chapter 2), (b) explored the sliding mechanisms for this material (Chapter 3), (c) investigated load-dependent tribological behaviors (Chapter 4), (d) characterized surface termination dependence of chemical and tribological properties (Chapter 5), (e) studied material composition effects (Chapter 6), and (f) explored alternative materials, i.e. Cu-Ta-O ternaries (Chapter 7). In Chapter 8 and 9, we focus on a model boundary lubricating system—potassium chloride films on iron substrate—based on which the pressure-induced interfacial structural variation (Chapter 8), and the effect of contact pressure and lattice structure on shear strength (Chapter 9) were explored. Finally, in Chapter 10, several research topics are proposed as future study.

Chapter 2

MEAM Parameter Fitting

2.1 Introduction

To computationally study $AgTaO_3$ as a high-temperature solid lubricant, we decided to develop empirical potential parameters specifically for this material in terms of the modified embedded-atom method (MEAM) formalism [3]. It is important to note that MEAM does not explicitly include ionic charges which implies that using it to model $AgTaO_3$ will require ionic bonding to be captured in an effective way through parametrization. However, there is evidence that this is possible based on MEAM potentials successfully developed for the Si-O-Au ternary [89] and Al_2O_3 [90]. The lack of explicit treatment of ionic bonding does introduce some limitations for the fitted potential. However, as we will show in this section, the MEAM potential can be parametrized for $AgTaO_3$ and reproduce properties obtained from first-principles calculations and experimental measurements.

Density-functional theory calculations were performed to predict material structure and energetics, and then the MEAM parameters were fit so that the empirical potential yields matching results (DFT results were provided by our colleagues *A. Otero-de-la-Roza and E.R. Johnson*). We started with reference binary structures, i.e. AgO and TaO, and fit the potential parameters to DFT-predicted lattice structure, elastic constants and cohesive energy. Then, using the fitted binary parameters, additional parameters were adjusted for the ternary $AgTaO_3$ to enable the empirical potential to reproduce DFT-predicted lattice structure, elastic constants, cohesive energy and equation of state. The fit potential parameters were further validated by MD prediction of thermal expansion that was found to be consistent with experimental measurements.

2.2 Methodology

2.2.1 MEAM Potential

The modified embedded-atom method is a semi-empirical interatomic potential that incorporates angular dependency of electron density into the embedded-atom method [3]. The total energy E of a system of atoms in the MEAM is approximated as the sum of the atomic energies

$$E = \sum_i E_i, \tag{2.1}$$

where i is the i^{th} atom in the system. The energy of atom i consists of the embedding energy and the pair potential terms:

$$E_i = F_i(\bar{\rho}_i) + \frac{1}{2}\sum_{j\neq i}\phi_{ij}(r_{ij}). \tag{2.2}$$

F is the embedding function, $\bar{\rho}_i$ is the background electron density at the site of atom i, and $\phi_{ij}(r_{ij})$ is the pair potential between atoms i and j separated by a distance r_{ij}. The embedding energy $F_i(\bar{\rho}_i)$ represents the energy cost to insert atom i at a site where the background electron density is ρ_i. MEAM has been used to describe a large number of different single element and binary systems (for a recent summary of available parameters, see [91]) and a few ternaries [92–97]. The potential developed in this work was based on the MEAM formulation given in [98]; the complete set of mathematical expressions underlying this version of MEAM is reported in the appendix of reference [98].

The MEAM parameters that need to be fit for the reference (B1) binary structures are: relative density ρ_0, cohesive energy E_c, nearest-neighbor distance r_e, and the exponential decay factor α. The exponential decay factor α is the following function of cohesive energy, bulk modulus B and atomic volume Ω: $\alpha = \sqrt{\frac{9\Omega B}{E_c}}$. In this work, the cohesive energy, nearest-neighbor distance, bulk modulus and atomic volume were obtained from DFT calculations. The only remaining parameter, ρ_0, was obtained by adjusting the ratio of the relative density of two elements, e.g. ρ_0^{Ag}/ρ_0^{O}, until the elastic constants predicted using the empirical potential were consistent with those obtained from DFT. The parameters for AgO and TaO were fitted using this approach.

For the ternary, we could not simply combine the single element potentials as with the binary structures. To obtain the desired properties for silver tantalate, we fitted the binary parameters for the immiscible Ag-Ta (discussed later). Also available are the ternary screening parameters C_{min}(Ag,Ta,O) and C_{max}(Ag,Ta,O) which consider an O atom screening the Ag-Ta pair. These parameters were adjusted until the model could reproduce the lattice structure, elastic constants and cohesive energy predicted for the ternary by the DFT calculations.

2.2.2 MD Simulation

The crystal structures, elastic constants and thermal expansion were computed using open source molecular modeling software LAMMPS [99]. The initial atomic configuration of the binaries was the reference B1 structure with primitive vectors $\vec{A_1} = \frac{1}{2}a\vec{y} + \frac{1}{2}a\vec{z}$, $\vec{A_2} = \frac{1}{2}a\vec{x} + \frac{1}{2}a\vec{z}$ and $\vec{A_3} = \frac{1}{2}a\vec{x} + \frac{1}{2}a\vec{y}$, where a is the lattice constant, and basis vectors $\vec{B_1} = 0$ and $\vec{B_2} = \frac{1}{2}\vec{A_1} + \frac{1}{2}\vec{A_2} + \frac{1}{2}\vec{A_3}$. Snapshots of the AgO and TaO structures are shown in figure 2.1(a) and (b), respectively. The initial structure of the silver tantalate was obtained from DFT and contains 40 atoms (8 Ag, 8 Ta and 24 O); the atomic configuration is shown in figure 2.1(c). Periodic boundary conditions were imposed in all directions. The cohesive energy and lattice structure for a given set of MEAM parameters were obtained by energy minimization using the conjugate gradient algorithm. To calculate the elastic constants, we performed zero static internal and external stress approximations, in which the size and shape of the system varied during the iterations such that the final configuration reached a local potential energy minimum.

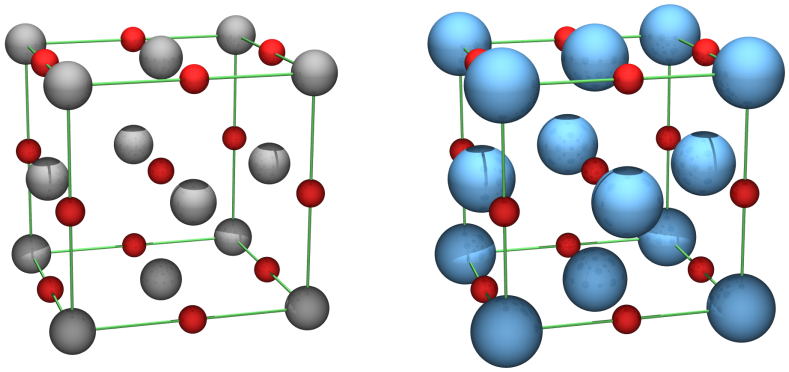

(a) (b)

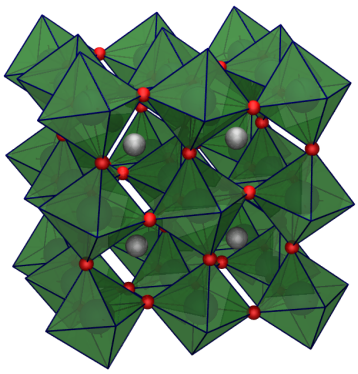

(c)

Figure 2.1: Snapshots of (a) AgO, (b) TaO, and (c) $AgTaO_3$. Atoms are identified by color: Ag (grey), Ta (blue), and O (red).

Properties predicted for a given set of MEAM parameters (cell length, angle, elastic constants and cohesive energy) were compared directly with the DFT results. The error was defined by:

$$\delta_i = \frac{1}{3}\lambda_{(L)} \sum_{m=1}^{3} |L_m^c - L_m^e| + \frac{1}{3}\lambda_{(A)} \sum_{n=1}^{3} |A_n^c - A_n^e| + \frac{1}{6}\lambda_{(C)} \sum_{p=1}^{6} |C_p^c - C_p^e| + \lambda_{(E_c)} |E_c^c - E_c^e|, \qquad (2.3)$$

where δ_i is the i^{th} observable error of the system where superscripts c and e denote the calculated (*i.e.* from MD simulation) and expected (*i.e.* from DFT) values. L_m, A_n and C_p denote the lattice constants (a_0, b_0 and c_0), angles (α, β and γ) and elastic constants (C_{11}, C_{12}, C_{13}, C_{14}, C_{33} and C_{44}), respectively. For perfect fitting, δ should be equal to zero. Equation (2.3) also contains weighing

factors for each observable, $\lambda = \lambda_{(L)} + \lambda_{(A)} + \lambda_{(C)} + \lambda_{(E_c)} = 1$, to enable more or less significance to be placed on the accuracy of a given parameter. We found $\lambda_{(L)} = 0.4$ for lattice constants, $\lambda_{(A)} = 0.1$ for angles, $\lambda_{(C)} = 0.2$ for elastic constants and $\lambda_{(E_c)} = 0.3$ for cohesive energy to be optimal values for guiding the fitting process toward ideal parameters.

Thermal expansion was predicted using MD simulation in the NPT (constant number of atoms, pressure and temperature) ensemble with a time step of 1 fs. Pressure and temperature control were maintained using a Nosé-Hoover barostat/thermostat with damping constants of 10 ps and 0.1 ps, respectively. The pressure was held at 1 atm and the temperature was varied between 50 and 450 K. The system was allowed to equilibrate for 2 million timesteps at each temperature, with properties averaged over the last 500,000 timesteps.

2.3 Results and Discussion

2.3.1 Parameter Fitting

The potential parameters for the pure Ag and Ta bulk phases were taken to be those reported previously [3]. The only difference was the exponential decay constants for the oxygen which had to be adjusted to be able to reproduce the experimental diatomic spring constant [100]. The new MEAM parameters developed for oxygen are $\alpha = \beta^{(0)} = \beta^{(1)} = \beta^{(2)} = 4.59$, where α is the exponential decay for the universal energy function and the βs describe the exponential decay for the atomic densities (see [3] for detailed information about these parameters). MEAM parameters for pure Ag, Ta and O and the MEAM-predicted properties of fcc Ag and bcc Ta are provided in table A.1 and table A.2 in Appendix A.1.

Four MEAM parameters were fit for each binary system: equilibrium distance (r_e), cohesive energy (E_c), exponential decay constant (α) and relative density (ρ_0). The reliability of the binary potentials was evaluated by comparing the lattice constant (a), cohesive energy (E_c), bulk modulus (B) and elastic constants (C_{11} and C_{12}), with the relevant DFT data. The cut-off distance within which pairwise interactions is computed was set to 6.2 Å, which is larger than the second nearest-neighbor distance in $AgTaO_3$ [94]. The fitting results are shown in table 2.1. Since we were specifying a, E_c and B through the MEAM parameters (r_e, E_c and α, respectively), those parameters were predicted exactly. The remaining parameters, the elastic constants, were fit with less than 1 % error.

Figure 2.2 shows the equations of state for the bulk metal phases (Ag and Ta) and binary systems (AgO and TaO) predicted by the MEAM potential and from DFT. The potential captures the energetics of these systems quite well near the energy minimum. Since the focus on this effort was on parameterizing MEAM for $AgTaO_3$, we did not attempt to optimize the binary potential parameters for cases far from equilibrium.

For $AgTaO_3$, the existing binary parameters were fixed and parameters for the undetermined Ag-Ta alloy system were identified by fitting the physical properties of the ternary system from DFT. The mutual solubility of Ag and Ta in the liquid state is limited and in the solid state is negligibly small [101]. This is captured in the MEAM potential by setting the heat of formation ΔH_{B1}

Table 2.1: Properties of B1 structure binaries from MD simulation with fitted MEAM potential and from DFT calculations (Details of DFT calculations are provided in Appendix A.2).

	Ag-O			Ta-O		
	MEAM	DFT	Diff (%)	MEAM	DFT	Diff (%)
a (Å)	4.548	4.548	0.00	4.404	4.404	0.00
E_c (eV)	-3.38	-3.38	0.00	-7.24	-7.24	0.00
C_{11} (GPa)	224.55	222.71	0.82	351.74	351.74	0.62
C_{12} (GPa)	156.80	155.39	0.90	269.56	267.75	0.67
B (GPa)	177.84	177.83	0.00	295.02	295.02	0.00

for the Ag-Ta pair to any negative number. The other parameters for Ag-Ta were adjusted to fit the $AgTaO_3$ properties to DFT. Specifically, ρ_0^{Ag}/ρ_0^{Ta}, r_e^{AgTa} and α^{AgTa} were varied with no adverse affect on the fitted binaries parameters. To extend from binaries to ternaries, MEAM also provides ternary screening parameters C_{min} and C_{max}. These were set to 2.0 and 2.8, respectively, for all atom pair combinations. The magnitude of the screening parameters was consistent with those for other material combinations [98] and we found no additional adjustments were necessary to obtained the desired level of fitting. The full set of MEAM parameters for Ag-O, Ta-O and Ag-Ta optimized to describe $AgTaO_3$ is given in table A.3 in Appendix A.1.

Table 2.2 shows the properties predicted by the fit empirical potential and DFT. Referring to equation (2.3), the averaged differences between MD simulation and DFT are: 1.25 % for lattice constants, 1.67 % for angles, 2.11 % for cohesive energy (magnitude difference 0.13 eV), and 10.45 % for elastic constants. Figure 2.3 shows the MD and DFT-predicted equation of state (EOS). The potential does a good job near equilibrium. Away from equilibrium there is some deviation which is consistent with the error in the predicted elastic constants in table 2.2. These results indicate that care must be taken when applying this potential to nonequilibrium systems.

2.3.2 Model Predictions

To further validate the fitting parameters, we performed MD simulations on the 40-atom $AgTaO_3$ system at varying temperatures. Initially, the analysis was limited to the temperature range in which the material is expected to remain in a single structural phase (i.e. 100 to 500 K where the structure is rhombohedral) so the lattice constants will vary smoothly with temperature. As the temperature increased, figure 2.4 shows that the potential energy and volume increased approximately linearly. We also observe that the variations in volume caused by thermal effects are well within the range where the MD and DFT data overlap in figure 2.3, i.e. ≈ 1 % deviation around the equilibrium volume. This suggests that the fitted potential parameters should be able to capture the physics of the material in the temperature range of interest.

To compare the model predictions to experiment, we calculated the thermal expansion at

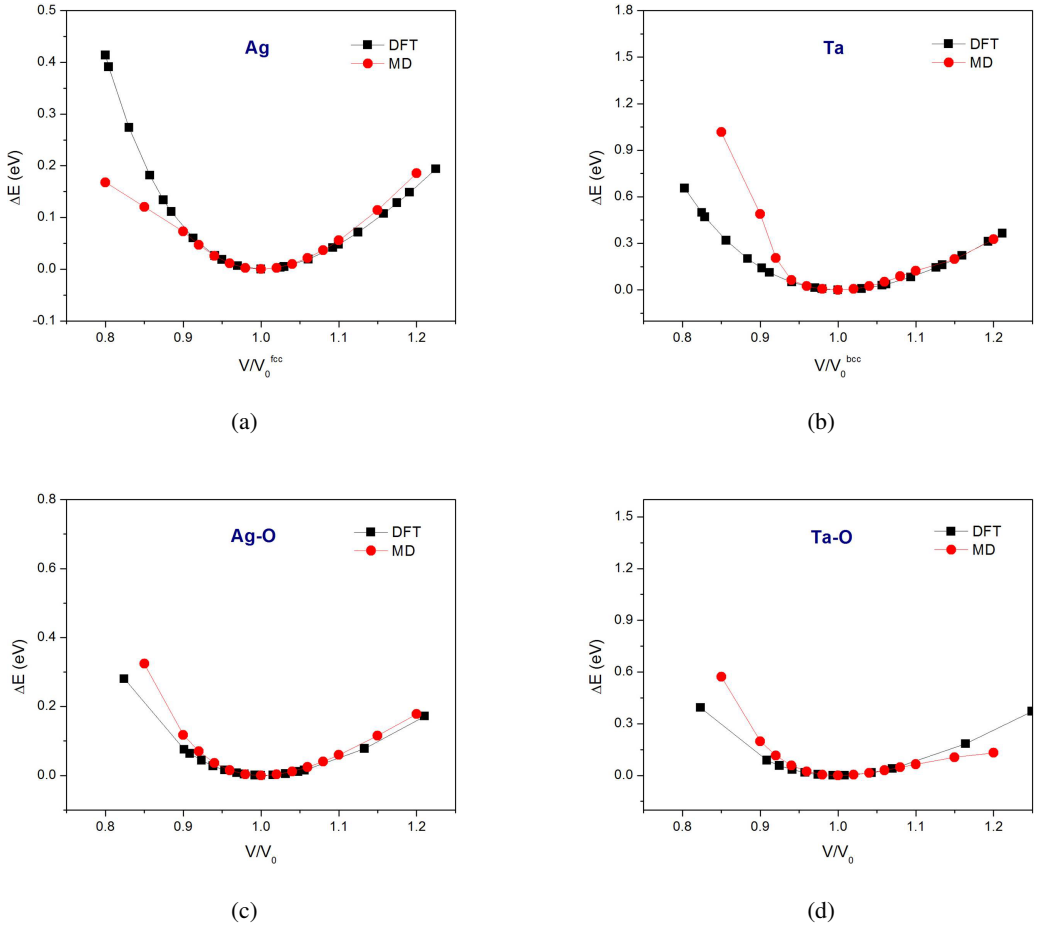

Figure 2.2: Equation of state for (a) fcc Ag, (b) bcc Ta, (c) AgO and (d) TaO where ΔV is the energy relative to the ground state.

constant pressure as $(L_T - L_{100K})/L_{100K}$, where T is temperature, L_T is the average of the three quasi-cubic crystal side lengths (a, b and c) at temperature T, and L_{100K} is the average side length at a reference temperature of 100 K. The results, shown in figure 2.5, are consistent with experimental values [1].

2.4 Conclusions

We have developed parameters for $AgTaO_3$ based on the MEAM empirical potential formalism. First, the MEAM parameters for AgO and TaO were fitted based on the structural and elastic properties of the materials in the B1 reference structure predicted by DFT. The empirical potential was able to reproduce the first-principles predictions. For $AgTaO_3$, the existing binary parameters were fixed and parameters for the undetermined Ag-Ta alloy system were fitted based on the physical properties of the ternary system from DFT. The empirical potential predicted the crystal structure

Table 2.2: Structural properties of $AgTaO_3$.

Parameters		MEAM	DFT
Lattice Constants (Å)	a	7.638	7.761
	b	7.633	7.761
	c	7.801	7.761
Angle (°)	α	89.90	88.75
	β	90.55	88.75
	γ	90.32	88.75
Cohesive Energy (eV)	E_c	-6.16	-6.29
Elastic Constants (GPa)	C_{11}	347.82	336.47
	C_{12}	96.10	157.48
	C_{13}	173.38	177.12
	C_{14}	35.36	35.29
	C_{33}	300.56	286.54
	C_{44}	65.51	75.43

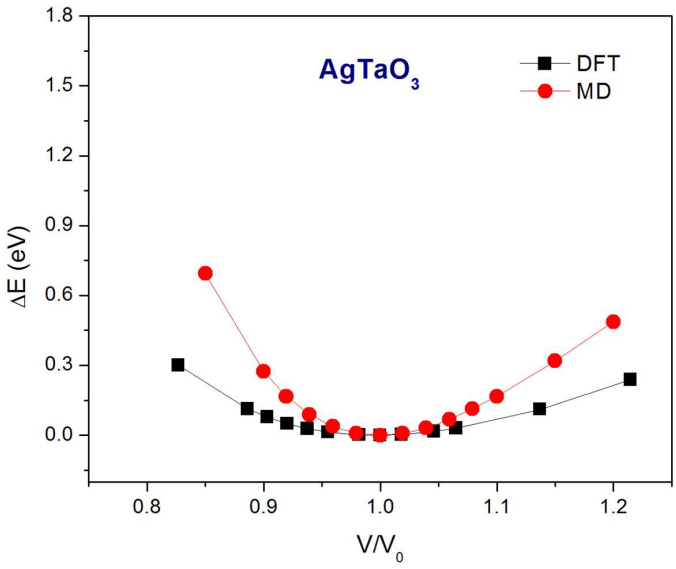

Figure 2.3: Equation of state for $AgTaO_3$ from MD and DFT where ΔV is the energy relative to the ground state.

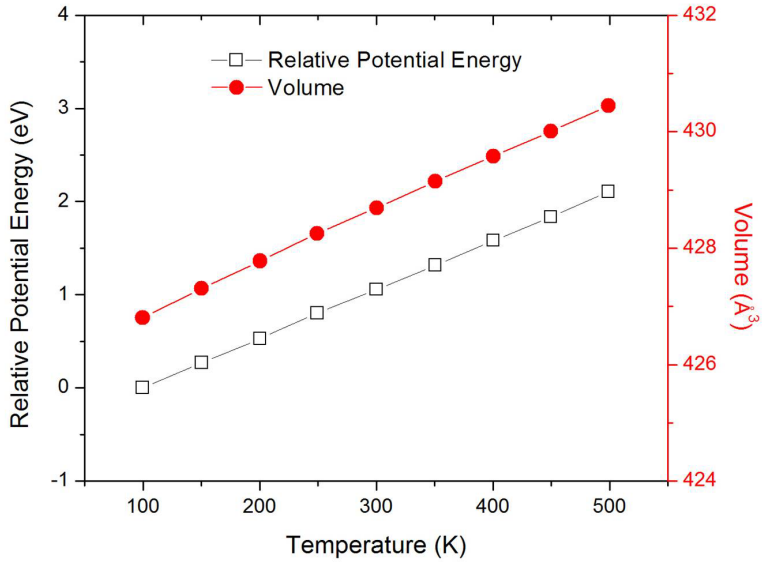

Figure 2.4: Increase of the time-averaged potential energy (hollow squares) and volume (filled circles) predicted by the MD simulation using fit MEAM parameters. The energy is relative to that at 100 K.

and cohesive energy very accurately and made satisfactory predictions for the elastic constants. The equation of state matched DFT calculations closely near the energy minimum, but some deviation was observed away from equilibrium indicating that this potential is most appropriate for modeling systems near equilibrium. Finally, the thermal expansion of $AgTaO_3$ was predicted by a molecular dynamics simulation using the newly developed potential parameters and found to be very consistent with experimental measurements.

As mentioned in the *Introduction*, MEAM is likely to have some limitations for $AgTaO_3$ because its functional form does not explicitly include ionic charges. Significant shortcomings of the potential may include, for example, the inability to capture magnetic properties, polarization and etc. We also recommend that the current model be applied only at lower pressures, specifically those near atmospheric pressure at which it was parameterized. Regardless, as shown in this section, the material's major structural and thermal characteristics are described well by the developed model and the parameter set can be used in future molecular dynamics and molecular statics simulations of $AgTaO_3$ within the range of conditions for which it was fit.

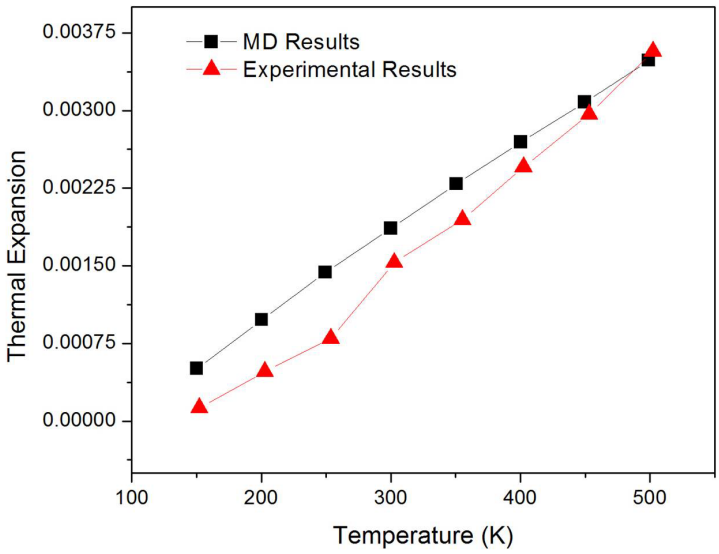

Figure 2.5: Temperature dependent-strain of silver tantalate predicted using MD with the fit MEAM potential (squares) and measured experimentally (triangles) using X-ray diffraction [1].

Chapter 3

Investigation of Sliding Mechanism of $AgTaO_3$

3.1 Introduction

Silver tantalate, with melting temperature of 1172 °C [49], was recently shown to exhibit an extremely low CoF of 0.06 at 750 °C [48]. It was suggested that the friction reduction was due to the formation of a lubricious $AgTaO_3$ phase that decomposed into Ta_2O_5 and Ag phases during interfacial sliding to form a tribofilm. In this chapter, we focus on discussing the friction-induced surface reconstruction and its role in reducing friction at high temperatures. MD results on the sliding tribological properties of $AgTaO_3$ tribofilm are reported. With the help of experimental observations (the experimental results are provided by our colleagues *D.S. Stone, H. Mohseni, S.M. Aouadi and T.W. Scharf*), we try to explain the sliding mechanisms for this material.

3.2 Methodology – Sliding Model

MD simulation was used to model a rigid plate sliding against a silver tantalate ($AgTaO_3$ perovskite crystal structure) film (shown as figure 3.1). The dimensions of the film were 6 × 4 × 15.5 nm^3 and it contained 32400 atoms. A normal load of 451.9 nN was uniformly distributed on the plate. The bottommost atomic layer of the film was fixed throughout the simulation. The motion of the atoms in the four layers immediately above the fixed bottom layer was damped to ensure a smooth transition from the large shear at the top to the stationary bottom of the simulation cell. The magnitude of the damping was decreased with increasing distance from the bottom layer (damping coefficients decreased from 0.0064 to 0.0016 $nN{\cdot}s{\cdot}m^{-1}$). Periodic boundary conditions were applied in the plane of sliding. Simulations were performed at four different temperatures (27, 350, 500, and 750 °C) where the temperature was maintained using a Langevin thermostat. The top plate moved laterally at a constant speed of 5 m/s with timestep of 1 fs. The simulation was run for 16 ns such that the total displacement of the top plate in the sliding direction was 80 nm. The onset of motion was followed by instability and the high sliding resistance characteristic of static friction. Therefore, reported friction values were obtained by averaging the simulation data from the last 40 nm of sliding. All atomic interactions were described by the MEAM with potential parameters developed specifically for $AgTaO_3$ in Chapter 2.

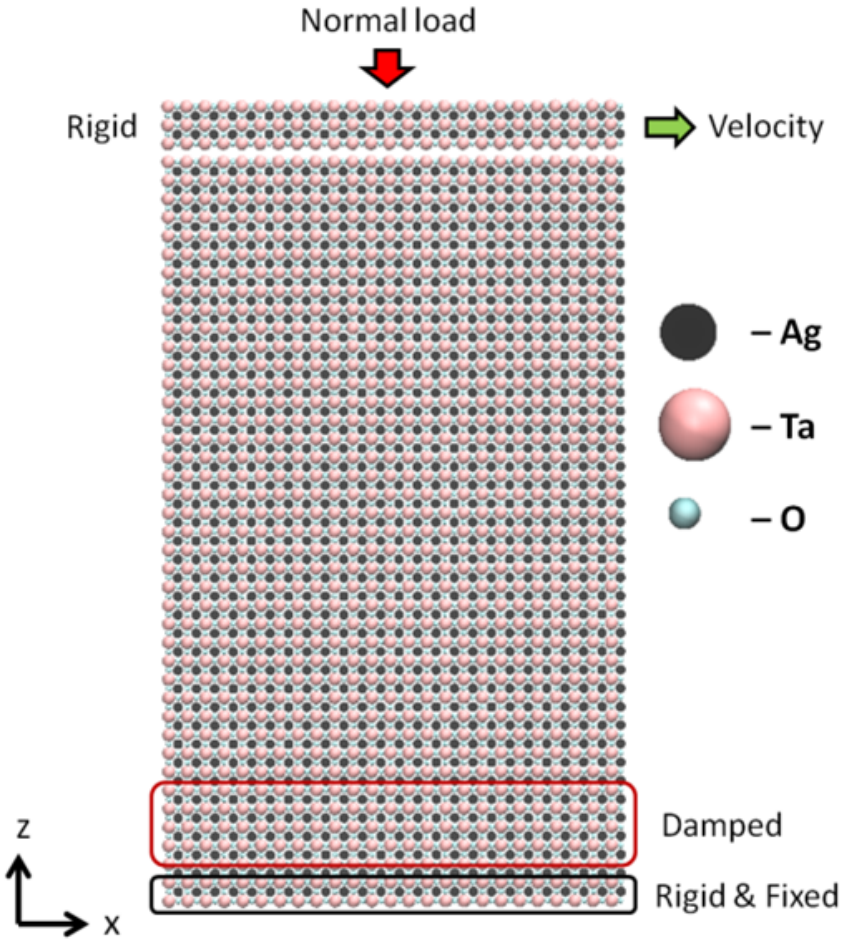

Figure 3.1: Snapshot of $AgTaO_3$ tribofilm setup.

3.3 Results and Discussion – Friction & Sliding Mechanism

Figure 3.2 shows experimentally-measured and simulation-predicted frictional forces as functions of temperature ranging from 27 to 750 °C. Both model and experiment show that friction decreases with temperature, and that minimum friction is observed at the highest temperature of 750 °C. The discrepancy in the magnitude of the frictional force is due to the inherent size-scale difference between the two techniques. Specifically, the model contact area is nanoscale while the contact area in the experiment is on the order of tens to hundreds of microns. The model and experimental applied loads differ by orders of magnitude as well which is indirectly due to size since Newton-scale loads cannot be applied to a nanometer-scale contact. Regardless, the similarity of the friction trends and the evolution of the tribofilm (discussed next) indicate that the simulation is indeed cap-

turing the dominant mechanisms underlying the temperature-dependent friction of $AgTaO_3$.

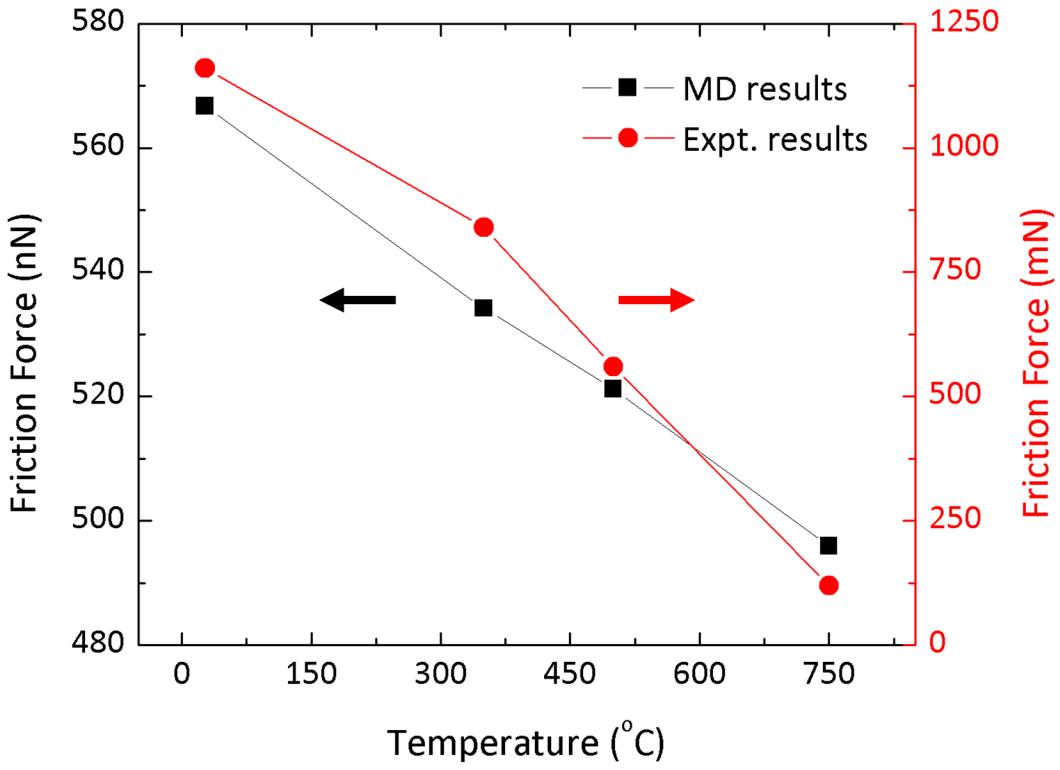

Figure 3.2: Model-predicted (black squares; left y-axis) and experimentally-measured (red circles; right y-axis) friction forces on $AgTaO_3$. Note that the units of force on the two y-axes differ by several orders of magnitude.

To understand the mechanisms of high-temperature friction, bright field transmission electron microscope (BFTEM) was used to analyze the structural and tribochemical (chemistry induced by sliding) changes in the surface and sub-surface regions. It was previously suggested that reduced friction may be due to the existence of a tribofilm that forms during sliding with the potential for reconstruction of $AgTaO_3$ through the friction process [48]. Figure 3.3(a) shows a cross-sectional BFTEM image taken inside the wear surface. An electron beam Pt (e-Pt) layer was deposited on the surface prior to forced ion beam (FIB)-milling to protect against Ga ion beam damage. From this image, we can clearly identify structural and tribochemical changes that occurred in this tribofilm during sliding at 750 °C; near the surface, there are Ag clusters surrounded by Ta_2O_5 while the $AgTaO_3$ remains intact further away from the sliding interface. The segregation of silver is reasonable since the Ta-O bond is much stronger than the Ag-O bond [5, 82] and the latter can easily break at high temperatures [5]. In addition, based on the image in figure 3.3(a), and others not shown, the residual coating thickness after sliding, including the tribofilm, is $\sim$ 440 nm (from an original coating thickness of $\sim$ 2 μm). Figure 3.3(b) is a snapshot of a simulation of $AgTaO_3$ at 12 ns and

750 °C. The image reveals that silver atoms (in grey) are not distributed uniformly; instead, they group together to form clusters (circled in yellow) and are predominately surrounded by tantalum and oxygen, both of which corroborate the aforementioned experimental observations. Far from the surface, the $AgTaO_3$ structure is more predominant, also in agreement with figure 3.3(a). These findings from both experiments and simulations suggest surface reconstruction leading to formation of Ag and Ta_2O_5 phases plays a significant role in reducing friction at high temperatures.

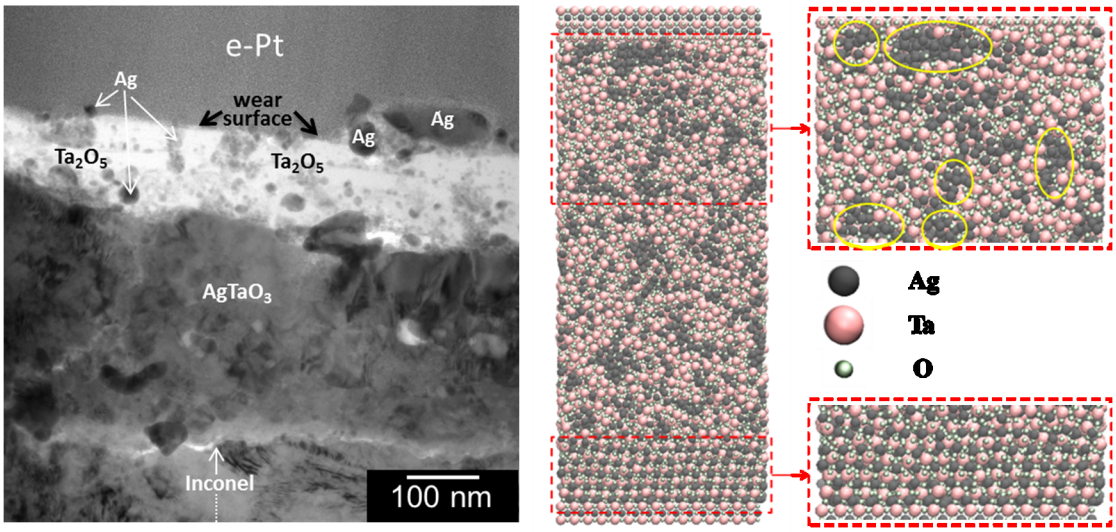

Figure 3.3: Cross-sectional BFTEM image of various chemical phases taken inside the center of wear surface after 750 °C. (b) Snapshot from a simulation at the same temperature after 12 ns of sliding (Ag – grey, Ta – pink, and O – white). Snapshots on the right highlight the tribofilm near the sliding interface that exhibits silver clusters encircled in yellow (top) and predominantly unchanged material far from the surface (bottom).

To provide further evidence of the connection between the observed surface reconstruction in the tribofilm and low friction, we calculate the local density distribution in the simulation to quantify the presence and evolution of silver clusters during sliding. Specifically, we divide the model film into cubes with side length of 0.5 nm (3262 cubes in total). By calculating the number and type of atoms in each cube, we can determine the quantity of high-density silver cubes (identified as cubes with at least 70 % silver) at each simulation timestep. This approach also allows us to calculate the average size of silver clusters (regions with multiple adjacent high silver density cubes). The results are shown in figure 3.4. At the beginning of each test, no high-density cubes exist because the entire film is crystalline $AgTaO_3$ (in which the silver density is 20 %). As the top plate moves laterally and the normal load is applied, the number of high silver density cubes gradually increases. Although this trend is observed at both 27 and 750 °C, it is more significant at the higher temperature. This is consistent with the images in figure 3.3 where identifiable Ag clusters are observed for sliding tests at 750 °C. We also measure the average volume of each silver cluster and, as shown in figure 3.4,

the silver clusters in the 750 °C case are consistently larger (approximately two times larger) than those in the simulation at 27 °C.

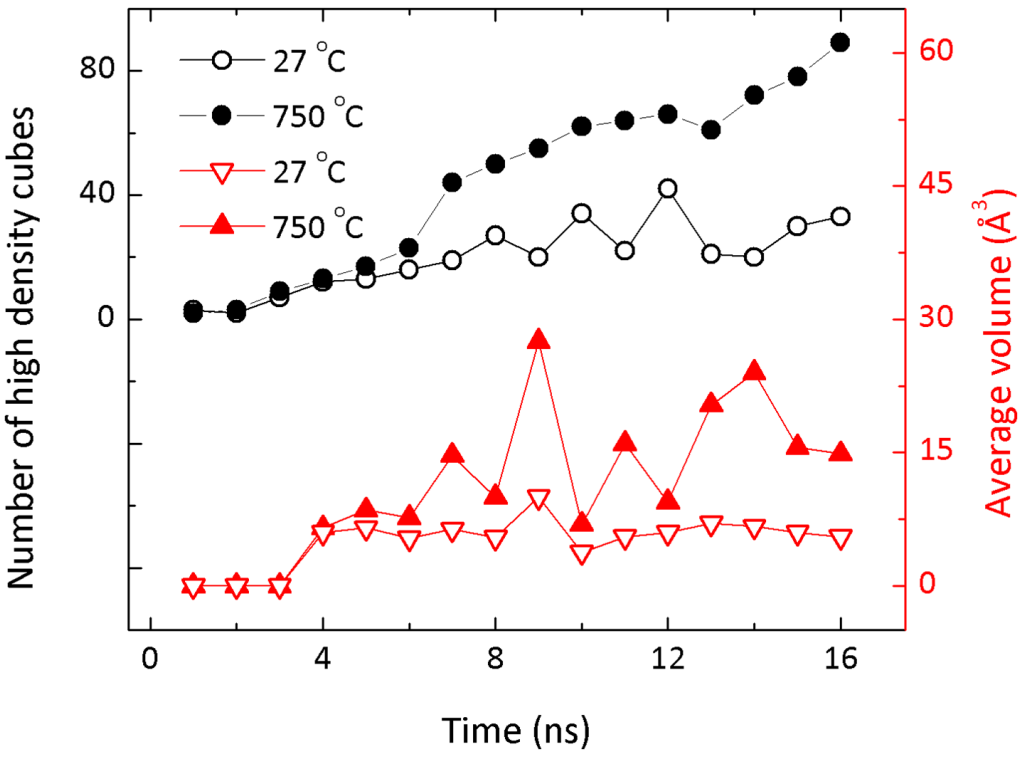

Figure 3.4: Number of high-density Ag cubes (black circles) and the average volume of multi-cube clusters (red triangles) at different temperatures (solid – 750 °C and hollow – 27 °C) obtained from MD simulations.

The results presented thus far show that friction decreases with increasing temperature (simulation and sliding experiments), silver clustering with surrounding Ta_2O_5 is present near the sliding surface (simulation and BFTEM image), and the number and volume of silver clusters increase with sliding distance at higher temperature (simulation). Collectively, these results suggest that there is a connection between the presence of the tribofilm and low friction at high temperatures observed for $AgTaO_3$. We next consider the mechanisms underlying this connection. It has long been known that elemental silver can act as a low interfacial shear film over a range of temperatures [102]. In addition, Ag has proven useful as a low-to-moderate-temperature solid lubricant phase in composite coatings [45, 102, 103]. Further, previous MD simulations have shown that soft nanoparticles in a harder matrix are deformed easily under sliding conditions [104]. It is reasonable that the silver clusters observed in the tribofilm are facilitating sliding at high temperatures. The aggregation of these silver clusters in the tribofilm may be driven by several different mechanisms. It has been suggested that coarsening of Au nanoparticles in the subsurface worn regions of MoS_2 nanocomposite coatings

is related to phenomena such as mechanical mixing [105], the motion of vortices [104, 106, 107], and diffusion-driven Ostwald ripening [108]. Similar mechanisms may underlie our observations of the growth of soft Ag nanoparticles (similar structure and hardness to Au). Although we cannot at this point determine the exact nature of the process, our findings suggest that a combination of thermal and tribomechanical stresses are required.

While the silver appears to be a key feature of the near-surface material enabling low friction sliding, we believe that the Ta_2O_5 and $AgTaO_3$ phases observed in figure 3.3(a) contribute to the overall performance of the coating as well. The limitation of using elemental silver on its own is that its relatively low hardness (on the order of 0.5 GPa from reference [109]) allows ploughing and excessive material transfer to the counterface [102]. The hardness of Ta_2O_5 is on the order of 10 GPa [110], suggesting the material can provide structural rigidity and wear-resistance. In addition, $AgTaO_3$ has a stable structure formed by the oxygen octahedra in its crystal structure, which is likely to contribute to the overall structural rigidity of the coating. Therefore, our findings indicate that the constituents of the tribofilm work together such that Ta_2O_5 and $AgTaO_3$ provide structure and resistance to deformation-induced friction while Ag clusters act as a lubricious phase that yields low interfacial friction.

3.4 Conclusions

In conclusion, the sliding resistance of $AgTaO_3$ at different temperatures was investigated by both MD simulation and experimental methods. Both methods showed the lowest friction forces were achieved at 750 °C. Excellent agreement was also observed with the formation of a tribofilm of Ag clusters and surrounding Ta_2O_5 during high-temperature sliding. As the temperature increased, more Ag clusters were formed in the tribofilm, also the average volume of these clusters became larger. These findings appear to be correlated to the friction behavior of $AgTaO_3$. In this chapter, the study of sliding behavior of $AgTaO_3$ tribofilm could be helpful to the understanding of high-temperature sliding mechanisms of this material.

Chapter 4

Load Dependence of Friction

4.1 Introduction

Applied load plays an important role in determining tribological behavior of materials in sliding contact. According to the classic Amontons' 1^{st} Law, friction is found to change linearly with the applied load. As load increases, the rise of friction and wear can be attributed to larger contact area induced adhesive force increase. Later on, Bowden and Tabor proposed a non-linear friction-load dependence (i.e. $F = L^{2/3}$) for single asperity contact model based on Hertzian elastic theory [111]. From macro to nano, load effect tends to be increasingly rely on the mechanical and chemical characteristic of the contact counterfaces [112, 113]. The objective of this research is to investigate the effect of load on the tribological properties of $AgTaO_3$ coatings. More specifically, the elemental and phase composition and the crystal structure are investigated to understand the changes that occur in these coatings as a result of the application of various loads during the sliding process. This study significantly extends previous work on a promising high-temperature solid lubricant by characterizing and providing mechanistic insight into its behavior under different operating conditions. In this chapter, experimental results are provided by our colleagues *D.S. Stone, C. Chantharangsi, C. Paksunchai, M. Bischof, D. Jaeger, T.W. Scharf and S.M. Aouadi*.

4.2 Methodology – Load Dependence of Sliding Model

The simulation process was similar to that in Chapter 3 and can be simply described as a rigid plate sliding over a $AgTaO_3$ tribofilm. This rigidity assumption means that the plate does not represent a real material and we found that model-predicted trends were unaffected by its atomic composition. The dimensions of the film were $9.7 \times 1.94 \times 15.52$ nm^3 and it contained 25375 atoms. The top rigid plate moved laterally at a constant speed of 5 m/s for 8 ns with a timestep of 1 fs. A schematic of the simulation setup is shown in figure 3.1. Normal loads ranging from 500 to 3000 nN (with an interval of 500 nN) were uniformly distributed on the top plate. The sliding tests were performed at two different temperatures, 27 and 750 °C. Results were obtained by averaging the data from the last 20 nm of sliding, excluding data during the initial, unstable stages of sliding.

4.3 Results and Discussion – Friction, Clustering & Film Density

MD simulations predicted that friction force increases with normal load at 750 °C as shown in figure 4.1. Here we show friction force instead of CoF because the simulations only capture part of the wear process at the higher loads. Specifically, the model atoms redistribute but cannot leave the periodic simulation cell such that removal of Ag from the wear track observed experimentally (and the likely source of the increasing CoF with load as shown in figure 4.2) does not occur in the model. The simulations also provided information at 27 °C which can be used for comparison and so facilitates understanding of the high-temperature measurements. We observe in figure 4.1 that both the friction force and the average friction coefficient (slope of a linear fit) at 750 °C are much smaller than those at 27 °C for all loads. In the case of nanoscale interactions, the relationship between friction force and normal load cannot be simply described by Amontons' Law due to the significant effect of adhesion. By extrapolating the data, we find that the friction force at zero load (and therefore the adhesion) is smaller at the higher temperature.

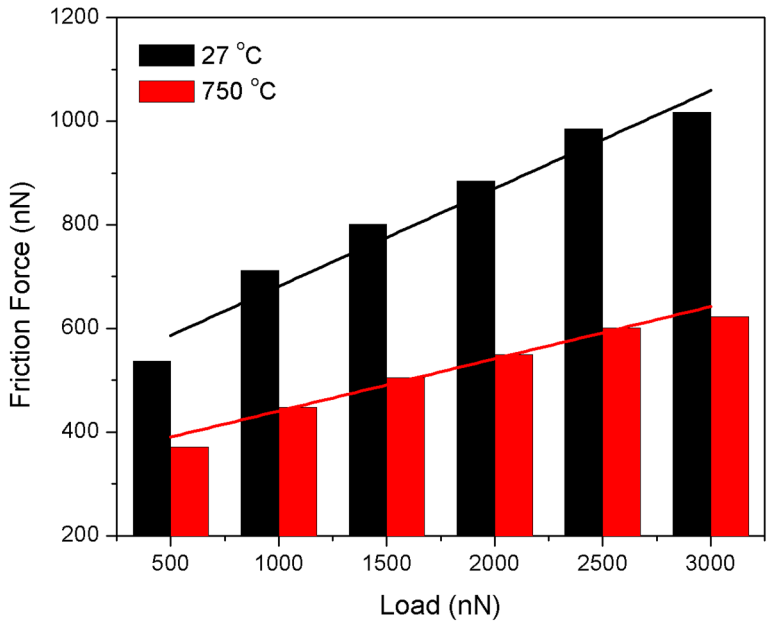

Figure 4.1: Model-predicted friction force as a function of normal load at 27 and 750 °C. The straight lines represent linear fits to the data at each temperature.

We previously suggested that the temperature dependence of $AgTaO_3$ is due to sliding- and temperature-induced structural change that provides the tribofilm with low shear resistance [48]. Specifically, experiments and simulations showed that groups of silver atoms formed at the sliding interface. Note that the number of Ag atoms in the simulation does not change, i.e. the clusters are formed from the Ag atoms initially present in the $AgTaO_3$ film. As described in the previous section, we divided the film into identical cubes with side length of 0.5 nm and identified high-

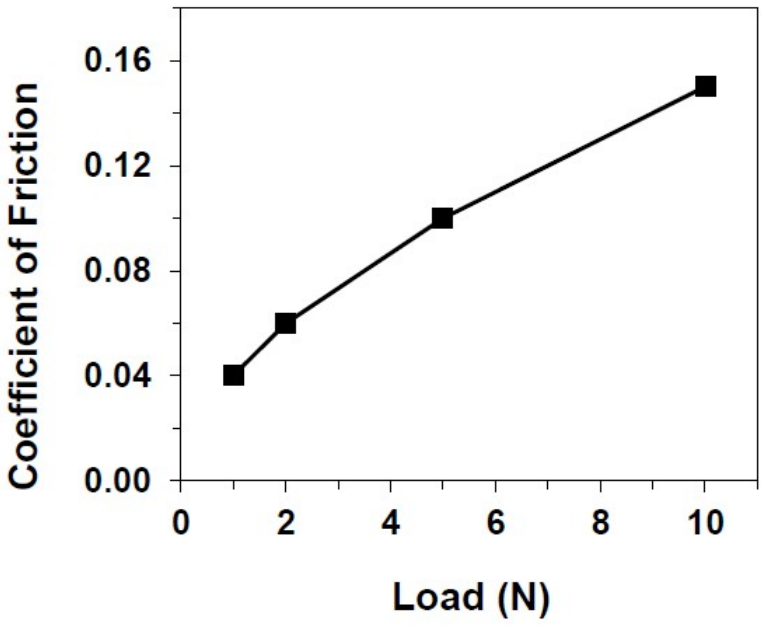

Figure 4.2: Experimentally-predicted steady-state CoF for silver tantalate as a function of load tested at 750 °C (this result is provided by our colleagues *D.S. Stone, C. Chantharangsi, C. Paksunchai, M. Bischof, D. Jaeger, T.W. Scharf and S.M. Aouadi*).

density Ag cubes, N, as cubes consisting of more than 70 % Ag atoms. Figure 4.3 shows that N increases with time and temperature at all loads. In addition, the results indicate that, in general, N decreases with normal load; this trend is particularly evident at the end of the simulation (8 ns) and more pronounced at the higher temperature. To correlate the silver clustering with friction force, we measured the shear stress for each cube. The distribution of high-density silver cubes at 1000 nN load and 750 °C is shown in figure 4.4 as a function of normalized stress, where stress is normalized by the maximum value. This shows that highest density silver regions correspond to the lowest shear stress in the simulation cell which supports the suggestion that silver segregation and clustering plays a role in enabling low friction. The results shown in figure 4.4 are representative of our observations for other loads and temperatures.

The results we have shown here (and in Section 3.3) strongly support the hypothesis that increasing temperature results in decreased friction due to the increased segregation of silver atoms and the low shear resistance those atoms provide. However, looking more closely at figure 4.3, this does not appear to be the only mechanism for load dependence. Especially at the lower temperature, the number of silver clusters is not significantly lower at the higher load where we observe higher friction. To explain the load dependence, we instead consider the porosity of the film. This is suggested by our TEM results that increasing load resulted in less silver and lower porosity [114]. Although the relationship between load and porosity is not direct, we can correlate a decrease of the model-predicted average density to an increase in porosity. We quantify porosity as the average den-

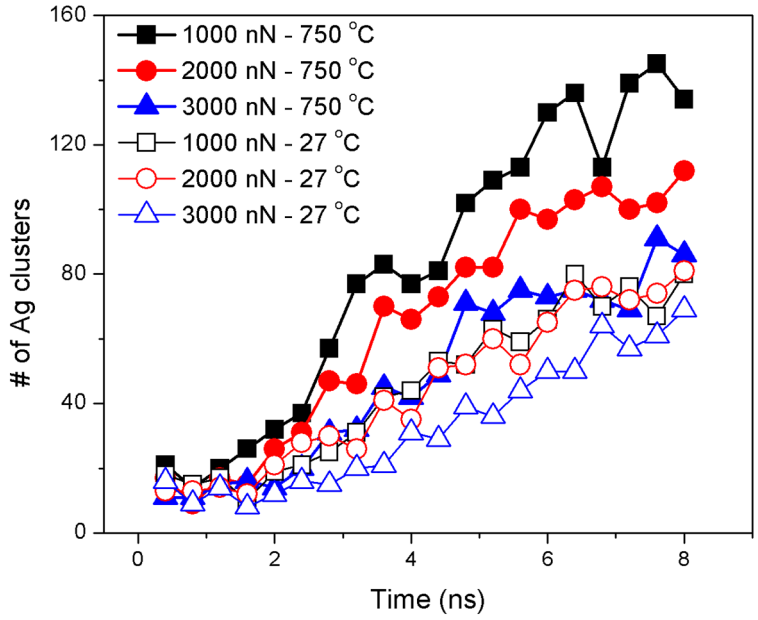

Figure 4.3: Number of high-density Ag cubes as a function of normal load (black squares – 1000 nN, red circles – 2000 nN and blue triangles – 3000 nN) and temperature (solid – 750 °C and hollow – 27 °C).

sity of the model film as a function of load. As shown in figure 4.5, the density of the film increases with increasing load, but the effect of temperature is negligible. When normal load large enough, temperature-induced thermal activation becomes trivial and more atoms are squeezed into each unit volume. Therefore, although silver clusters may dominate the effect of temperature on friction, load affects friction through the combined effects of decreasing sliver and resulting decreased porosity.

4.4 Conclusions

MD simulations predicted an increase of friction with load consistent with experiment. Taken together, the experiments and simulations indicate that the increase in friction with load is due to the combined effects of decreasing presence of silver clusters in the wear track (silver being sheared/extruded from the wear track) and corresponding decreasing porosity, both of which result in the material being less able to accommodate interfacial shear.

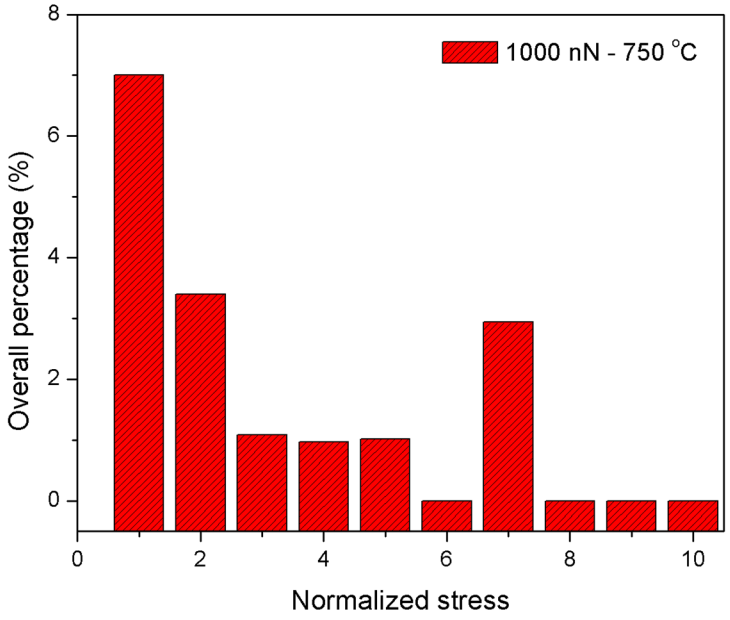

Figure 4.4: Percent of high-density Ag cubes as a function of normalized stress in the case of 8 ns after initial sliding at 750 °C with 1000 nN normal load.

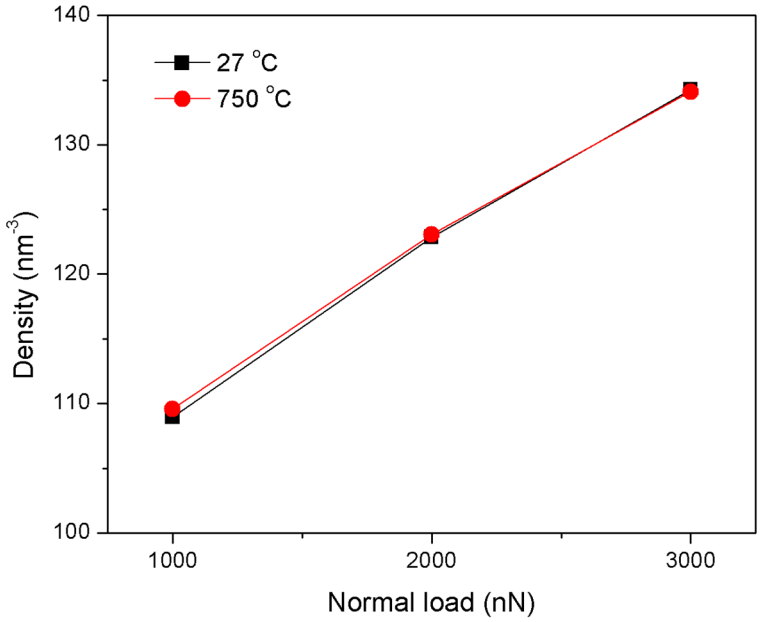

Figure 4.5: Average simulation-predicted density of the film as a function of load at 27 °C (black squares) and 750 °C (red circles).

Chapter 5

Effect of Surface Termination

Friction is an important aspect of materials science for which the atomic nature and the chemical interactions at the material surface play vital roles [115–117]. Research performed so far on $AgTaO_3$ suggests that its functionality depends significantly on phenomena that occur at the material surface during sliding. However, there has not yet been a study focused specifically on surface properties. Here we directly address this issue through a model-based investigation of $AgTaO_3$ surface terminations.

5.1 Introduction

The surface terminations of perovskite materials have been studied before, but rarely in the context of friction or sliding behavior. Perovskite materials with formula ABO_3 are generally formed by stacking AO and BO_2 monatomic layers alternately along the $\langle 001 \rangle$ direction. All $ABO_3(001)$ surfaces have two possible terminations: AO and BO_2. However, previous first-principles calculations of these two terminations showed that their behavior is material dependent [118, 119]. For example, a comparative study of $SrTiO_3$, $BaTiO_3$ and $CaTiO_3$ revealed that $CaTiO_3$ is unique in that it exhibited the most surface reconstruction and, for the TiO_2 termination, was characterized by significant relaxation in the second layer of atoms which in turn affected the band structure [118]. In another study of the same three materials, it was found that the TiO_2-terminated surface was energetically favorable for $BaTiO_3$ and $SrTiO_3$ (the latter was consistent with previous experimental findings), while the CaO-terminated surface was preferred for $CaTiO_3$ [119]. The difference was attributed to cation size, where Ca^{2+} is the smallest cation among the titanates compared. Other first-principles calculation-based studies focused specifically on $SrTiO_3$, reporting surface energies, near-surface atomic displacements, atomic charges and dipole moments of atoms, and the atomic bond populations of various surface terminations [120], and that the TiO_2-terminated surface is more favorable for epitaxial growth of (100) oriented Pt films than the SrO-terminated surface [121]. In the only previous study of the effect of perovskite surface termination on friction, atomic force microscope measurements showed that the friction on SrO-terminated surface of $SrTiO_3$ was larger than that on the TiO_2-terminated surface [122]. This observation was attributed to the higher bonding energy between the TiO_2 coated probe and SrO-terminated surface.

More studies have been reported highlighting the important role of surface termination on tribological behavior for other materials (i.e. not perovskites). For example, MD simulations of di-

amond surfaces showed that hydrogenation increased friction [123, 124]. This observation has been attributed to decreased interfacial bonding [124] and the resulting effect on adhesion [123]. The significant effect of surface termination on adhesion was corroborated by first-principles calculations of the Al_2-, O- and Al-terminated surfaces of Al_2O_3 [125]. Friction can also be affected by surface properties such as hardness and Young's modulus, both of which were shown to be affected by surface termination by density-functional theory calculations of Si [126]. Finally, termination can affect the mobility of atoms on a surface. For example, first-principles calculations showed that Ag diffuses more rapidly on the Al-terminated surface than the O-terminated surface of α-$Al_2O_3(0001)$ due to weaker binding energy on the former surface [127]. This observation is particularly important for our study of $AgTaO_3$ since its low friction is believed to be partially attributable to clustering of Ag which provides a low shear stress sliding interface [11, 48, 128].

This review of the literature has shown that there are previous studies focusing on (1) the different surface terminations of perovskite materials that highlight material-specific behavior of AO and BO_2 terminations, and (2) the important role of surface termination on material and tribological properties of materials in general. Here we report an atomic level investigation of the AgO- and TaO_2-terminated surfaces of $AgTaO_3$, with specific focus on how they affect friction and wear. Using MD simulations, we characterize the surfaces in terms of friction, wear, adhesion and the ease with which atoms are removed from a stable surface. It is shown that Ag clusters are formed at high temperatures as a result of wear in the MD simulations, in agreement with experimental observations [128]. This behavior is explained by the DFT calculations, which predict low barriers to Ag migration and greater binding affinity of Ag on the AgO- versus the TaO_2-terminated surface, ultimately justifying the tendency of silver atoms torn from the surface to form the metallic aggregates observed in the MD simulations and in experiments.

5.2 Methodology – AgO- & TaO_2-Terminated Surfaces

Figure 5.1 illustrates the model AgO- and TaO_2-terminated $AgTaO_3(001)$ surfaces used in the MD runs. During the simulation, the bottommost atomic layers were held fixed. A thermostat was applied to remove the generated heat in order to maintain the systems average temperature around either 0.1 or 1023 K. For brevity, we will refer to the lower temperature as "0 K" in the rest of the article. The 0 K simulation captures the dynamics of the system in response to only the interatomic interactions. This is unphysical but provides us with the limiting behavior of the system at low temperature. The higher temperature was chosen to match the experimental conditions in a previous work [114].

Periodic boundary conditions were applied in the plane parallel to the surface, and simulation time step was 1 fs. The MEAM [3] was used to describe atomic interactions in our models using potential parameters developed earlier (in Chapter 2). We performed four types of simulations to characterize the behavior of the AgO- and TaO_2-terminated surfaces: sliding friction and wear, work of adhesion, surface atom displacement, and surface energy calculation.

Quantifying friction, wear, and adhesion required that we also introduce a probe into the simulations to interact with the surface. The model probe had a radius of 2.97 nm, was constructed of atoms in a Si_3N_4 lattice, and was treated as a rigid body throughout the simulations. In all

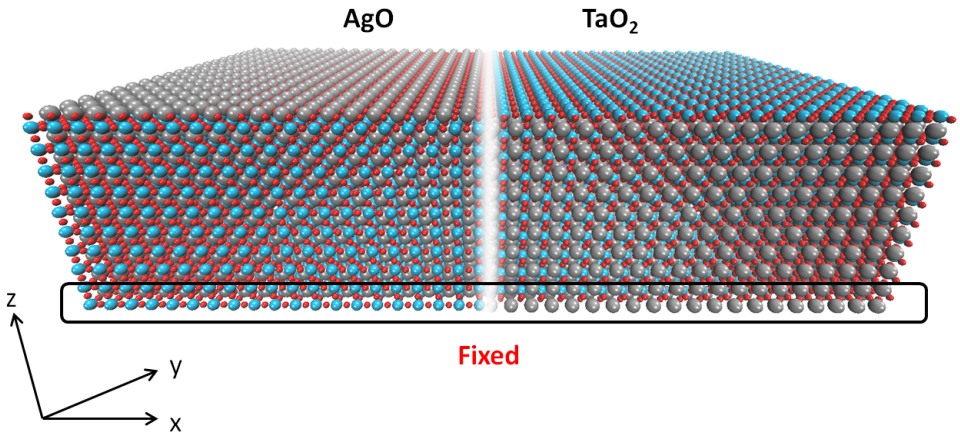

Figure 5.1: The AgO- (left) and TaO_2-terminated (right) surfaces; only half of each model surface is shown. The atoms are represented by blue (Ta), silver (Ag), and red (O) spheres.

cases, the $AgTaO_3$ system was equilibrated for 0.1 ns before bringing the probe into contact with it. The probe-surface interactions were described using an artificially constructed Lennard-Jones type potential. Note that we do not expect this potential to describe the probe-surface interactions accurately. However, since the interaction is the same for both surface terminations, we assume that most of the errors in the description of the surface-probe interaction will cancel out and that the potential will give a faithful qualitative picture of the underlying physics.

To study friction and wear, the model probe was slid over the surfaces. First, a normal load of 881 nN was applied to the probe (the load was chosen such that the pressure was consistent with previous simulation studies of sliding between two flat surfaces [114]), and the system equilibrated again for 0.1 ns. Then, the probe was slid at a constant velocity of 20 m/s in the x-direction for 2 ns. This high speed is necessitated by the time scale limitation in MD simulations, particularly for the relatively large number of atoms in this model. The friction force was measured as the average lateral force on the rigid probe during each cycle, where a cycle is defined by the probe crossing the periodic boundary of the simulation cell. To quantify the evolution of the material in response to sliding, as suggested the results in Chapter 3 and 4, we identified Ag clusters and characterized their size. Clusters were identified as groups of neighboring Ag atoms, where two atoms within 0.25 nm were considered neighbors and a cluster was assumed to consist of at least four atoms. Both the number and size of these clusters may affect friction, so their collective contribution was quantified as the integral of the probability distribution of cluster sizes.

The work of adhesion was calculated to assess the strength of adhesion between the probe and the material surface. The ideal work of adhesion is defined as [70, 129]:

$$W_{adh} = \frac{E_p + E_s - E_{ps}}{A}, \tag{5.1}$$

where A is the contact area, E_{ps} is the total energy of the probe-surface contact at equilibrium, and

E_p and E_s are the total energies of the probe and the surface at equilibrium, respectively. The energies in equation (5.1) were obtained by minimization after the system was equilibrated for 1 ns with zero external normal load applied to the probe. The contact area is defined as the area (projected in the xy-plane) of the atoms in the probe apex that were within 0.5 nm of the material surface.

In addition to probe-surface interactions, we studied the force required to displace atoms away from the two surfaces. Different groups of atomic clusters were identified on each surface, namely, AgO_x (x = 0,1,...,4) on the AgO-terminated surface and TaO_y (y = 0,1,...,5) on the TaO_2-terminated surface. After the material was equilibrated for 0.1 ns, each atomic cluster was displaced straight upward (in the z-direction), away from the surface. To match the sliding velocity in our friction and wear simulations, the atoms were displaced with a constant velocity of 20 m/s. The vertical force on each atom group was measured as they were pulled away, where the peak value was identified as the threshold for detaching the atoms from the surface.

5.3 Results and Discussion

5.3.1 Tribological Behavior

The average friction force per cycle predicted by MD simulations of a probe sliding on the $AgTaO_3$ surfaces is shown in figure 5.2. The results demonstrate that friction initially decreases and then reaches a relatively stable value on both the AgO- and TaO_2-terminated surfaces. At 0 K, the friction on the TaO_2-terminated surface is larger than that on the AgO-terminated surface throughout the simulation. However, the differences in friction between both surfaces are negligible at higher temperatures and, at 1023 K, the average force on both surfaces is essentially equal. The observation that friction decreases with temperature is consistent with the experimental measurements, which showed that friction decreases, on average, by 36.5 % as the temperature increases from room temperature to 1023 K. Details of the complementary experimental results for this research are provided in Appendix A.3.

From our MD simulations, visual analyses of the model surfaces after sliding, shown in figure 5.3, reveal a buildup of silver on the edges of the wear track similar to that observed experimentally. The buildup is more pronounced on the AgO-terminated surface and at the higher temperature. Since AgO termination and higher temperature are also associated with lower friction, these results suggest that the redistribution of silver plays an important role in the friction characteristics of this material.

To investigate this further, we analyzed the wear tracks generated in the sliding simulations. Figure 5.4(a) shows representative cross-sectional profiles of the wear tracks (z-coordinates of the topmost atoms are averaged along the x-direction) in terms of element type at the end of the fifth cycle. Figure 5.4(b) shows the evolution of the wear-track depth for the AgO- and TaO_2-terminated surfaces at 0 and 1023 K. We observe that the wear depth increases with cycle and is larger at the higher temperature for either surface. Also, at 1023 K, the wear track is deeper on the AgO surface than the TaO_2 surface.

To quantify the material evolution due to wear, we characterized the composition of the sur-

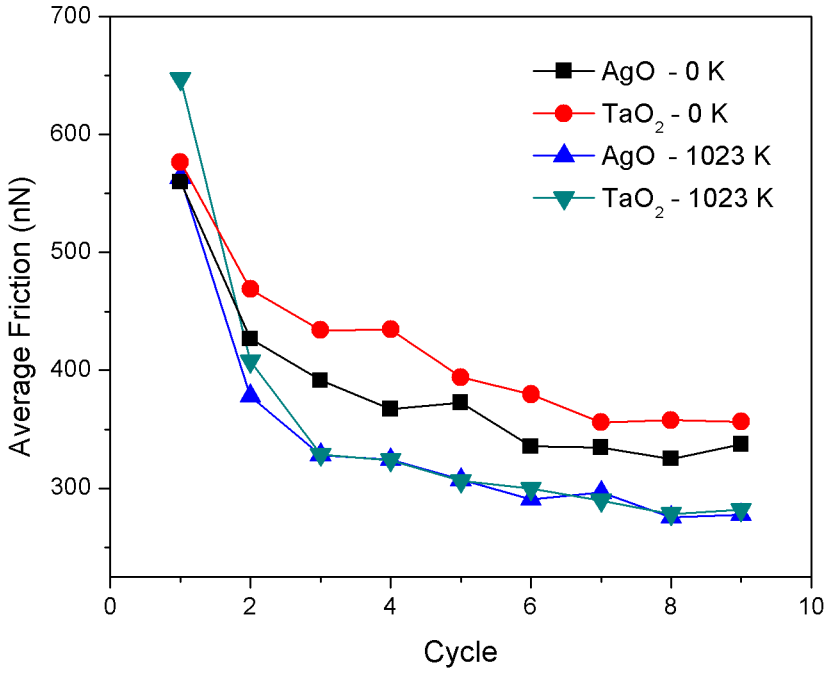

Figure 5.2: Friction force on the AgO- (circles) and TaO_2-terminated (triangles) surfaces at 0 K (filled symbols) and 1023 K (hollow symbols) as a function of cycle number.

faces before and after sliding, focusing on Ag segregation and clustering based on the experimental clues [48, 128].

Figure 5.5 quantifies the Ag clustering on the AgO- and TaO_2-terminated surfaces after the first and last sliding cycles at the two temperatures. Silver clustering is negligible before sliding in any case. The number of Ag clusters increases with sliding cycles and is always larger at 1023 K. The inset of figure 5.5 facilitates comparison of clustering on the two surfaces. First, we observe that, at any temperature, there are more Ag clusters on the AgO surface at any cycle. However, at 1023 K, the magnitude of this difference decreases rapidly with number of cycles. At the first sliding cycle, there are more clusters on the AgO surface, corresponding to the lower friction at that cycle in figure 5.2. This is explained by the lower migration barrier of Ag on the AgO surface, as shown later. However, after several sliding cycles, the number of Ag clusters is effectively the same on either surface, corresponding to the similar friction exhibited in figure 5.2.

5.3.2 Adhesive Strength

The adhesive strength on a surface often plays a major role in determining its friction and wear behavior. The work of adhesion calculated from MD simulations of probe-surface interactions is 0.56 J/m^2 for the AgO surface and 3.21 J/m^2 for the TaO_2 surface. The smaller adhesive strength

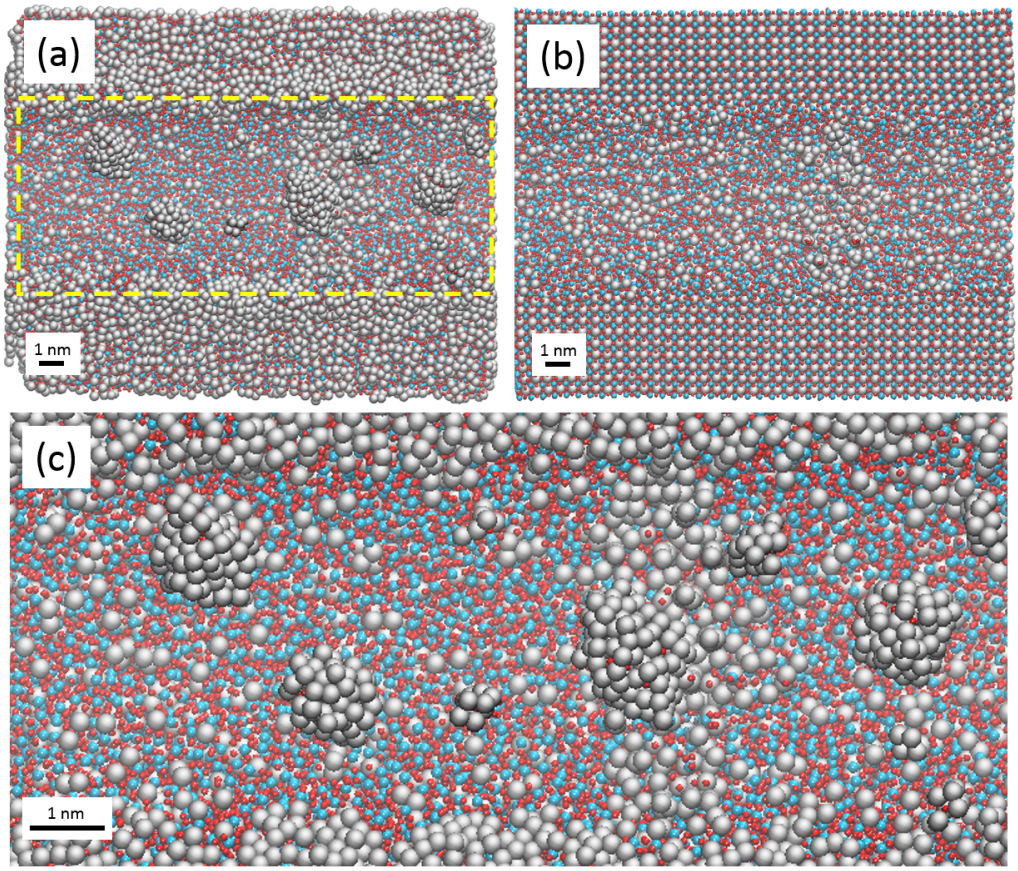

Figure 5.3: Top view of surfaces after 5 cycles of sliding: (a) AgO surface at 1023 K and (b) TaO_2 at 0 K. A close up of the wear track (identified by the dashed line in (a)) is shown in (c). Atom colors ar the same as those in figure 5.1.

of the AgO surface is consistent with the lower friction observed at either temperature in the first cycle and at 0 K during all cycles in figure 5.2.

The adhesion results can be interpreted in terms of the relative reactivities of the two surfaces, based on the relaxation energies calculated from density-functional theory. The relaxation energies are 0.86 and 2.88 eV for the AgO and TaO_2 surfaces, respectively. Thus, the AgO surface is relatively stable as cleaved, whereas the TaO_2 surface undergoes a comparatively strong reconstruction. Chemically, this means that complete octahedra, present in the AgO surface, are more stable than cleaved octahedra, as on the TaO_2 surface. The cleaved octahedra deform to compensate for the missing oxygen giving a larger surface relaxation energy. We speculate that the higher adhesive energy for the probe on the TaO_2 surface is caused by the greater reactivity of the cleaved octahedra.

The reduced reactivity of AgO and the stability of complete octahedra can also be demonstrated by the ease with which atoms can be removed from the surface. To quantify this, we considered different groups of atoms on the top layer and measured the maximum force required to sepa-

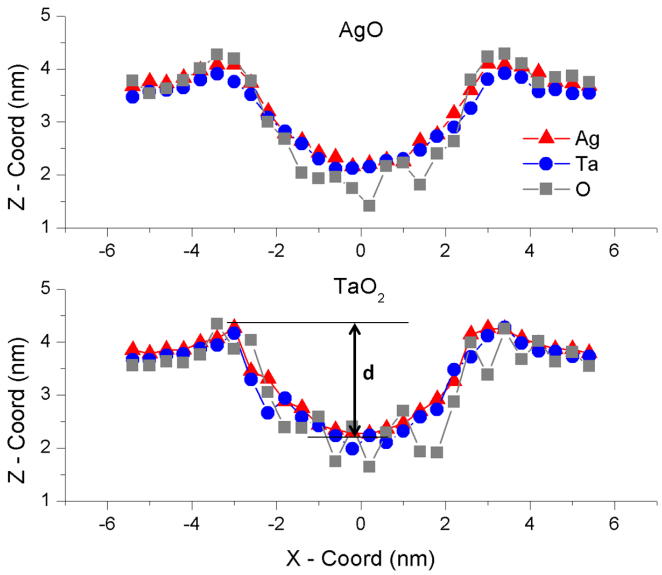

(a)

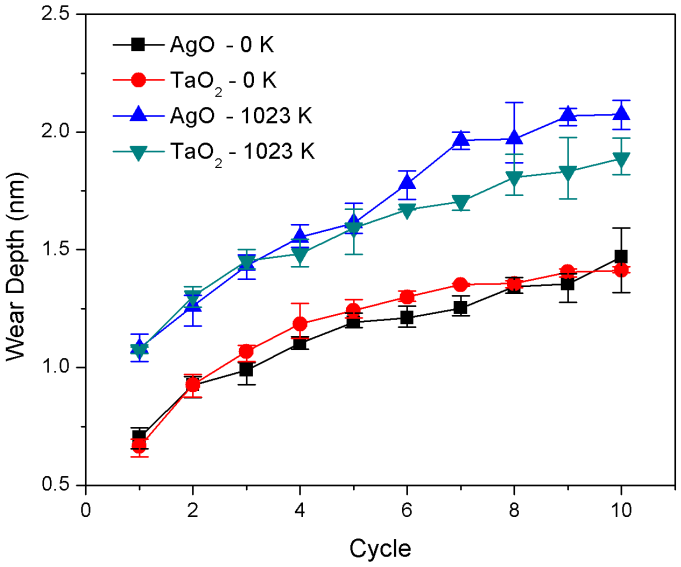

(b)

Figure 5.4: (a) Representative cross-sectional profiles of the wear track on the AgO- and TaO_2-terminated surfaces after the fifth cycle of sliding. (b) Increase of wear depth with cycle on the AgO (circles) and TaO_2 (triangles) surfaces at 0 K (filled symbols) and 1023 K (hollow symbols). Error bars reflect the variation of depth along the length of the wear track.

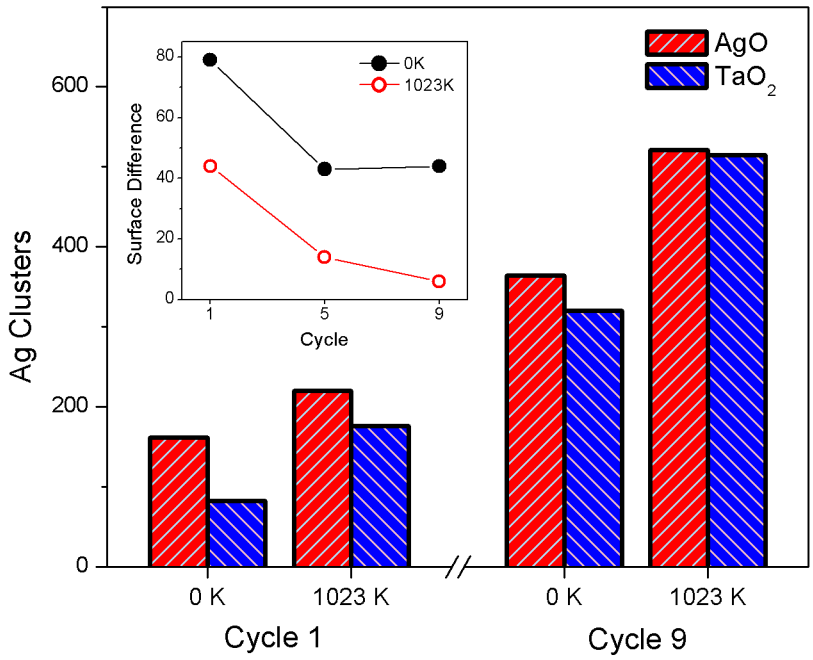

Figure 5.5: Variation of silver clusters with cycle and temperature for the two surfaces. The inset shows that the difference between the silver clustering on the AgO surface and that on the TaO_2 surface decreases with cycle and is smaller at the higher temperature.

rate them from the surface in our MD simulations. Figure 5.6 shows the force required to remove atoms from the AgO- and TaO_2-terminated surfaces. Figure 5.6(a) shows that a very small force is required to remove a single Ag from its lattice position on the AgO-terminated surface. This force increases rapidly as more oxygen atoms are removed along with the Ag. Consequently, external forces are more likely to result in the removal of individual Ag atoms from an AgO-terminated surface rather than cleaving the relatively stable TaO_6 octahedra. In contrast, on the TaO_2-terminated surface, as shown in figure 5.6(b), approximately equal forces are required to pull away either a single Ta or a Ta with multiple coordinated oxygens. This is also consistent with the observation from the simulations that individual silver atoms segregate easily on the AgO-terminated surface. The relative ease with which a silver atom is removed from the surface permits the formation of Ag clusters, as observed in both the MD simulation and the experimental wear track. We focus on the energetics of Ag migration in the next section.

5.3.3 Ag Migration

The ability of silver atoms to migrate on a surface is related to the potential energy barrier for a single Ag atom moving over the surface. Contour plots of the energy landscape obtained from the MEAM potential used in the MD simulations are shown in figure 5.7. The plots show that the

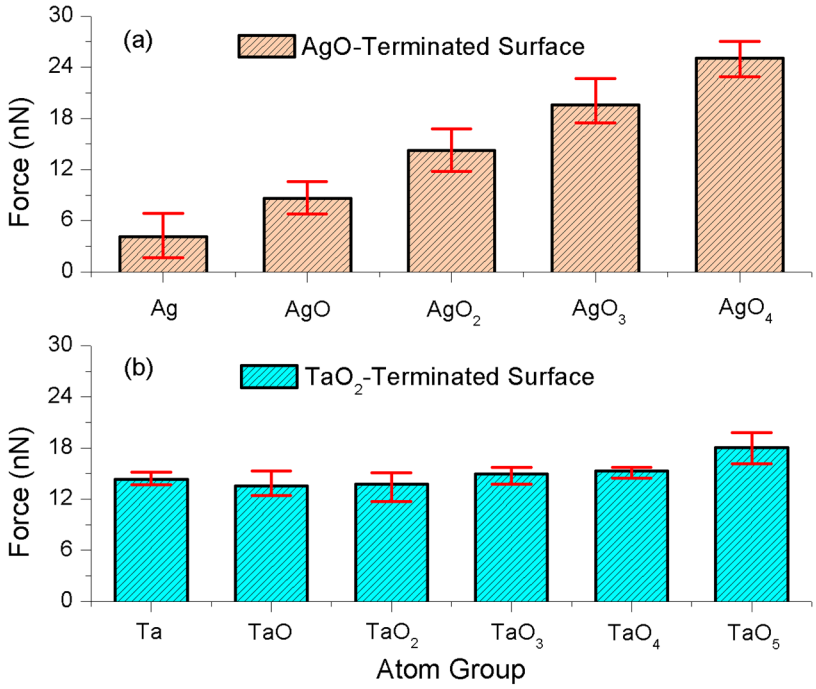

Figure 5.6: Force required to displace atoms from the (a) AgO- and (b) TaO_2-terminated surfaces. Error bars represent the variation in force when displacing the same atoms from five different positions on the surface.

single Ag atom prefers to bind on top of the O atoms on the AgO surface and over the Ta atoms on the TaO_2 surface. The minimum energy path on the AgO surface involves a migration from the basin at (1,1/2) to (1/2,0). Along this path, the energy barrier is 0.024 eV. On the TaO_2 surface, the lowest energy path is from (1/4,1/4) to (1/4,3/4) and the energy barrier is 0.052 eV. We too obtained potential energy surfaces for Ag migration as well as binding energy from DFT calculations. Those results are discussed in Appendix A.4.

5.4 Conclusions

The $AgTaO_3$(001) surface presents two common terminations: AgO and TaO_2. In this chapter, we analyzed these surfaces by performing sliding simulations of friction and wear and by calculating the work of adhesion, the forces required to displace atoms from the surface, and the energetic barriers to silver migration.

Our results show that at low temperature, friction is influenced by the chemical nature of the surface. TaO_2-terminated surfaces present a higher work of adhesion as well as larger relaxation energies than AgO-terminated surfaces, which are caused by the existence of (relatively unstable and reactive) cleaved TaO_6 octahedra on the former. This causes sliding on the TaO_2 to be harder

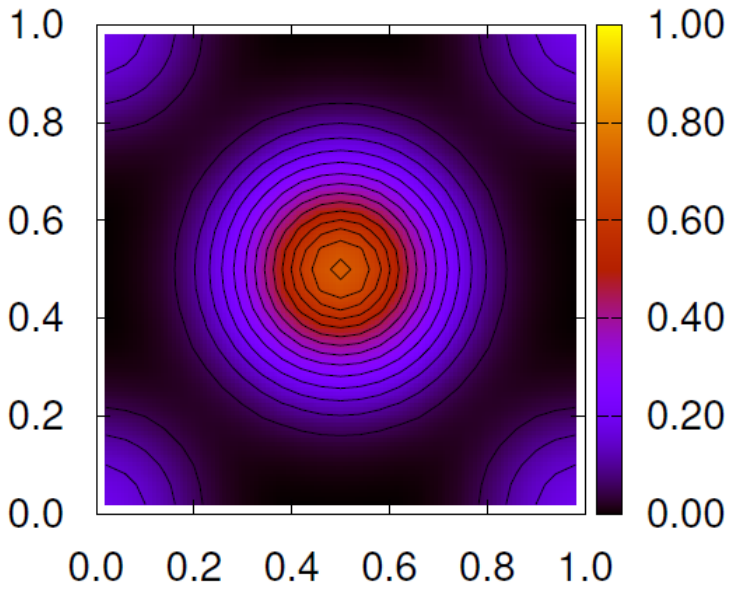

(a)

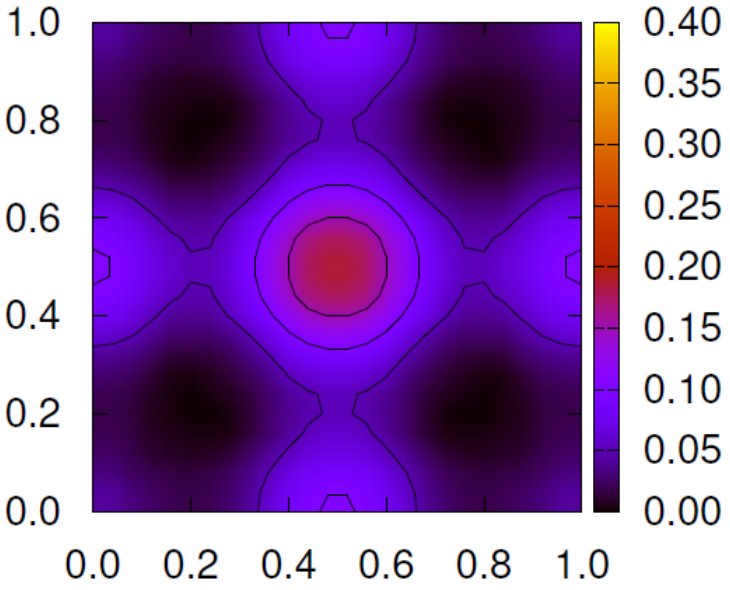

(b)

Figure 5.7: Potential energy surfaces calculated using the MD potential for the migration of a Ag atom over the (a) AgO- and (b) TaO_2-terminated surfaces. The energy units are eV, and the x and y coordinates are fractions of a cell length.

at low temperature and results in a higher friction force. At high temperature, the dominant friction mechanism is the formation of silver aggregates, which were observed both in our sliding simulations and at the edges of the experimental wear tracks, and both surfaces present equivalent friction characteristics.

We also probed the chemical nature of the surface by pulling different atomic clusters from the surface. We showed that pulling a single atom from the AgO surface is relatively easy, whereas removing oxygens requires more force, which is indicative of the aforementioned stability of the TaO_6 moiety. In consequence, it is reasonable to assume that the silver atoms are relatively free to move on the surface provided there is enough energy (thermal or mechanical) to enable them to overcome the energy barriers associated with such motions.

The last piece of the study in this chapter is the calculation of energy barriers to migration of silver on both surface terminations, predicted by DFT to be in the range of 0.1-0.2 eV, with a higher barrier for the TaO_2 surface. This is equivalent to a thermal energy that is in the range of 1000-2000 K, consistent with the experimental findings and the MD simulations presented. MD potential energy surfaces for silver migration agree with DFT results, although the barriers are smaller. The DFT binding energies for Ag are 4.14 eV on the AgO-terminated surface and 2.75 eV on the TaO_2 termination, showing the greater affinity of silver for the former than the latter.

In summary, our results provide a thorough understanding of the mechanisms that enable the excellent friction characteristics of $AgTaO_3$ in different temperature regimes. In addition, these calculations provide direct atomic-scale evidence supporting the Ag-facilitated sliding mechanism previously suggested to explain experimental observations.

Chapter 6

Film Reconstruction Due to Sliding and Role of Ag Content

6.1 Introduction

Previous experimental study showed that $AgTaO_3$ exhibited CoF as low as 0.06 at 750 °C [48]. The transmission electron microscopy observations indicated that the lubricious nature of $AgTaO_3$ at high temperatures was enabled by the joint contributions of the hard Ta_2O_5 phase and lubricious silver clusters in the shear- and temperature-induced surface layer. Theoretical and experimental cross-sectional images of the coatings in the wear track revealed that the presence of Ta_2O_5 and silver increased dramatically closer to the interface whereas the remainder of the coating consisted primarily of $AgTaO_3$ with a very small amount of finely dispersed silver. Reconstruction of $AgTaO_3$ from the silver and Ta_2O_5 phases from mechanical mixing during wear testing has also been hypothesized [48]. With increased normal force during testing, the diffusion and plowing of the silver from the surface increased, causing the coating to decrease in density and increase in porosity. MD modeling complemented the experimental results and supported the hypothesis that friction increased with load due to changes in the silver distribution and near-surface density [114]. In the present study, we further investigate the suggestion that low friction in $AgTaO_3$ is enabled by the reconstruction of the material into silver and Ta_2O_5 by studying the tribological properties of Ag/Ta_2O_5 nanocomposite coatings using MD.

6.2 Methodology – Ta_2O_5/Ag Films

We modeled a rigid hemispherical probe slid over a tribofilm consisting of Ta_2O_5, Ta_2O_5/M at.% Ag (M=6.3, 14.3, 20.0 and 26.0) or $AgTaO_3$. The Ta_2O_5/Ag films were created by embedding 8 nm^3 regions of silver atoms into the Ta_2O_5 film, where the percent silver was adjusted by increasing the number of these silver regions. All films had dimensions of 16.30 (in sliding direction) × 11.44 × 3.88 nm^3. To mimic the near-surface reconstruction observed in the experiment [130], a mechanically-mixed tribofilm was created by first sliding a rigid plate (same cross-sectional area as the film) over the material surface. Then a probe was introduced into the model and slid on the resultant tribofilm. During the simulation, the bottom layer of the tribofilm was held fixed, and the probe with 2.72 nm radius moved laterally at a constant speed of 100 m/s for 1 ns with a timestep of

1 fs. The high sliding speed is necessitated by the timescale limitation in MD simulations, particularly for the relatively large number of atoms in this model. A normal load of 300 nN was uniformly distributed on the probe. The temperature of the system was maintained at 750 °C throughout the simulation using a Langevin thermostat. Periodic boundary conditions were applied in the sliding plane (otherwise, atoms were confined by the rigid boundaries). The friction force was measured as the average lateral force on the rigid probe during each cycle, where a cycle is defined by the probe crossing the periodic boundary of the simulation cell. Wear depth was defined as a vertical distance between the equilibrated film surface and the bottom of the wear track. To quantify the evolution of the films in response to sliding, as suggested by the previous results in Chapter 3, 4, and 5, we identified silver clusters and characterized their size. The MEAM was used to describe the atomic interactions.

6.3 Results and Discussion – Friction, Wear & Film Evolution

Figure 6.1 shows the friction force for each model film. In general, the friction initially increased (consistent with a run-in process) and then approached a steady state around the fifth cycle. In the steady state, the Ta_2O_5 exhibited the highest friction, and then friction decreased with increasing silver content. This is consistent with trends reported in previous experimental work where adding/increasing silver decreased friction in Mo_2N/MoS_2/Ag [35] and YSZ-Ag-Mo nanocomposites [103], as well as other coating materials (such as TiN, CrN, ZrN, DLC and TaN) [131–135]. This correlation between friction and silver content can be attributed to the fact that silver facilitates sliding over a range of temperatures due to its low shear strength [136]. We also observed that $AgTaO_3$ exhibited the lowest friction, slightly lower even that the Ta_2O_5/Ag film with similar silver content (i.e. 20 %), which is consistent with our experimental results [130].

The various model films were also characterized in terms of their wear resistance, as shown in figure 6.2. We observe that the wear rate (slope of the depth vs cycle plot) reached approximately a constant value in steady state. Also, for each cycle, the wear depth increased with increasing silver content, with Ta_2O_5 exhibiting the best wear performance. We also observed less wear on the $AgTaO_3$ film than the Ta_2O_5/Ag films. This is inconsistent with the experimental result that Ta_2O_5/Ag exhibited less wear than $AgTaO_3$. However, it has been reported that the effect of incorporating of silver into a coating is non-monotonic. Specifically, the wear performance of a coating material improves with a small amount of silver, but may deteriorate as more silver is added [131–134]. The experimental results are consistent with the former trend while the simulation results reflect the latter. The discrepancy is likely related to relative sizes of the model and experiment. Specifically, in the 14 at.% silver model film, all the silver atoms are localized at the sliding interface, whereas, in the experiment, the silver is likely not distributed evenly within the film and the actual amount of silver in the material at the sliding interface may be less than 14 at.%. The simulation results in figure 6.3 suggest that the actual percent silver in the interface during experiment is likely less than 6 at.%.

To understand the friction and wear trends, we analyzed the evolution of the silver content during sliding. Since both the number and size of silver clusters may affect friction, the overall contribution was quantified as the integral of the probability distribution of cluster sizes. In this study, we focused on the wear track and the silver clusters in that region. Figure 6.3 shows that silver

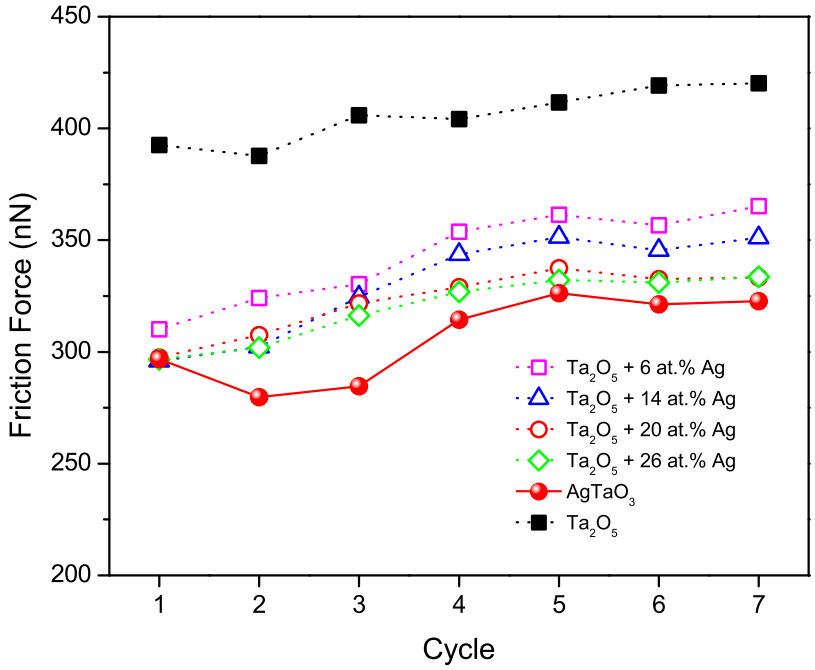

Figure 6.1: Model-predicted friction forces for tribofilms with different compositions.

clustering in all Ta_2O_5/Ag films increased with silver content. This trend can be directly correlated to the decreasing friction with silver shown in figure 6.1. However, the fact that the friction for the Ta_2O_5/20 at.% Ag and Ta_2O_5/26 at.% Ag was similar indicates that there is a limit to the friction reducing effect of silver. That is, once the silver content reaches some critical value (20 % per the results in this simulation) the friction will no longer increase with increasing silver content. As suggested by previous experimental results on WS_2-Ag [137], this behavior might be attributed to the depth of penetration of the probe, which gradually increases with silver content due to the softness of silver, leading to increased plowing stress in front of the counterface. This affects the wear behavior and is consistent with the wear results shown in figure 6.2. The trends exhibited by the silver clustering in the $AgTaO_3$ suggests that the silver that is initially evenly distributed in the film gradually forms silver clusters that continue to provide low shear resistance as sliding progresses. The behavior of silver clusters in $AgTaO_3$ is further supported by a calculation of the average vertical displacement (towards the surface) of silver during sliding, which we found to be 0.09 nm and 0.24 nm for the $AgTaO_3$ and Ta_2O_5/20 at.% Ag films, respectively. This, along with the silver cluster results, indicates that silver clusters form and migrate to the surface more gradually on the $AgTaO_3$ films than the Ta_2O_5/Ag films, leading to both lower friction and wear.

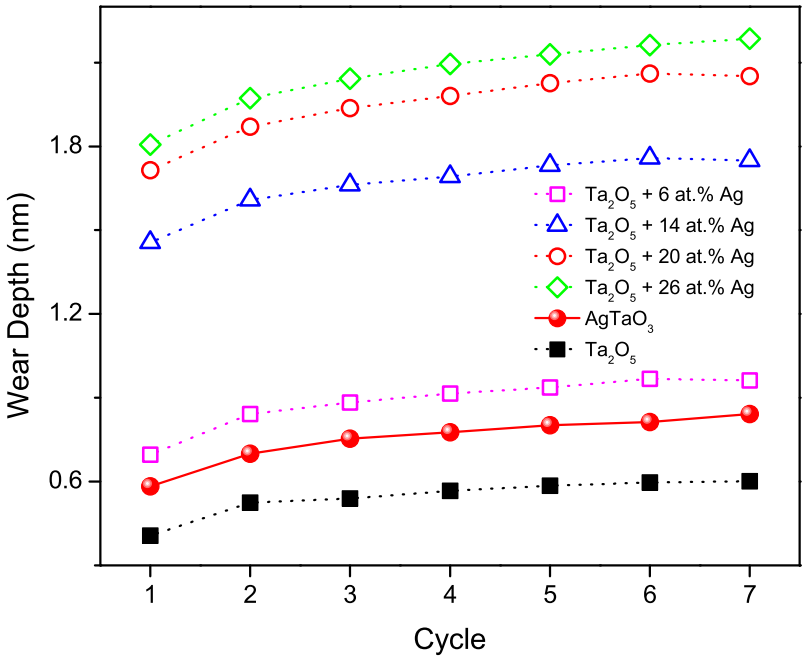

Figure 6.2: Model-predicted wear depths for tribofilms with different compositions.

6.4 Conclusions

In summary, molecular dynamics simulations were performed to study the tribological properties for the films with different compositions. The results showed that the surface of the coating was changed over time as a result of the migration of silver to the surface. These changes affected friction and wear of the sliding interface. Those results also revealed that friction decreased while wear increased with increasing silver content in Ta_2O_5/Ag films. However, the lowest friction was always observed on $AgTaO_3$. The lower CoF values for $AgTaO_3$ are probably due to the even distribution of the silver in this system and the gradual formation and migration of silver clusters to the interface. The wear performance was less straightforward since the experimentally-measured wear was smaller on the Ta_2O_5/Ag films than the $AgTaO_3$, while simulations predicted the opposite trend. This difference was attributed to localization of silver in the interface in a simulation that is unlikely to occur in the experiment. Overall, the results suggest that it is possible to tune the friction and wear performance of Ag-Ta-O films by tuning the amount of embedded silver for a given set of operating conditions.

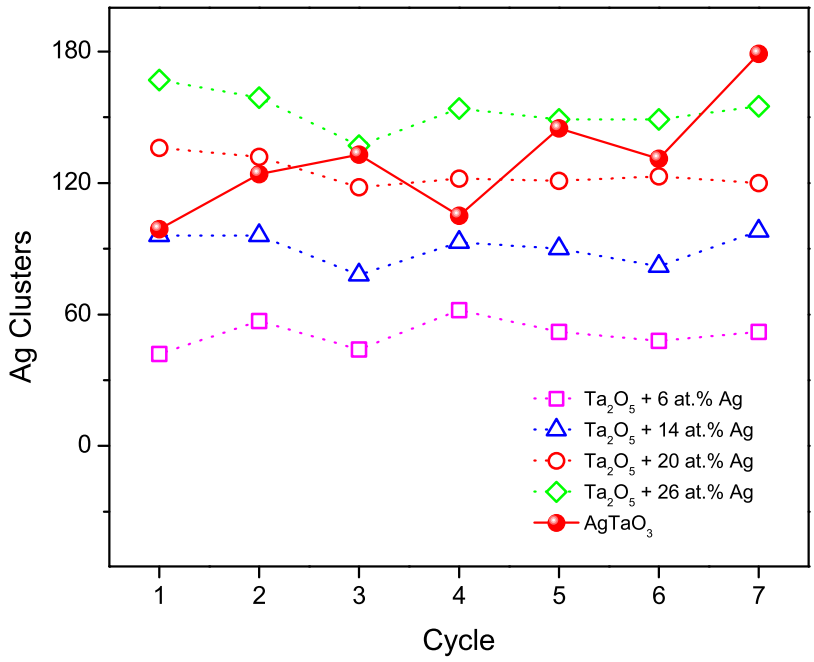

Figure 6.3: Model-predicted silver clusters for tribofilms with different compositions.

Chapter 7

Cu-Ta-O Ternary Oxides

7.1 Introduction

High-temperature induced oxidation and the resulting irreversible chemical changes result in a failure of conventional solid lubricants to provide the desired lubricity [5, 15, 138]. Considering the shortage of available candidates for high-temperature applications, developing effective solid lubricants that remain thermally stable and lubricious over a wide range of temperatures is imperative.

Oxide-based materials are promising lubricants for high-temperature applications due to their structural and chemical inertness [139]. Ternary metal oxides, including Zn(Pb)-W(Mo,Ti)-O, Ca(Ba,Sr)-S-O, and Ag-Ta(V,Mo)-O, have been explored recently due to their low friction at high temperature [35, 48, 139–143]. Previous experimental work focused on silver tantalate ($AgTaO_3$), which possesses a layer-like structure, can form a soft, metallic (silver) phase when subjected to sliding, and is highly resistant to oxidation [36, 48]. The CoF for $AgTaO_3$ was reported to decrease with temperature down to 0.06 at 750 °C [48, 128].

Given the relatively poor wear performance of $AgTaO_3$ and the issues associated with Ag particle migration, we have been exploring alternatives to obtain both low friction and high wear resistance. A potential candidate is a Cu-Ta-O ternary oxide because: (1) both Cu and Ag are soft metals that have been used as dopants to improve tribological performance of various coating materials [34, 144–147]; (2) Cu-based oxides have been used as high-temperature solid lubricants [141]; and (3) Cu and Ag belong to the same group of elements, so similar material properties are expected (e.g., the substitution of Cu in $Ag(Nb_xTa_{1-x})O_3$ has been performed to study the composition dependence of dielectric properties [148]). From a practical perspective, the fairly reasonable market price of Cu could render it more competitive for potential industrial applications [49].

In this chapter, we focus on two Cu-Ta-O ternaries, $CuTaO_3$ and $CuTa_2O_6$, and contrast their performance with $AgTaO_3$. The structures of $AgTaO_3$, $CuTaO_3$, and $CuTa_2O_6$ are shown in figure 7.1. $CuTaO_3$ was considered because it shares the same perovskite structure with $AgTaO_3$. The comparison between $CuTaO_3$ and $AgTaO_3$ will allow us to isolate the effect of the metal on the tribological performance. However, from an experimental perspective, $CuTaO_3$ is not practical because it cannot be synthesized at atmospheric pressure [149]. Therefore, $CuTaO_3$ is studied using only simulations in this work. The experiments focus on $CuTa_2O_6$, which can be prepared relatively easy. This material also has a perovskite-like structure, but with alternating vacancies in the Cu sites.

Additionally, a recent study showed that the frictional properties of $Ag_2Ta_4O_{11}$ differed from those of $AgTaO_3$ [48], which suggests that $CuTa_2O_6$ and $CuTaO_3$ may also have significantly different tribological properties and that tuning of coating performance may be achieved by controlling the noble-metal content of the coating during deposition.

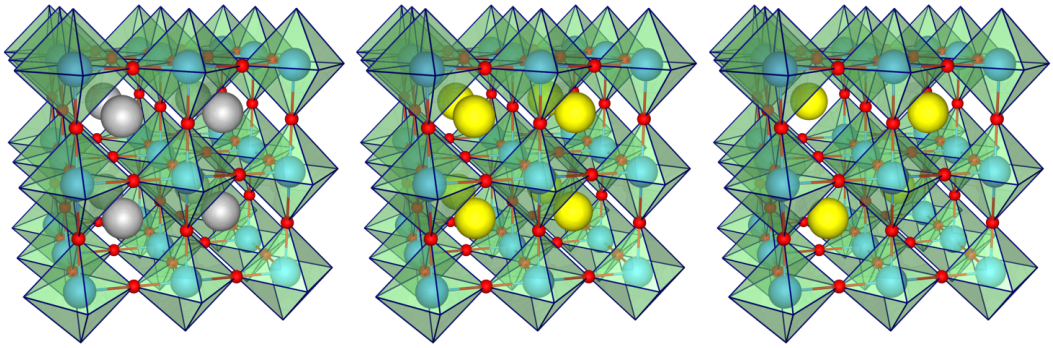

Figure 7.1: Structures of the $AgTaO_3$ (left), $CuTaO_3$ (middle), and $CuTa_2O_6$ (right) perovskite-like crystals. Sphere colors represent: Ta – Blue, O – Red, Cu – Yellow, Ag – Grey.

In this work, the tribological performance of (Ag,Cu)-Ta-O materials was explored and compared. MD simulations were performed using newly-developed empirical potential parameters fit to DFT results for each Cu-Ta-O ternary oxide (DFT results were provided by our colleagues *A. Otero-de-la-Roza and E.R. Johnson*). The friction and wear properties were compared with those of $AgTaO_3$. Results were analyzed in terms of the underlying sliding mechanisms with a focus on the formation of Ag/Cu clusters at the interface that can facilitate sliding.

7.2 Methodology

7.2.1 Potential Parameter Fitting

Potential parameters for the ternary Cu-Ta-O oxide were developed based on the modified embedded-atom method formalism [3], which has been successfully used to reproduce material properties of $AgTaO_3$ (see Chapter 2). MEAM parameters for pure Cu, Ta, and O were taken from reference [3] and are given in table A.4 of the Appendix A.5. For the binary oxides, parameters were fitted based on a B1 structure, consistent with our previous fitting of the Ag-O and Ta-O binaries in Chapter 2. The relative density (ρ_0), exponential decay factor (α_{edf}), and screening parameters (C_{min} and C_{max}) for Cu-O were determined based on the structural and elastic properties predicted by DFT calculations. Next, the binary parameters were used in the fitting process for the ternary oxide, where additional potential parameters (i.e. parameters for the immiscible binary Cu-Ta and ternary Cu-Ta-O) were adjusted by making the empirical potential reproduce the DFT-predicted lattice constants, angles, elastic constants, and cohesive energy of the Cu-Ta-O compounds. Due to the differences in the chemical and mechanical properties of $CuTaO_3$ and $CuTa_2O_6$, two separate sets of potential parameters were fitted to better describe these two materials. Detailed information

about the fitting process can be found in Chapter 2.

Table 7.1 shows the MD- and DFT-predicted structural and elastic properties of $CuTaO_3$ and $CuTa_2O_6$. The mean absolute percent differences between MD and DFT results (assigning equivalent weighting factors to each property) were 1.32 % and 4.11 % for $CuTaO_3$ and $CuTa_2O_6$, respectively. The final potential parameters for the two materials are given in table A.5 of the Appendix A.5.

Table 7.1: MD- and DFT-predicted structural properties of $CuTaO_3$ and $CuTa_2O_6$.

Property		$CuTaO_3$		$CuTa_2O_6$	
		MEAM	DFT	MEAM	DFT
Cell Lengths (Å)	$a/b/c$	3.90	3.90	7.61	7.45
Cell Angles (°)	$\alpha/\beta/\gamma$	90.00	90.00	90.00	90.00
Cohesive Energy (eV)	E_c	6.20	6.20	6.97	6.73
Elastic Constants (GPa)	C_{11}	450.83	503.49	426.32	431.43
	C_{12}	104.48	104.47	75.04	79.20

To verify the validity of those parameters, we compared the energy-volume curve obtained using MD with our DFT calculations (see figure 7.2). The results show that, within 20 % of the equilibrium volume, the relative energies of both $CuTaO_3$ and $CuTa_2O_6$ are well-captured by the potentials. In addition, the MD-predicted thermal expansion coefficient for $CuTa_2O_6$ at temperatures between 200 and 1200 K is 3.73×10^{-6} K^{-1}, which is comparable to the experimental measurement of 8.0×10^{-6} K^{-1} [150].

7.2.2 Sliding Models

Using the newly fitted MEAM parameters reported in the previous section, two sliding models were created to study the friction and wear behavior of Cu-Ta-O: (1) plate-on-plate and (2) ball-on-plate. These models are shown in figure 7.3. Model 1 facilitates calculation of the average friction force and analysis of the film reconstruction during sliding, while model 2 allows characterization of material transfer and wear. Simulations with these two models were performed for each of the three materials: $AgTaO_3$, $CuTaO_3$ and $CuTa_2O_6$.

The dimensions of the tribofilms (i.e. the bottom plate) for all three materials were $9.7 \times 2.2 \times 11.9$ and $16.4 \times 11.9 \times 3.7$ nm^3 for Models 1 and 2, respectively. In Model 2, the ball was assigned a radius of 2.5 nm. In each model, the top plate/ball was kept rigid during sliding, and the positions of the atoms in the bottommost layer of the film were fixed. The plate/ball slid laterally at a constant speed of 10 m/s with a timestep of 0.5 fs. Periodic boundary conditions were applied in the sliding plane; in the direction perpendicular to that plane, atoms were confined by the rigid boundaries. Normal loads of 1000 and 300 nN were uniformly distributed on the rigid plate (in Model 1) and ball (in Model 2), respectively. Tribological simulations with the two models were performed at room temperature (RT, 27 °C) and 750 °C. The temperature was maintained using a

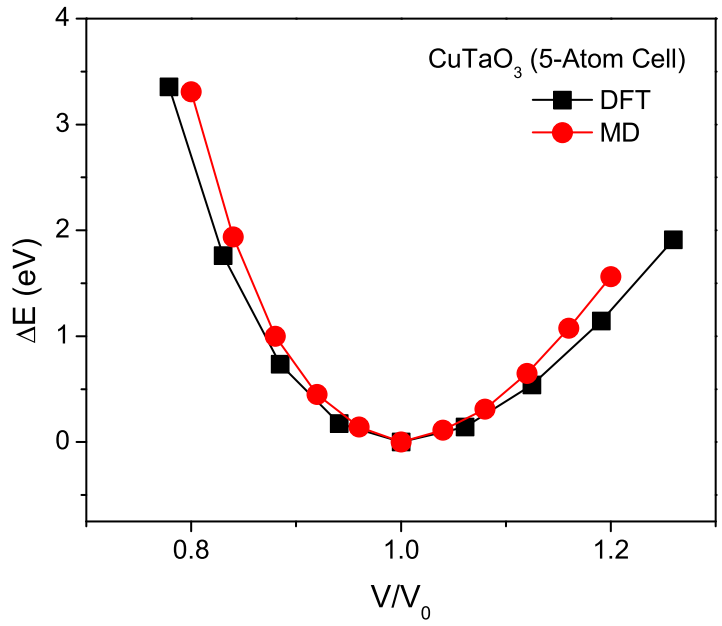

(a)

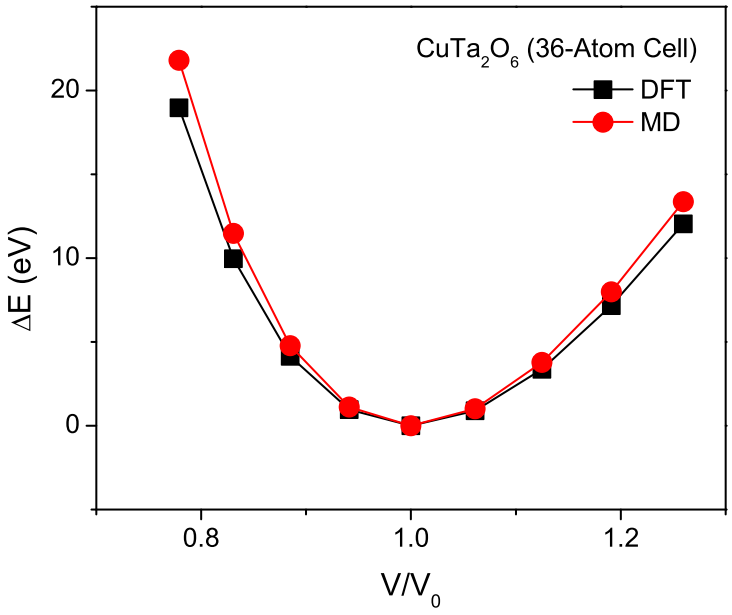

(b)

Figure 7.2: Volume-dependence of the energy for (a) $CuTaO_3$ and (b) $CuTa_2O_6$ from MD and DFT. ΔE is the energy relative to the equilibrium structure, with volume V_0.

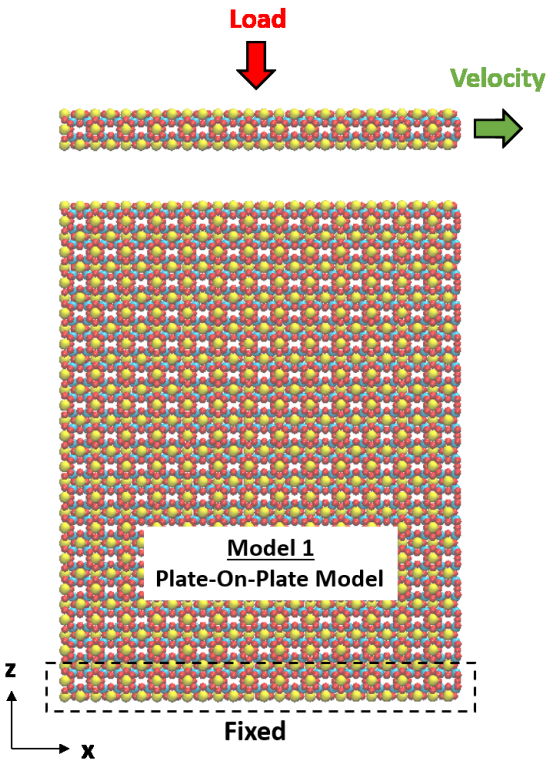

(a)

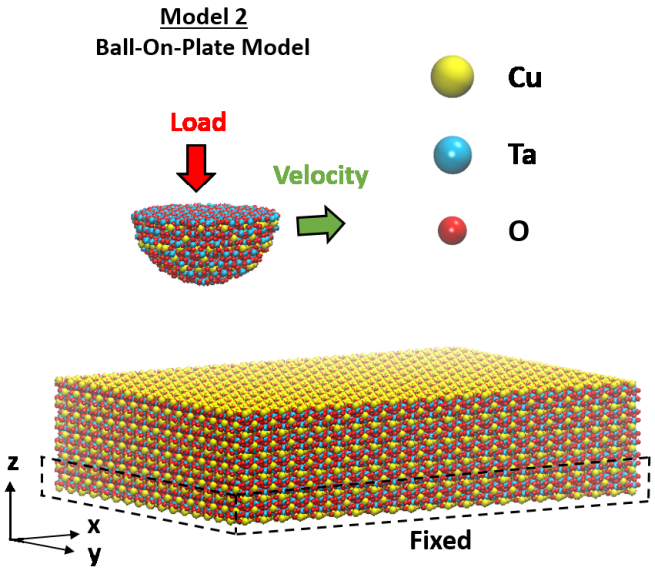

(b)

Figure 7.3: Initial configurations of the two MD simulation models, shown here for $CuTa_2O_6$.

Langevin thermostat in the canonical ensemble. The friction force was defined as the average lateral force on the plate from Model 1. The wear depth, in Model 2, was defined as the vertical distance between the equilibrated film surface and the bottom of the wear track. To quantify the evolution of the films in response to sliding, we identified Ag/Cu clusters and characterized their sizes. A cluster was identified as a group of Ag/Cu atoms consisting of at least four atoms with each neighboring distance less than 0.25/0.20 nm, where a smaller neighbor distance criterion was used for Cu to reflect its smaller atomic radius.

7.3 Results

7.3.1 Friction

Figure 7.4(a) shows the average friction force from MD (Model 1) for $AgTaO_3$, $CuTaO_3$ and $CuTa_2O_6$ films, and the experimental coefficients of friction for $AgTaO_3$ and $CuTa_2O_6$ films, measured at 750 °C. The friction trends from MD and experiment are in agreement: $f^{\text{MD \& Exp.}}_{AgTaO_3} < f^{\text{MD}}_{CuTaO_3} < f^{\text{MD \& Exp.}}_{CuTa_2O_6}$. Note that the friction results from MD and experiment can not be quantitatively compared due to the inherent size-scale difference between the two techniques, where contact area and applied load in MD are orders of magnitude smaller than those in experiment. Also, in MD, strong surface adhesion at the nanoscale tends to result in larger CoF at the sliding interface [151]. However, the ratios of the friction forces and CoFs for $AgTaO_3$ and $CuTa_2O_6$ can be directly compared, and both experiment and simulation yield $3 < f_{CuTa_2O_6}/f_{AgTaO_3} < 4.5$.

It was previously shown that the CoF of $AgTaO_3$ decreases with temperature (Chapter 3, 4 and 5). Here we investigated the effect of temperature on friction for $CuTa_2O_6$ with both MD and experiment. As shown in figure 7.4(b), the friction decreases with increasing temperature, exhibiting the same trend as $AgTaO_3$.

7.3.2 Wear

To quantify the wear performance of these materials, the MD ball-on-plate model (Model 2) was used since it allows the removal of atoms from the wear track so wear depth can be measured. Figure 7.5(a) shows that the wear depth for each material at 750 °C increases significantly at the beginning of sliding (run-in) and then approaches a steady state. The wear depth varies as $d_{AgTaO_3} > d_{CuTaO_3} > d_{CuTa_2O_6}$, opposite to the friction trend. The experimentally-measured wear rates at the same temperature, shown in figure 7.5(b), exhibit the same trend as that from MD, indicating that $AgTaO_3$ is more easily removed from the wear track than $CuTa_2O_6$.

7.4 Discussion

The MD and experimental observations of opposing friction and wear trends suggest that all three materials share similar sliding mechanisms. In Chapter 3, 4, 5 and 6, we proposed that the CoF and the wear rate are determined by the ability of the monovalent metal (in this case Ag or Cu) to migrate to the surface and agglomerate into soft metallic clusters. In this section, we investigate

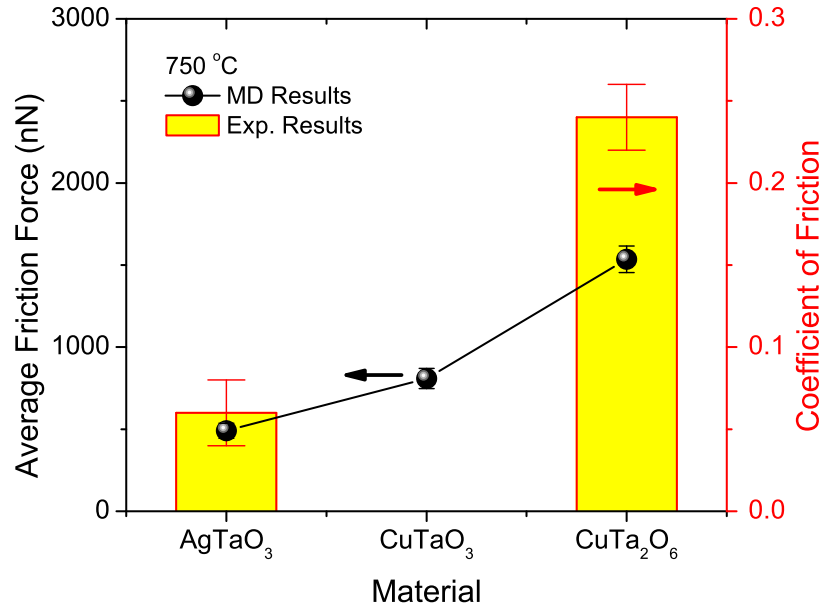

(a)

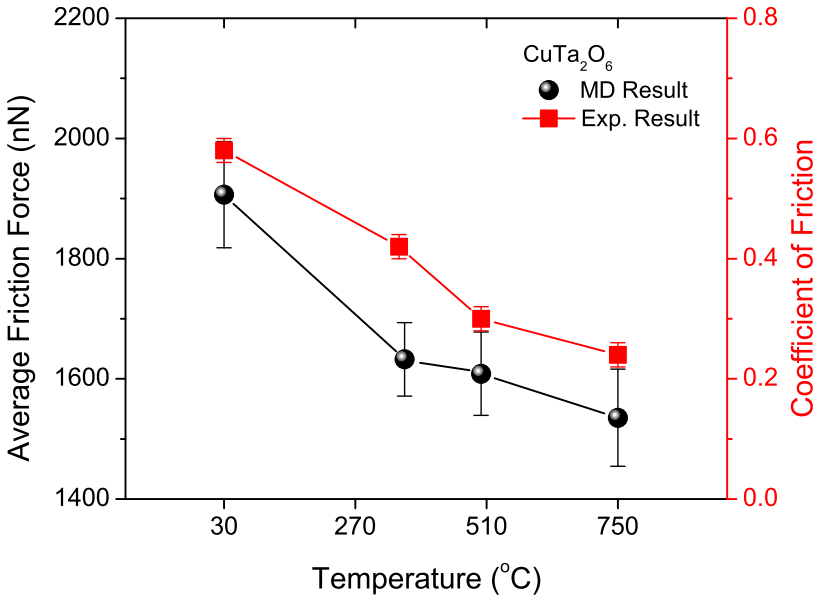

(b)

Figure 7.4: Friction from MD and experiment as functions of (a) material (i.e. $AgTaO_3$, $CuTaO_3$ and $CuTa_2O_6$ in MD; and $AgTaO_3$ and $CuTa_2O_6$ in experiment), and (b) temperature (i.e. RT, 350, 500 and 750 °C).

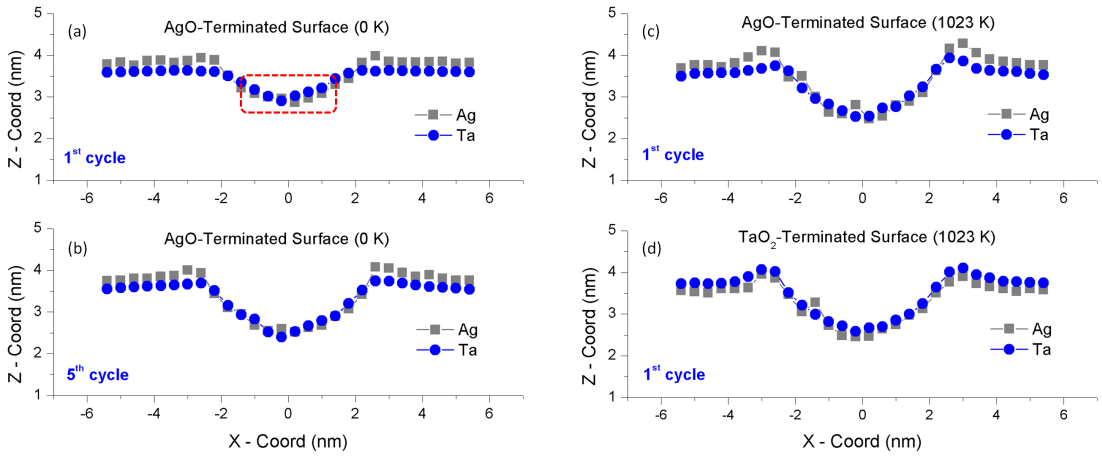

(a)

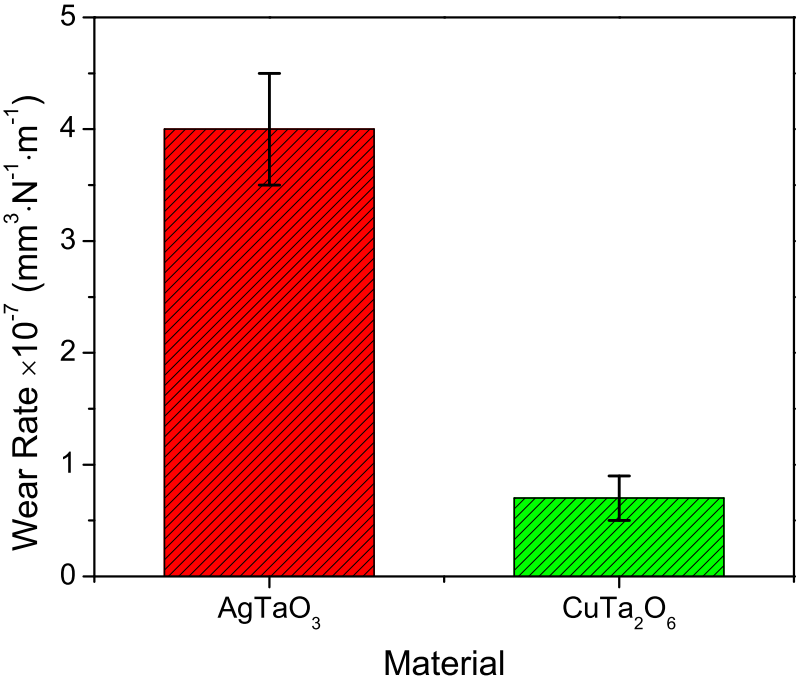

(b)

Figure 7.5: Wear performance of (Ag/Cu)-Ta-O at 750 °C: (a) MD-predicted wear depth and (b) experimentally-measured wear rate.

the ability of this mechanism to explain the observed trends. Analyses of the results of (1) surface elemental mapping from experiment (see Appendix A.6), (2) Ag/Cu clustering at the interface in MD, and (3) Ag/Cu migration on the film surface using DFT (see Appendix A.7), were conducted.

7.4.1 Ag/Cu Clustering

We quantified the evolution of the materials in response to sliding with particular focus on formation of Ag and Cu clusters. In Chapter 3, 4, and 5, we showed that Ag clusters were formed in the process of $AgTaO_3$ film restructuring. Figure 7.6 shows the number of Ag and Cu clusters formed in the $AgTaO_3$ and $CuTaO_3$ films from Model 1 at 750 °C. The two curves increase at the beginning of sliding, typical of a run-in process, and both reach a steady state after ~ 1 ns. At this steady state, the number of Cu clusters was about half of that of Ag, even though the initial amount of Ag and Cu in each film was equivalent. This result indicates that, under the same sliding conditions, Cu is less likely to segregate and form clusters than Ag. Since the film lubricity largely depends on the presence of the metallic Ag/Cu phase on the surface, the formation of clusters relates to the friction result shown in figure 7.4(a), where $CuTaO_3$ exhibits higher friction than $AgTaO_3$. However, Ag clusters with high mobility have low wear resistance, which results in more significant wear on $AgTaO_3$ compared to $CuTaO_3$.

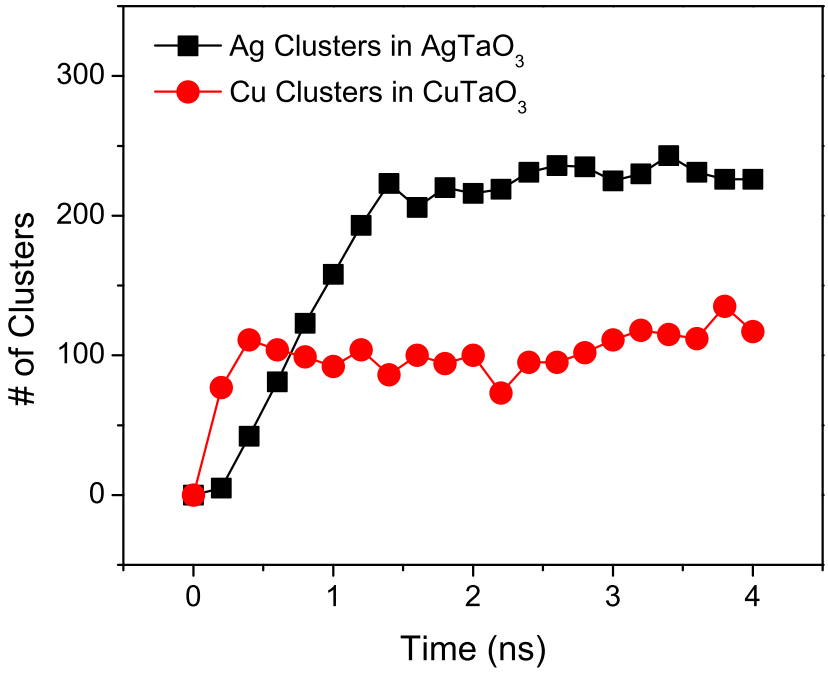

Figure 7.6: The number of Ag/Cu clusters at the sliding interface of $AgTaO_3$ and $CuTaO_3$ at 750 °C as a function time.

For $CuTa_2O_6$, the same criteria was applied to measure the number of Cu clusters. However, only a few Cu clusters were found even after the system reached a steady state (not shown). One likely reason is that the initial Cu content in $CuTa_2O_6$ is half that of Ag or Cu in the ABO_3 perovskites for the same model size. Regardless, the simulations show that Cu is less likely to form clusters in the interface than Ag. This is consistent with the experimental observation that Cu is more uniformly distributed in the wear track on $CuTa_2O_6$ than was found in a previous analysis of

Ag in the wear track on $AgTaO_3$ [2].

7.5 Conclusions

In this work, we studied the tribological performance of three ternary oxide materials: $AgTaO_3$, $CuTaO_3$ and $CuTa_2O_6$. MEAM potential parameters for Cu-Ta-O were obtained by fitting to DFT calculations of structural and elastic properties. These potentials were then used in subsequent MD sliding simulations of $AgTaO_3$, $CuTaO_3$ and $CuTa_2O_6$. The MD predictions of friction and wear properties were compared with results of experimental tribotests on $AgTaO_3$ and $CuTa_2O_6$ films at elevated temperatures up to 750 °C. The MD and experimental trends were consistent for both friction ($AgTaO_3 < CuTaO_3 < CuTa_2O_6$) and wear ($AgTaO_3 > CuTaO_3 > CuTa_2O_6$). The wear performance was significantly improved when Ag was substituted by Cu, but at the expense of higher friction. Further analysis of the sliding mechanisms revealed that the friction increase and wear decrease could be attributed to the formation of fewer Cu clusters at the sliding interface, relative to Ag. This was corroborated by DFT calculations, which showed that energetic barrier for migration of Cu atoms on the CuO-terminated surface of $CuTaO_3$ is considerably higher than for the equivalent sliding of Ag on $AgTaO_3$. This observation supports the hypothesis that the same friction and wear mechanisms reported for $AgTaO_3$ apply to $CuTaO_3$ and $CuTa_2O_6$, and explains the opposing friction and wear trends. Comparison of the three ternary materials enabled us to identify the key effects of the identity and relative concentration of the noble metal on tribological performance. These observations provide insights useful for developing new solid lubricants for high-temperature applications.

Chapter 8

Pressure Dependence of the Interfacial Structure of Potassium Chloride Films on Iron

8.1 Introduction

The registry between a film and substrate has a profound influence on interfacial shear. A film that is in registry with the substrate will result in the largest friction force since all the atoms at the interface will simultaneously surmount the sliding potentials. Conversely, a lack of commensurability between the atoms in the contacting interface would lead to a lower shear strength which does not scale linearly with contact area [152–156]. For thin films, commensurability may be dependent on the thickness of the film and, in the case of confined films, pressure. Therefore, understanding the friction properties of an interface requires first understanding the dependence of film structure on thickness and pressure.

This complex relationship has been explored using a simple alkali halide as a model boundary lubricating film. While alkali halides are not used as commercial boundary films, their structural simplicity and the availability of a wide range of alkali halides with varying lattice constant, along with their chemical inertness make them attractive candidates for fundamental study [157]. In particular, the shear strength S of KCl films has been measured experimentally in ultrahigh vacuum (UHV) where it is found that S varies linearly with contact pressure P:

$$S = S_0 + \alpha P, \tag{8.1}$$

where S_0 is the shear strength at zero pressure and α is typically assumed to be a constant [158–161]. Such linear variations in interfacial shear strength as a function of contact pressure are relatively common in tribological systems [158, 160, 161]. The specific system explored in the current study is KCl on Fe(100), which is particularly well suited for such research since precise interaction potentials for computational models are already available for alkali halide films and it is relatively straightforward to prepare well-defined films in ultrahigh vacuum by KCl evaporation.

This model system has previously been investigated using DFT calculations of KCl films on an Fe(100) substrate [162]. However, the requirements of using periodic boundary conditions for

the calculations necessitated modeling KCl films that were in registry with the iron substrate. Since the lattice mismatch between KCl and the 100 face of iron is significant (~7 %), the resulting KCl film is strained. Nevertheless, these calculations revealed a relatively low barrier in sliding the KCl film against Fe(100) of 0.7 kJ/mol that yielded a calculated shear strength that was in good agreement with experiment. In this case, it was proposed that the pressure-dependent shear strength arose because of the vertical motion of the atoms in the contact as they slid from one stable site to the next over an energy barrier, analogous to the barrier height in the Prandtl-Tomlinson (PT) model (an brief description of PT model can be found in Section 10.2) for sliding friction [163–168]. However, the low value of the sliding potential implies that the KCl film does not have a strong site preference on the Fe(100) substrate suggesting that KCl might not, in fact, be in registry with the Fe substrate and also emphasizes the need for accurate potentials to describe sliding friction.

Although these results show that the previous DFT calculations yield a potential barrier that is in good agreement with the experimentally measured shear strength for KCl films, there are limitations to the predictions that can be made using this approach given the relatively small simulation size and required periodic boundary conditions which force registry. This suggests the use of molecular dynamics simulations, which have been extensively used to explore the structural and tribological properties of sliding solid-solid interfaces [61, 123, 169–174]. Such simulations have proven extremely useful in helping to understand the behavior of buried interfaces that, in most cases cannot be interrogated directly. However, MD simulations often use generic interface potentials that have been optimized to provide reasonable agreement with the experimental results for a wide range of materials, rather than precisely mimicking the behavior of a specific material. When the interfacial structure is controlled by small energy differences, as is the case in the KCl-Fe system, this may result in the prediction of erroneous structures and the resulting properties. Since it is not generally possible to experimentally interrogate the buried sliding interface, the results of such simulations cannot be directly compared with experiment except to compare predicted parameters such as friction force with the experimental value. It is therefore desirable to tune the interaction parameters in the MD simulation to reproduce experimentally measurable film properties measured for the film-surface interface and then use the tuned simulation to provide information about that interface not available via experiment. This is the approach taken in this work. We adjust the interaction potentials between a model alkali halide boundary film on an Fe(100) substrate by comparison with the results of temperature-programmed desorption (TPD) experiments of the desorption behavior of the films. The structure of thin KCl films is then further characterized experimentally using low-energy electron diffraction (LEED) [175] measurements. Finally, the MD simulations,with interaction potentials fitted to the TPD data, are used to explore the influence of contact pressure on the interfacial structure. (All the experimental results in this chapter are provided by our colleagues *D. Olson* and *W.T. Tysoe*.)

8.2 Methodology – Two Fe-KCl Model Systems

Two computational models were created as shown in figure 8.1. Both models contain an Fe substrate with dimensions of $12.0 \times 12.0 \times 0.6$ nm^3. A small slab of an m-layer (m = 1, 2, ... ,14) KCl film with in-plane dimensions of 4.72×4.72 nm^2 was placed in the center of the Fe. In Model 1, shown in figure 8.1(a), the top surface of the KCl was free. In Model 2, shown in figure 8.1(b), a rigid Fe plate, with the same orientation as the bottom Fe surface, was placed on top of the KCl film.

During the simulation, the outermost atomic layer of Fe was held fixed. In both models, periodic boundary conditions were applied in the plane parallel to the Fe-KCl interface. Both models were equilibrated by running dynamics for 0.5 ns until the potential energy of the system reached a constant value. Then, the KCl lattice was characterized throughout the film by measuring the distance between all adjacent K (or Cl) atoms in each KCl layer, and then fitting the distribution of the data to a Gaussian function to obtain the mean lattice constant (for the standard unit cell of the NaCl (B1) structure) and its standard deviation. Model 2 was used to investigate the effect of pressure with normal loads of 0.014, 0.14, 1.41 and 14.1 nN applied to the top plate, corresponding to contact pressures of 0.63, 6.30, 63.0 and 630 MPa. The system was equilibrated for 1 ns after each load was applied. We partially validated this model by calculating the Poisson's ratio and elastic modulus from the change in the normal and in-plane dimensions of the innermost four layers of the 8-layer KCl model due to an increase in pressure from 6.3 to 630 MPa. The model predicted a Poisson's ratio of 0.194 and an elastic modulus of 44.8 GPa, which are reasonably consistent with the bulk properties of KCl (Poisson ratio= 0.216; elastic modulus = 38.2 GPa).

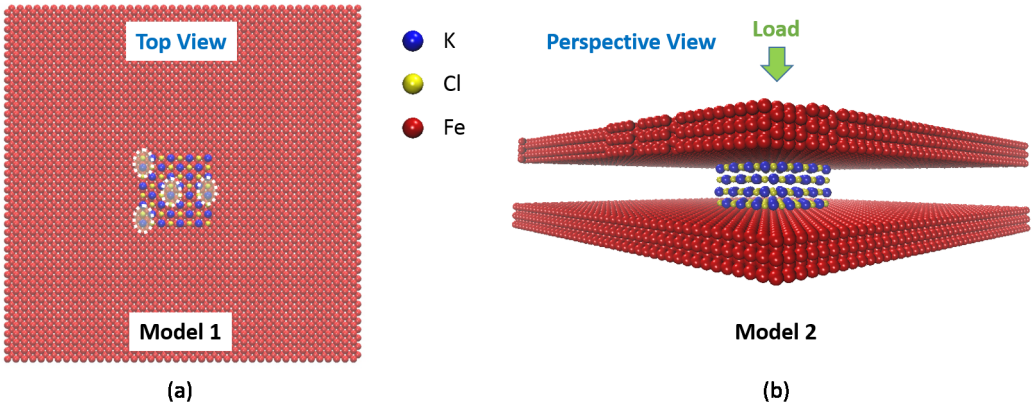

Figure 8.1: Snapshots of the two MD models. (a) In Model 1, the top surface of the KCl is free. White dashed circles identify representative positions (i.e. film center, edge center, K- and Cl-terminated corners) from which KCl was removed to calculate activation energy. (b) The KCl film is confined between two Fe plates in Model 2 with varying normal loads applied to the upper plate.

The desorption activation energy (E_a) was calculated using Model 1 from the difference in potential energy of the system before and after removing a single KCl pair. E_a was calculated using the equation [176]: $E_a = E_{N-1,KCl-Fe} + E_{1,KCl} - E_{N,KCl-Fe}$, where $E_{N,KCl-Fe}$ and $E_{N-1,KCl-Fe}$ are the potential energies of the system before and after the removal of KCl, respectively, and $E_{1,KCl}$ is the energy of one KCl at equilibrium. The values of $E_{N,KCl-Fe}$ and $E_{N-1,KCl-Fe}$ were calculated directly from the simulation after energy minimization. However, this approach could not be applied to $E_{1,KCl}$ because the empirical potential was fit to crystalline KCl and therefore not expected to be able to predict gas-phase energies, which is the state of the KCl as it is desorbed in the experiment. To address this, we assumed that E_a from MD and experiment should be the same for sufficiently large films, i.e. where the Fe interaction has no effect on activation energy, and the value of the calculated $E_{1,KCl}$ was adjusted such that the activation energy of the 2.5 nm thick film was the same in the experiment and simulation. We initially tested removing KCl from four different positions on

the film, i.e. film center, edge center, and the K- and Cl-terminated corners; see figure 8.1(a). The results showed that, for any film thickness, the smallest E_a was always calculated from the model where we removed KCl from one of the two corners. This is consistent with 1/2 order dependence of the activation energy from the TPD experiment (see Appendix A.8) which suggested atoms were removed from the edge of the KCl slab. Therefore, in subsequent calculations, E_a was identified as the smaller of the values calculated from the two corner positions.

Multiple empirical potentials were used to describe the atomic interactions for the system. The Born-Mayer-Huggins (BMH) [177] potential was used to model interactions within the KCl, with potential parameters from Ref. [178]. The Embedded-Atom Method (EAM) [179, 180] was used to describe Fe, with potential parameters from Ref. [181]. Interactions between KCl and Fe were modeled using the Morse potential: $E = D_0[e^{-2\alpha(r-r_0)} - 2e^{-\alpha(r-r_0)}]$, where D_0 is the potential well depth, r is the distance between each atom pair, r_0 is the equilibrium distance, and α is the exponential parameter that controls the width of the potential well. The potential parameters were tuned by matching the MD-predicted activation energies with the corresponding experimental results.

8.3 Results and Discussion

8.3.1 KCl-Fe Pair Potential Fitting

The experimentally-measured activation energy (see Appendix A.8) was used to tune the Morse potential parameters that describe the interactions between KCl and Fe in the MD simulations. We started with thick films, for which the activation energy was unaffected by the iron substrate and therefore determined only by the KCl potential. As shown in figure 8.2, the activation energy of the simulation and experiment are the same for the thickest films (~2.5 nm). As the film thickness decreased, the activation energy decreased and the rate of this decrease was determined in the simulation by the KCl-Fe potential. The initial Morse parameters (D_0, α and r_0) were obtained by reproducing the change of energy with distance between KCl and Fe slabs from the previous DFT calculations [162,182,183]. We then tuned the minimum energy for the K-Fe and Cl-Fe interactions ($D_{0,K-Fe}$ and $D_{0,Cl-Fe}$) to match the experimentally measured activation energy for films between 0.3 and 1.2 nm thick. The other two parameters (α and r_0) were unchanged from their initial values ($\alpha_{K-Fe} = 9.8$ nm^{-1}, $r_{0,K-Fe} = 0.421$ nm, $\alpha_{Cl-Fe} = 14.0$ nm^{-1} and $r_{0,Cl-Fe} = 0.270$ nm). We observed that activation energy increased monotonically with increasing KCl-Fe interaction strength and that the rate of that increase was faster for thinner films and for stronger interactions. The best fit values of the minimum energy parameter were found to be: $D_{0,K-Fe} = 0.67$ kJ/mol and $D_{0,Cl-Fe} = 8.74$ kJ/mol. Note that we did not model films with thicknesses smaller than the lattice constant of a single layer since those corresponded to experimental measurements of partial films which could not be reproduced reliably in the simulations. Figure 8.2 shows that the activation energy predicted from MD using the best fit Morse parameters for films at least one layer thick was in good agreement with the values obtained from TPD.

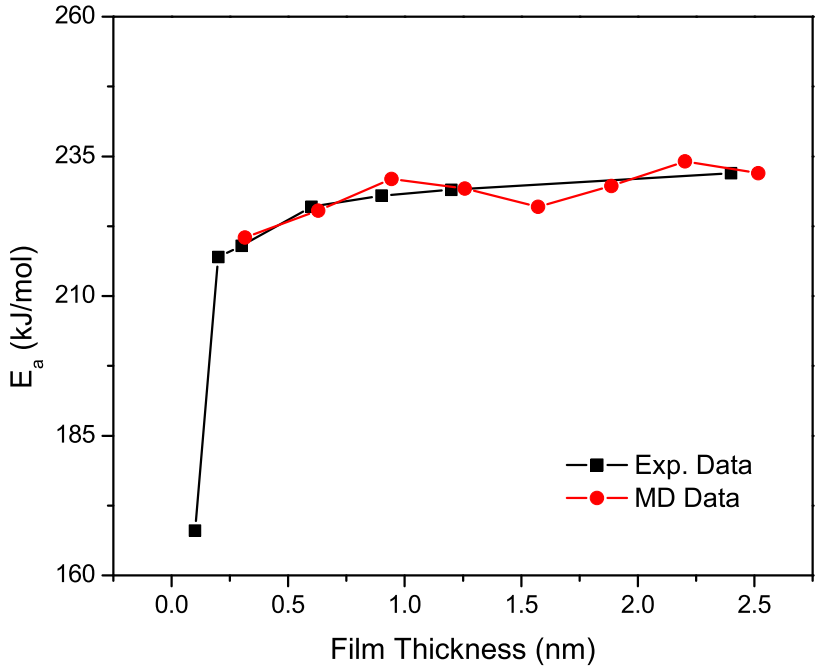

Figure 8.2: MD-predicted and experimentally-measured activation energies as functions of film thickness.

8.3.2 KCl Film with A Free Surface

In the simulations, Model 1 was used to study the equilibrium structure of KCl films between 1 and 14 layers thick. Because of the atomic level detail available in the simulation, we were able to observe the variation of this structure, both between and within the KCl layers in a given film. Therefore, we characterized the distribution of in-plane lattice constants for each film, using a Gaussian fit to estimate mean values and their standard deviations. Figure 8.3(a) shows a representative distribution and fit for eight-layer KCl. In this case, the mean lattice constant is comparable to the value predicted for the bulk material using the BMH potential (0.625 nm) and the standard deviation is small, indicating that most of the film conforms to the bulk material structure. The mean of the lattice constant for films between 1 and 14 layers thick is shown in figure 8.3(b). The mean lattice constants of the thicker model films are comparable to that of bulk KCl, consistent with the LEED (see Appendix A.9) pattern for KCl films of two monolayers and thicker. Note that the mean values reported here were calculated from Gaussian fits to atom positions throughout the film, including the edges of the film where variation from bulk structure is expected. Recalculation using only the middle 75 % of the films yielded slightly smaller error bars, but similar mean values and the same trends.

Figure 8.3(b) also shows that, as the film thickness decreases, so too does the mean lattice constant of the film. For the two-layer film, the mean lattice constant is 0.611 nm, which is between

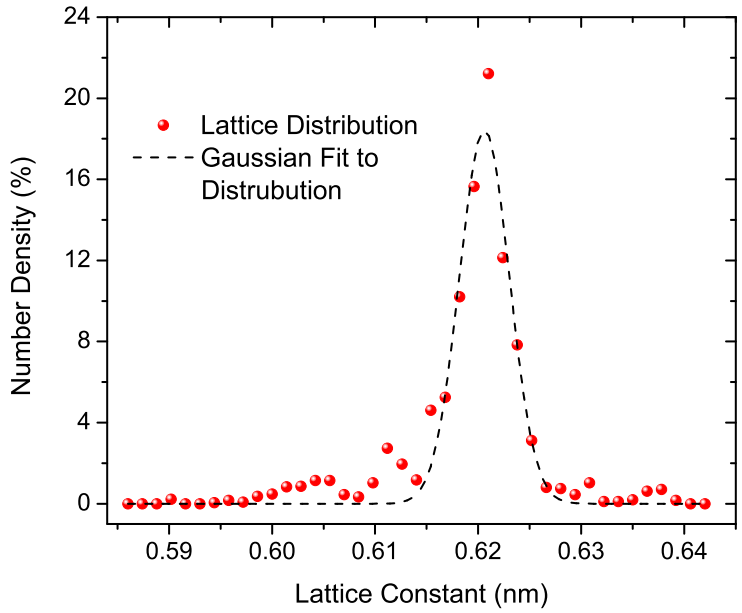

(a)

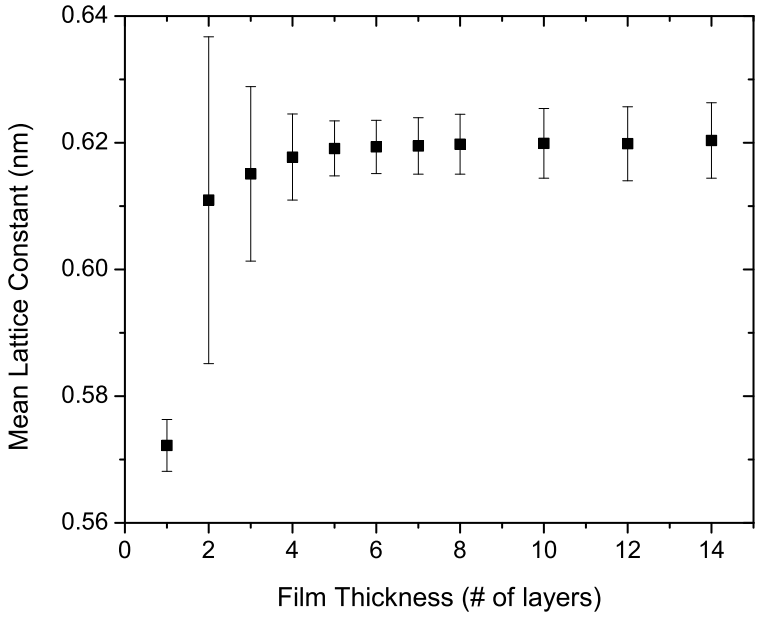

(b)

Figure 8.3: (a) Distribution of in-plane lattice constants within an eight-layer KCl film, fit to a Gaussian function to enable calculation of the mean and standard deviation. (b) Mean in-plane lattice constant for KCl films of varying thickness.

that of bulk KCl and bulk Fe. This result differs from the LEED pattern which indicated that the two-layer film exhibited the bulk KCl lattice. Also, there is significant variation of the structure within and between the two layers of KCl. This is reflected by the large error bar for this case in figure 8.3(b). It can also be observed from the distribution of the lattice constants in each layer of the model film, which is shown as a contour plot in figure 8.4 for a smaller KCl patch (2.2 nm × 2.2 nm) to highlight key trends. The contour plot for each layer was generated by calculating the in-plane mid-point position and the in-plane distance between each pair of adjacent K (or Cl) atoms. The color on the plots represents the magnitude of the distance (lattice) at each mid-point position, with color between the calculated values obtained using interpolation.

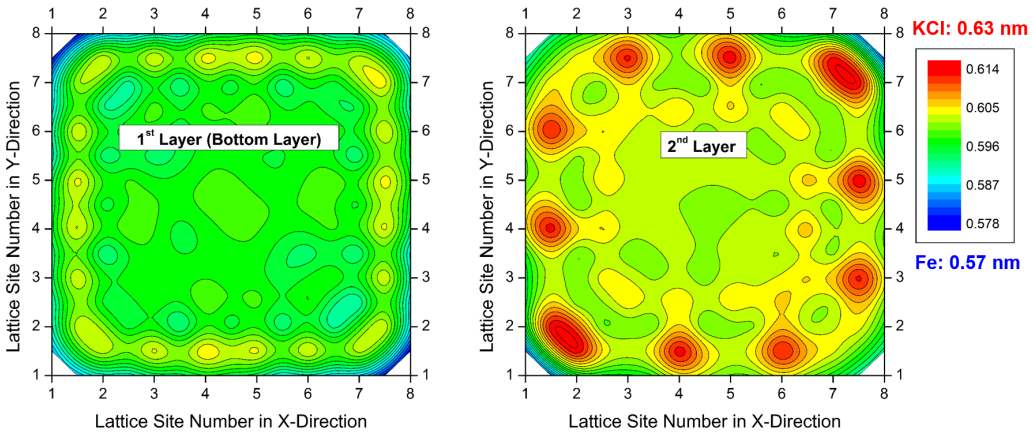

Figure 8.4: Contour plots of the in-plane lattice in each of the two layers of two-layer KCl illustrating the variation of the structure of the film, both within and between the layers.

Figure 8.4 shows that the first KCl layer (adjacent to the Fe) is predominantly in registry with the Fe, particularly near the center of the film, while the second layer largely reflects the KCl lattice. It is noted that the escape depth for 50-eV electrons used for the LEED measurements is ~0.4 nm and thus predominantly probes just the outermost layer of the KCl film. The difference between the structure of thin films in the experiment and simulation is even more obvious in the single-layer film. In the simulations, the single layer KCl mean lattice constant was found to be 0.572 nm, i.e. similar to bulk Fe, indicating that the KCl is in registry with the Fe substrate. This contrasts with the LEED results which suggest that the single layer KCl lattice is larger than that of both bulk Fe and KCl. We were unable to reproduce this observation with any values of the Morse parameters: with strong interactions, the KCl was in registry with the Fe as expected for the Morse pair potential; but with weak interactions, the BMH potential that was fitted to bulk KCl was unable to maintain the single layer structure resulting in a buckling of the film. This issue might be addressed by using a non-pairwise, or location dependent KCl-Fe potential, but is out of the scope of this study.

8.3.3 Effect of Pressure on Interfacial Structure

Next we used the simulations to explore the effect of pressure on the structure of KCl confined between two Fe surfaces (Model 2). We analyzed only films with four layers or more since, as shown in Section 8.3.2, thinner model films exhibited structures that differed from the LEED measurements. First we analyzed the variation of structure across the film. The mean in-plane lattice in each layer of an eight-layer KCl slab as a function of load is shown in figure 8.5. At any load, the smallest lattice is observed in layers adjacent to the Fe and the largest in the middle of the film. Comparing the structure of the film at the two loads, we observe that the mean lattice constant of the outermost layers decreases with load while that of the innermost layers increase with load. This suggests that, as load increases, the outermost KCl layers are forced into registry with the Fe, and that the inner KCl layers respond to this strain by expanding. The net effect is that there is a slight increase in the overall lattice of the film as the load increases (see dashed lines in figure 8.5).

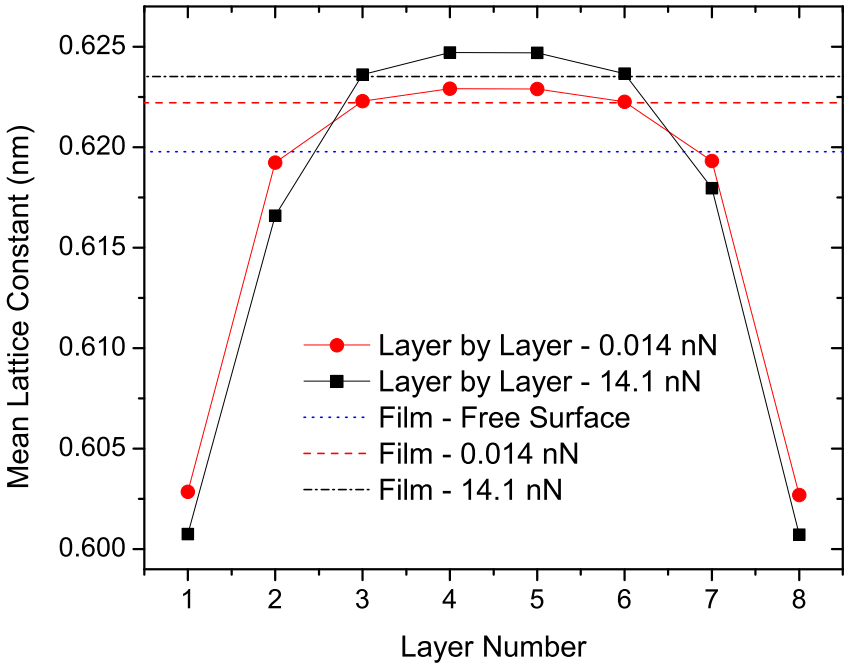

Figure 8.5: Structure of the eight-layer confined KCl film at two different normal loads. Points represent the mean in-plane lattice constant in each layer of the film where layers 1 and 8 are adjacent to the Fe, and dashed lines represent the overall mean in-plane lattice of the confined film (Model 2) subject to load and with one free surface (Model 1).

These trends are illustrated in another way in figure 8.6, which plots the effect of load on the in-plane lattice averaged over the entire eight-layer film, and only the innermost two layers or only the outermost two layers; the mean lattice constant of the free surface film is also shown for reference. Consistent with the trends shown in figure 8.5, we observe that the overall mean lattice

constant of the confined film is larger than that of the free surface film at any load, and increases slightly with increasing load. This trend is attributable to combined effects of the load-induced increase in the lattice constant of the inner layers and decrease of the lattice constant in the outer layers.

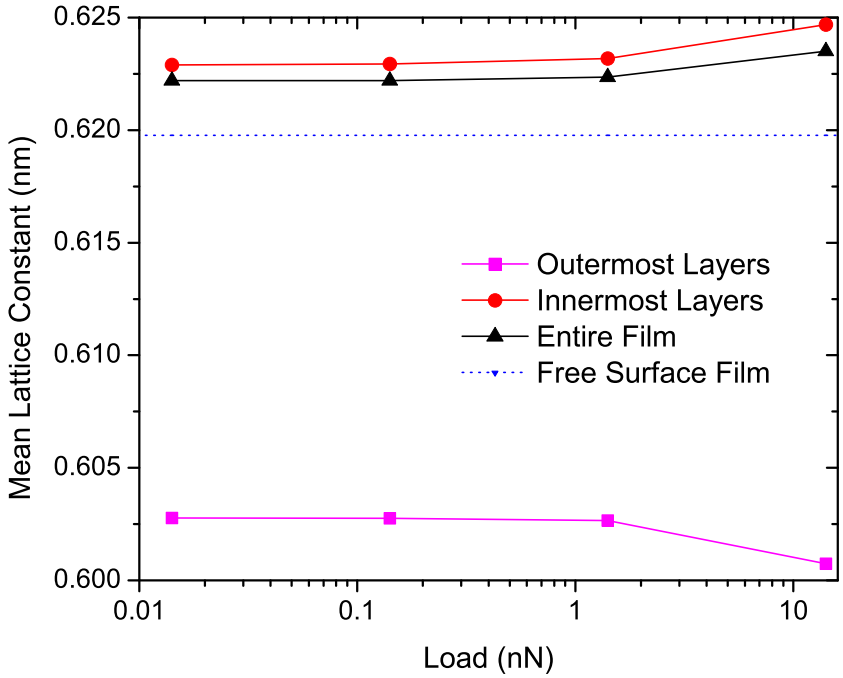

Figure 8.6: Variation of the mean in-plane lattice constant of the KCl films due to load. The mean in-plane lattice constant is reported for the entire film and for the innermost and outermost layers of that film. The free surface film (Model 1) in-plane lattice constant is shown for reference.

The trends observed for the eight-layer case are also exhibited by the other films. The percent change in the in-plane lattice due to confinement and due to an increase in load by a factor of 1,000 for films up to fourteen layers thick is shown in figure 8.7. The hollow symbols represent the change in the lattice of just the outermost layers, which is negative (smaller lattice) for all films and is relatively constant with varying film thickness. The effect of confinement and load on the overall mean lattice, however, is affected by film thickness. Except for the four-layer film, the change in mean lattice is positive (larger lattice) due to both confinement and load, and these effects increase with film thickness, approaching a constant value above approximately ten layers. Although all of these changes are very small (< 1 %), since the thicker films have more inner layers, the trends are consistent with the suggestion that load is partially accommodated by expansion of the inner layers of a confined film.

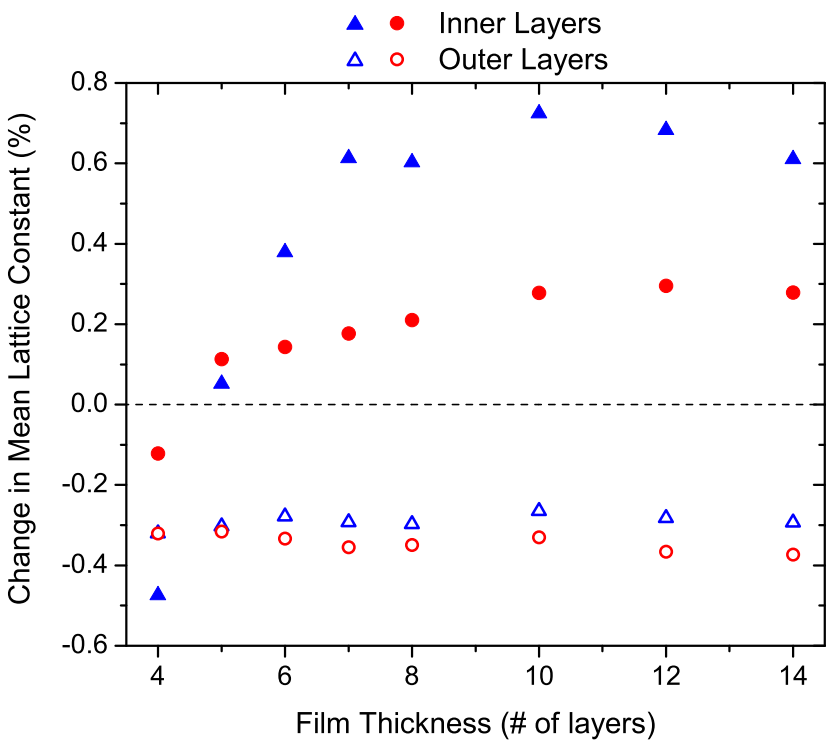

Figure 8.7: Change in the mean in-plane lattice constant of a film (solid symbols) and outermost layers (hollow symbols) of that film due to confinement (blue triangles) and a 1,000 fold increase in load (red circles).

8.4 Conclusions

A simple model system consisting of KCl films on a clean iron surface was used to investigate the effects of thickness and pressure on film structure. The study was performed with both experiments (conducted by our colleagues *D. Olson* and *W.T. Tysoe*) and molecular dynamic simulations. The simulations used existing empirical potentials to describe the KCl film and Fe substrate, but the critical interactions between the film and substrate were tuned to match the corresponding experimental system. This was accomplished by performing TPD measurements and fitting that data to a rate equation to yield film thickness-dependent desorption activation energy (conducted by our colleagues *D. Olson* and *W.T. Tysoe*). The desorption activation energy was then predicted by the simulations, and the minimum energy in the pair potential that was used to describe the KCl-Fe interactions was tuned such that the model predictions were consistent with the data obtained from experiment.

Simulations of films at least four layers thick were then used to investigate the effect of pressure on film and interface structure. Pressure was found to decrease the lattice constant of the outermost layers of the film while increasing the lattice constant of the film's inner layers. These trends were observed for all films, where the effect of pressure on the inner layer was more

significant for thicker films. These results suggest an additional possible origin for the pressure-dependence of shear strength. It was previously suggested that the vertical motion associated with sliding from one potential minimum to the next on the surface resulted in additional external work being carried out on the system, thereby yielding a pressure-dependent shear strength. However, the above simulations, combined with the experimental results for the film-vacuum interface, suggest an additional possibility, that of a change in interfacial registry at higher contact pressures. Since the shear strength has been found to increase when the boundary film and the substrate are in registry, the increasing registry between the film and substrate at higher pressure can also be expected to result in an increase in shear strength with pressure. Clearly, both effects can occur simultaneously and MD simulations of sliding are currently being carried out to explore these effects as well as the influence of interfacial dynamics on the registry between the film and substrate.

Chapter 9

Identification of the Shear Plane during Sliding of Solid Boundary Films

9.1 Introduction

The friction force of a sliding interface is dominated by the properties of the shear plane. Shear in sliding contacts can occur either at the interface between the two contacting materials or within one of the materials. The location of the shear plane is determined by the strength of the possible sliding interfaces, where sliding will occur at the weakest interface [184]. In many sliding systems, the shear plane is unambiguous since the weakest interface is that with the smallest contact area, which is often at the interface between the two materials. However, in thin films grown on a substrate, the contact size is effectively the same within the film as between the film and substrate. In such cases, the shear strength of the interfaces is primarily dependent on the strength of the interactions between atomic layers. Unfortunately, it is generally impossible to directly interrogate thin boundary films located between two sliding solids *in situ*, although shear within the film can be expected to result in transfer of material from one counterface to the other. This implies that theoretical strategies must be used to model the sliding interface and to identify where shear occurs; this is the approach adopted in the following, where sliding is modeled using molecular dynamic simulations.

Generally, the shear strength of an interface is found to obey equation 8.1. The friction coefficient μ is then given by $\mu = S/P$, where S is the shear strength and P is the contact pressure. This leads to the following formula: $\mu = S_0/P + \alpha$ and, depending on the relative values of S_0 and α, can lead to friction coefficients that are relatively independent of contact pressure. Equation 8.1 can be interpreted in terms of a Prandtl-Tomlinson model and this is discussed in greater detail below. However, other effects could produce pressure-dependent shear strengths, particularly those arising from structural changes caused by high contact pressures that influence the registry between the atoms at the shearing interface [185, 186]. This will influence the shear strength since, if the atomic lattices on either side of the shear plane have similar periodicities (that is, they are commensurate or in-registry), the shear strength will be larger than if the atomic lattices on either side of the interface have dissimilar structures (that is, they are incommensurate or out-of-registry) [152–156].

Here we explore this effect using MD simulations of a simple model boundary film consisting of KCl on Fe. As described in Chapter 8, this system can be evaporated in a controlled manner onto

clean metal substrates in ultrahigh vacuum (UHV) allowing the structure, energies and tribological properties to be studied on simple model systems [157, 159, 187–192]. The frictional behavior of KCl-Fe systems has been previously studied both experimentally and computationally. Experiments in UHV showed that the shear strength of thin KCl films obeys equation 8.1 with a value of $\alpha = 0.14 \pm 0.02$ [159]. First-principles density-functional theory calculations indicated that the lowest-energy barrier to sliding will occur at the KCl-Fe interface and that the shear strength of that interface will increase linearly with pressure, consistent with equation 8.1 [162, 182]. In Chapter 8, MD simulations were performed to avoid the limitations from the periodic nature in DFT using potentials for the interaction between the KCl films and substrate that were specifically tuned to experimental measurements of the film structure and sublimation energies measured in UHV, rather than using generic potentials. Those simulations showed that the in-plane structure of thin KCl films on Fe surfaces is affected by the magnitude of the applied load.

Based on this, load-induced structural variations in the KCl film could have an effect on the strength of shear planes within the film, and between the film and substrate. This then will influence the location of the sliding plane and the magnitude of the friction during sliding. Here we use MD simulations of a KCl film confined between Fe plates to investigate the role that these effects play on the origin of the commonly observed pressure-dependent shear strengths. To explore this, first we artificially vary the in-plane lattice constant of the KCl as well as the applied load to explore the influence of film structure on friction. We find that sliding can occur either within the KCl film or at the KCl-Fe interface and that the location of the sliding plane is dependent on the load and the KCl lattice structure. These effects are interpreted in terms of the contributions of interlayer distance and interface registry. The findings have important implications for understanding the location of the shear plane and how that changes with load, and on the influence of pressure on the shear strength and corresponding friction of thin boundary lubricating films. We then study the properties of the equilibrium structures of a KCl film to explore how well the simulations parameters reproduce the experimental data and calculate a value of α in equation 8.1 in excellent agreement with previous experiments [159]. This allows the origin of the pressure-dependent shear strength to be analyzed in the framework of the PT model.

9.2 Methodology – Fe-KCl Sliding Model

Figure 9.1 shows the Fe-KCl model system used in the simulations. It consists of a KCl film with three atomic layers confined between two Fe(100) slabs. The in-plane dimensions of the system are 4.72 nm $\times$ 4.72 nm and the initial height of the system is 1.67 nm. In the first set of simulations, the three KCl layers and the two Fe plates are treated as rigid bodies, i.e. the atoms do not move relative to one another. Note that, although this is a dynamics simulation, the fact that the movement of all of the atoms is constrained means that the temperature is effectively zero. Based on our observation that the in-plane lattice constant of KCl layers adjacent to Fe will decrease with pressure [193], we artificially varied the lattice constant of the outermost KCl layers in the model between 0.573 and 0.590 nm while keeping the inner KCl layer lattice constant at its bulk value (0.63 nm). In a second set of simulation, the KCl atoms were allowed to move relative to one another, but the temperature was constrained to near zero to be consistent with the rigid KCl simulation. In all simulations, the lower Fe plate was held fixed and the upper Fe plate was subjected to normal loads between 0.14 and 14 nN. The simulation was equilibrated for 0.5 ns and then the upper Fe plate

was moved laterally at a speed of 5 m/s. The lateral force on the upper Fe plate (friction force) was calculated throughout the simulation. Empirical potentials used in the Chapter are from Chapter 8.

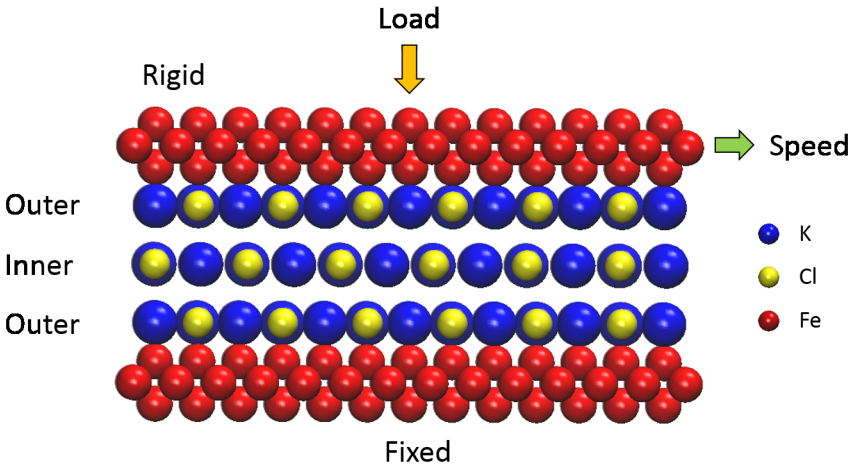

Figure 9.1: Cross-sectional image of the Fe-KCl model system.

9.3 Results and Discussion

9.3.1 Effect of Film Structure on the Shear Plane

We first explore the effect of KCl lattice spacing on friction. Figure 9.2 shows the effect of changing the lattice constant of the outer KCl layers on the maximum (static) friction force at three different loads. We observe three key features: (1) At a given lattice constant, friction increases with load; (2) The friction initially increases and then decreases with increasing lattice constant; and (3) The transition (identified by arrows in figure 9.2) between an increasing and decreasing friction force shifts to smaller values of lattice constant as the load increases.

First, a monotonic increase of friction with load is observed in figure 9.2 at all lattice constants except those near the transition points, where the location of the sliding plane changes, as discussed next. The trend of a friction increase with load is in accord with equation 8.1 and the origin of this effect will be discussed in the next section in terms of the P-T model [163, 164, 194, 195].

The second trend, that friction increases and then decreases with lattice spacing, is directly related to a change in the location of the shear plane with applied load. Sliding could occur either between the inner and outer KCl layers (within the KCl film) or between the outer KCl layers and Fe. Figure 9.3 shows the position of the shear plane as a function of lattice constant where the two possible shear planes are highlighted in the inset images. At small lattice constants, shear occurs within the KCl film, corresponding to the region where the maximum friction is increasing with lattice spacing in figure 9.2. However, at large lattice constants, shear occurs between the KCl and Fe,

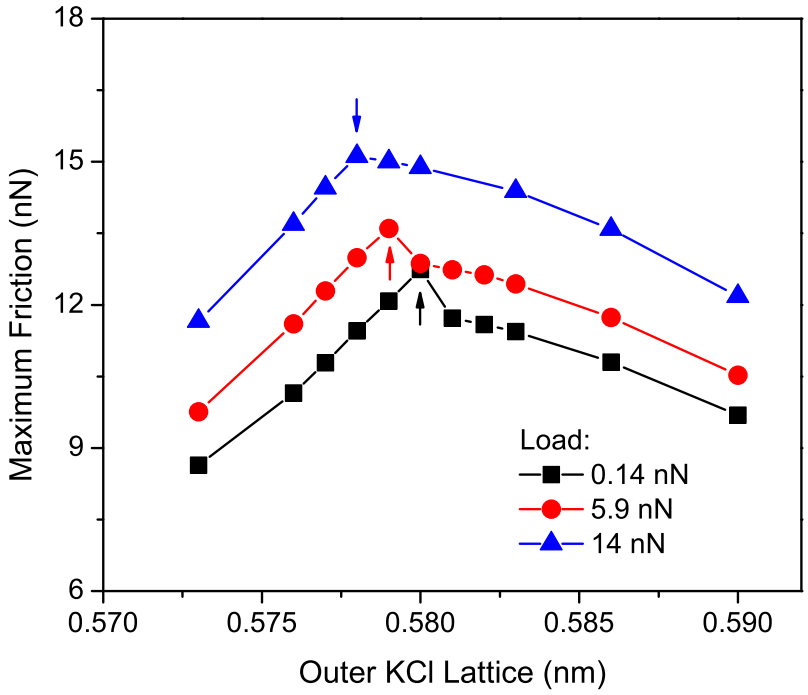

Figure 9.2: Maximum friction as a function of the in-plane lattice constant of the outer KCl layers for three different loads. Arrows indicate the transition from sliding within the KCl to between the KCl and Fe.

corresponding to the region where the maximum friction decreases with lattice spacing in figure 9.2.

The transition from shear within the KCl film to shear at the KCl-Fe interface must be due to a strengthening of the KCl-KCl interface and/or a corresponding weakening of the KCl-Fe interface with increasing outer KCl lattice constant. This can be explained by an increase in registry at the KCl-KCl interface or a decrease in registry at the Fe-KCl interface since, as the outer-layer KCl lattice spacing increases, it becomes closer to that of bulk KCl (and of the inner layers of the KCl film) and further from that of Fe. This change is quantified by comparing the lattice mismatch, the percent difference between the in-plane lattice constants of two adjacent atomic layers. It is known that even small deviations from perfect registry (zero lattice mismatch) can significantly decrease friction [172]. As shown in figure 9.4(a), the mismatch within the KCl decreases with increasing outer KCl lattice constant, while that between the KCl and Fe increases. This is consistent with the friction increasing with outer KCl lattice constant when shear occurs within the KCl film, but decreasing when shear occurs between the KCl film and Fe.

However, if the lattice mismatch were the only effect that influenced the friction force, a shift of the location of the shear plane from within the KCl to between the KCl and Fe would be expected at a much larger lattice spacing than observed in figure 9.2. That is, if only the lattice mismatch

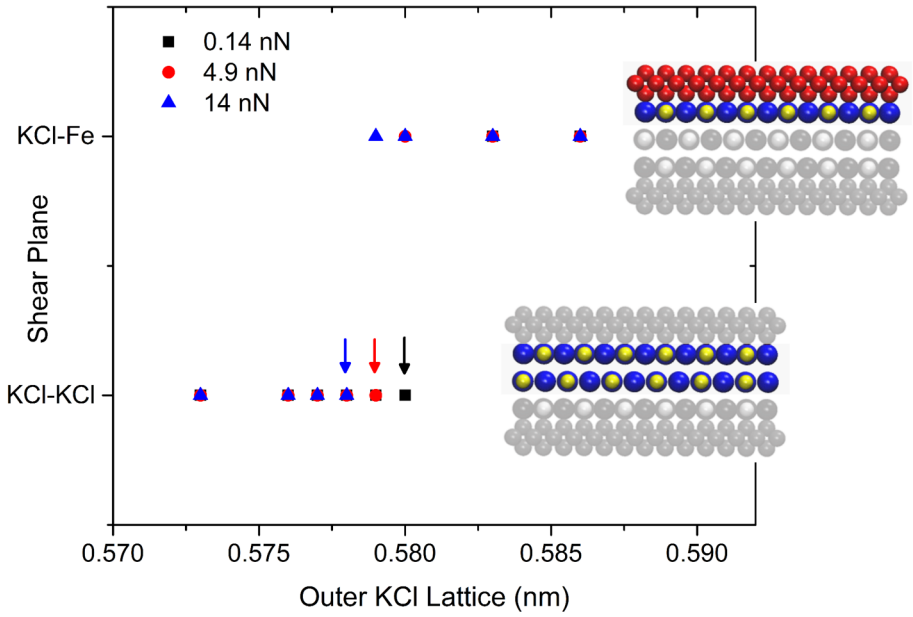

Figure 9.3: Location of the shear plane as a function of the outer KCl lattice constant for three loads. At small lattice constants, shear occurs within the KCl film but, at larger lattice constants, the shear plane moves to between the KCl and Fe. The maximum lattice constant at which sliding occurs within the KCl film at each load is identified by an arrow. Insets show cross-sectional images of the model with the sliding plane highlighted for each case (atom type and color are the same as those in figure 9.1).

alone determined shear strength, we would expect the shift of the position of the shear plane at the outer KCl lattice constant where the two lines in figure 9.4(a) cross one another (which occurs at 0.6 nm). The fact that the transition occurs around 0.578 nm instead means that shear strength of the interfaces is not just a function of registry. A likely contributing factor is the interlayer distance. Figure 9.4(b) shows that the interlayer distance within the KCl film decreases with increasing lattice spacing, while the KCl-Fe interface shows the opposite trend. The interlayer distance affects interface strength, as discussed in more detail in the next section. Therefore, the KCl-KCl interface strengthens as the lattice constant increases, both due to an increase in registry between the layers and a decrease interlayer distance (and vice-versa for the KCl-Fe interface). This is consistent with the observed shift in the sliding plane from within the KCl film to the KCl-Fe interface.

The final trend observed in figure 9.2 is that the KCl lattice spacing at which the friction starts decreasing (due to the transition from sliding occurring within the KCl film to between the KCl and Fe) takes place at smaller lattice constants under larger loads. To explore this effect, we performed additional simulations as a function of load for the case of a small lattice constant (0.576 nm), where sliding occurs within the KCl film under all loads, and for a large lattice constant (0.586 nm), where sliding always occurs at the KCl-Fe interface. Figure 9.5 shows the variation in maximum

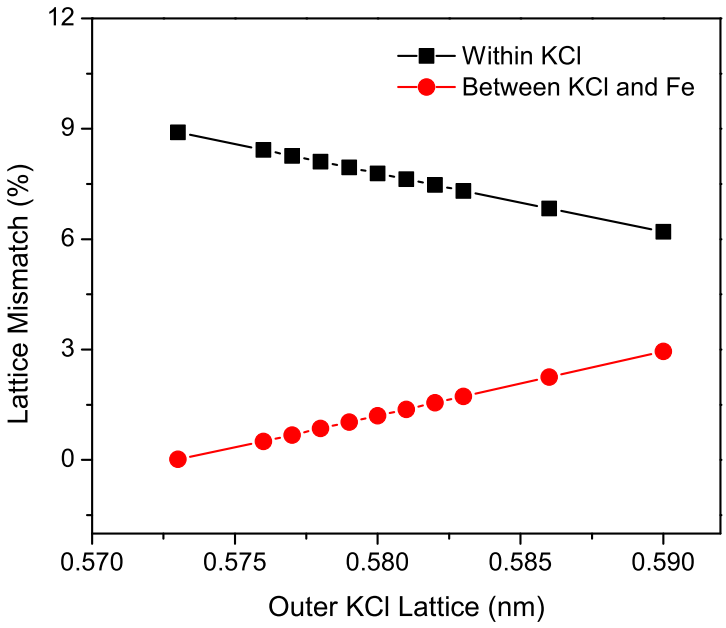

(a)

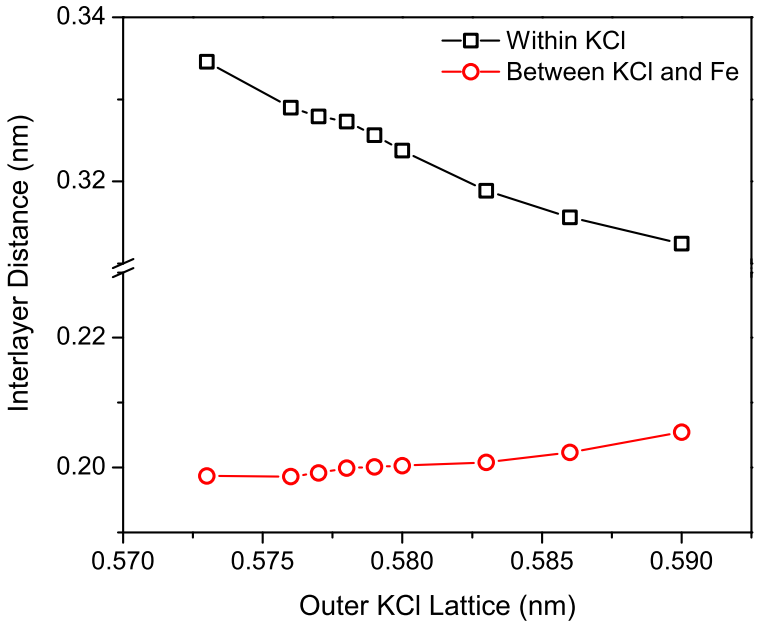

(b)

Figure 9.4: Effect of the in-plane lattice of the outer KCl layers on the (a) lattice mismatch and (b) interlayer distance between the outer KCl layers and the inner KCl layer (black squares) and the Fe (red circles). The interlayer distance shown here is at a load of 14 nN, but similar trends are observed at all loads.

friction for these two cases as a function of load. In both cases, friction increases approximately linearly with load. Linear fits of the data to equation 8.1 are also shown in figure 9.5. Note that, although a linear fit is a reasonable first approximation, it may not fully capture the friction-load relationship [184] and there is evidence for this in figure 9.5 where the friction force for a lattice spacing of 0.576 nm shows deviations from linearity at lower loads. However, assuming a linear relationship enables the two situations to be compared. The fits yield values of α in equation 8.1 of 0.25 and 0.20, for lattice constants of 0.576 and 0.586 nm, respectively. This reveals that the effect of pressure on shear strength is larger when sliding occurs within the KCl than when sliding occurs between the KCl and Fe. This explains the trend found in figure 9.2: as the normal load increases, the shear strength of the KCl-KCl interface increases more rapidly than that of the KCl-Fe interface, and therefore changes the location of the shear plane.

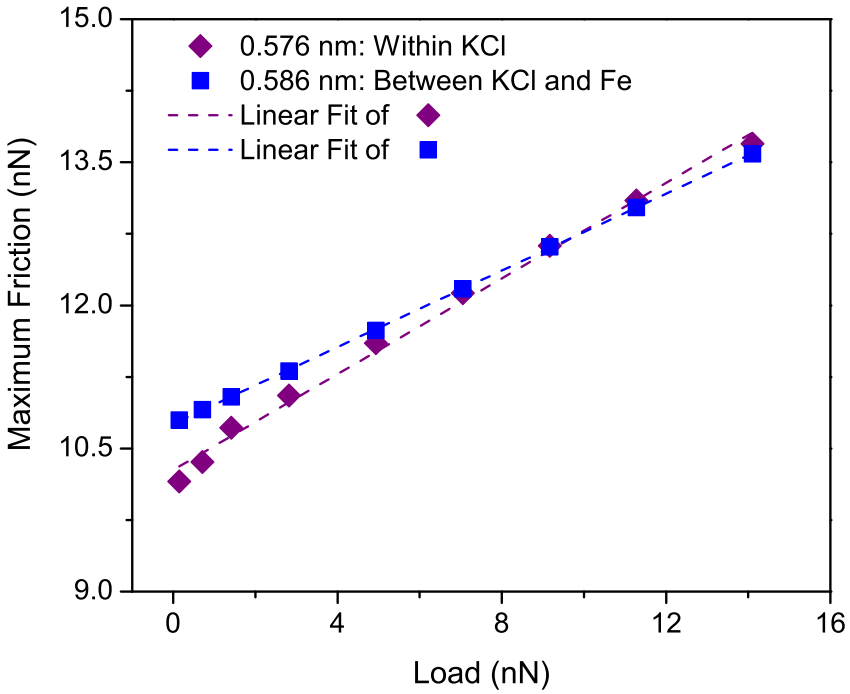

Figure 9.5: Maximum friction as a function of load for models with two different outer KCl lattice constants: 0.576 nm for which sliding always occurs within the KCl film (purple diamonds) and 0.586 nm for which sliding always occurs at the KCl-Fe interface (blue squares). Linear fits of the data to equation 8.1 are shown as dashed lines.

9.3.2 Equilibrium KCl Frictional Load Dependence

The above analyses were carried out for systems in which the lattice constants of the KCl film were constrained to explore their effect on the location of the shear plane. However, under

real conditions, the equilibrium lattice constant of the outer layers of the film is determined by the film thickness and load. To explore the implications of the results from our rigid-layer model, we performed a set of simulations with equilibrium KCl structure, i.e. with all atoms in the KCl film allowed to move relative to one another. The results, shown in figure 9.6, indicate that the outer KCl lattice constant decreases monotonically with load, consistent with the findings in Chapter 8. Sliding occurred at the KCl-Fe interface at all loads. This is consistent with results for the rigid KCl layer model which indicated that shear should occur at the KCl-Fe plane for KCl lattice constants larger than ~0.579 nm, depending on the load (figure 9.3). The maximum rigid KCl lattice constants for which shear occurred within the KCl film at three different loads are shown as dashed lines in figure 9.6. Clearly, in the unconstrained KCl model, the equilibrium lattice constant is much larger than these values, consistent with our observation that shear occurs at the KCl-Fe interface. This also agrees with the experimental results that show no material transfer when sliding on a KCl film, in contrast to sliding on $FeCl_2$, where material transfer does occur [187].

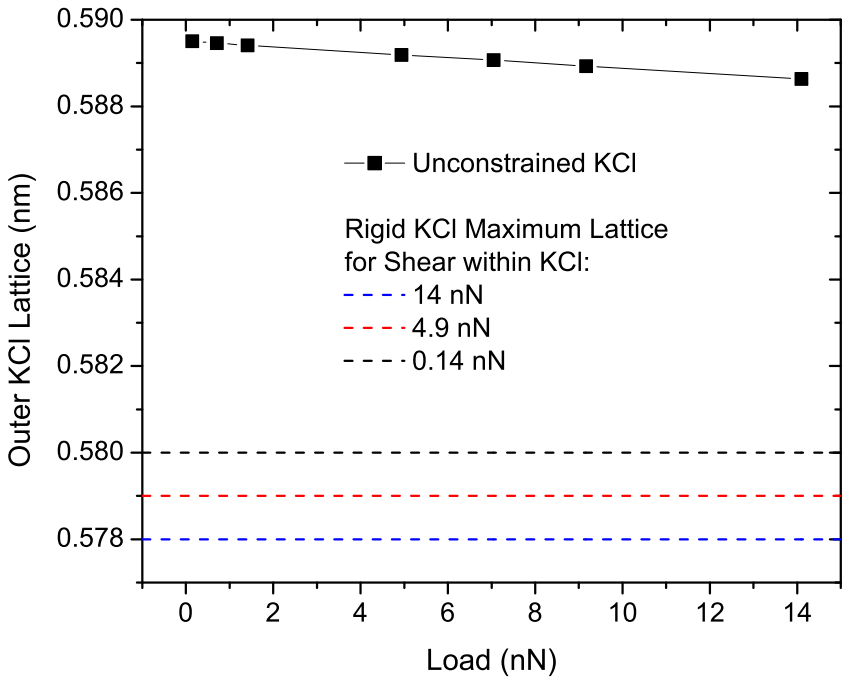

Figure 9.6: Change in the lattice constant of the outer KCl layers (black squares) with increasing load for the unconstrained KCl model. The maximum lattice constants at which shear occurred within the KCl film obtained from the rigid-layer model at three loads are shown as dashed lines.

The maximum friction force for the unconstrained KCl film is shown in figure 9.7. We observe that the friction increases approximately linearly with load, as predicted by equation 8.1. The slope of a linear fit to the simulation results gives a value of α equal to 0.115 ± 0.004, in excellent agreement with the experimental value for a model KCl boundary film measured in UHV of 0.14 ±

0.02 [159], suggesting that the model accurately describes the experiment.

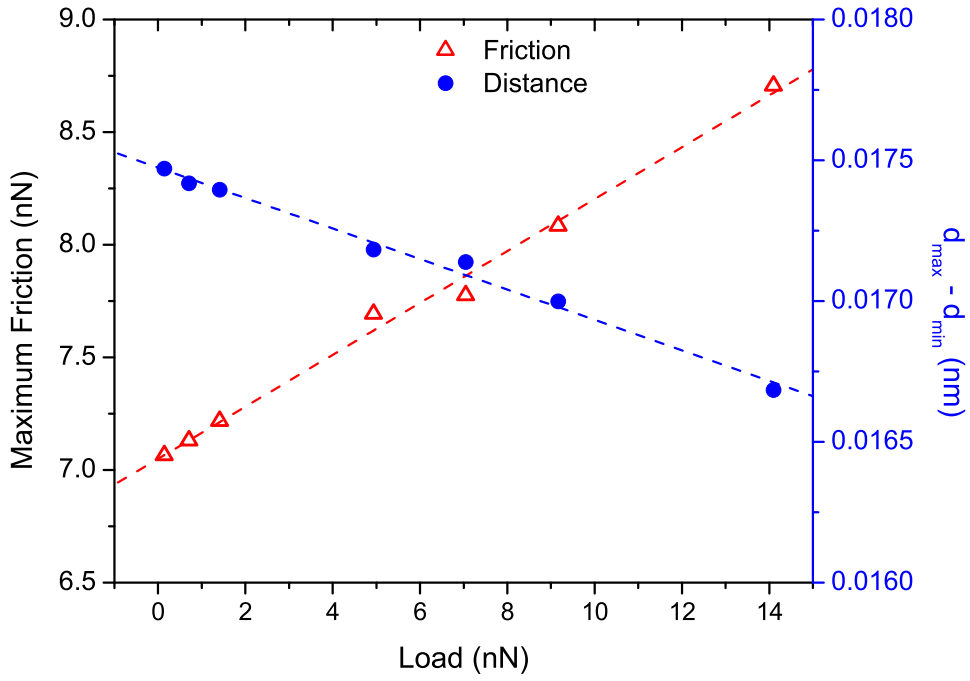

Figure 9.7: Friction increasing with load for sliding at the KCl-Fe interface in simulations with unconstrained KCl (red triangles, left axis). The distance between the maximum (d_{max}) and minimum (d_{min}) vertical position of the Fe during sliding is plotted on the right axis (blue circles). The dashed lines are linear fits to the data.

Since the change in the lattice constant is small as shown in figure 9.6, this is unlikely to be the origin of observed increase of friction with load. Therefore, to understand this trend, we consider a P-T model where there is a periodic potential at the shear plane. The energy of the potential minimum is E^0_{min} at separation d^0_{min} at zero normal force. The corresponding values at the energy maximum of the potential energy corrugation are E^0_{max} at separation d^0_{max}. Under the influence of a normal force, F, the separation will be changed by the external force. Assuming that the curvatures (force constants) of the potentials normal to the surface at the sliding interface are k_{min} and k_{max}, then both the values of E^0_{min} and E^0_{max} will change. Then, $d_{max} = d^0_{max} - \frac{F}{k_{max}}$ and $d_{min} = d^0_{min} - \frac{F}{k_{min}}$. Similarly, $E_{min} = E^0_{min} + \frac{1}{2}k_{min}(d_{min} - d^0_{min})^2$ and $E_{max} = E^0_{max} + \frac{1}{2}k_{max}(d_{max} - d^0_{max})^2$.

The total energy barrier during sliding consists of two components: the intrinsic energy barrier and the external work done on the system. First, we consider the intrinsic energy barrier, ΔE. From above, $d_{max} - d^0_{max} = -\frac{F}{k_{max}}$ and $d_{min} - d^0_{min} = -\frac{F}{k_{min}}$, and writing $\Delta E = E_{max} - E_{min}$ and substituting gives:

$$\Delta E = E^0_{max} - E^0_{min} + \frac{1}{2}(\frac{1}{k_{max}} - \frac{1}{k_{min}})F^2. \tag{9.1}$$

The second contribution is the external work done as the system slides, ΔW, and is given by $\Delta W = F(d_{max} - d_{min})$. Substituting from above gives:

$$\Delta W = F(d^0_{max} - d^0_{min}) + (\frac{1}{k_{min}} - \frac{1}{k_{max}})F^2. \tag{9.2}$$

The total energy change $\Delta E_{tot} = \Delta W + \Delta E$ and is then the sum of equation 9.1 and equation 9.2:

$$\Delta E_{tot} = E^0_{max} - E^0_{min} + F(d^0_{max} - d^0_{min}) + \frac{1}{2}(\frac{1}{k_{min}} - \frac{1}{k_{max}})F^2. \tag{9.3}$$

This gives a S_0 term, a term proportional to F, corresponding to α and a second-order term. From the simulations, we calculate the change in total potential energy of the system during sliding and observed an approximately linear decrease with load (not shown). Therefore, we do not observe the second-order dependence predicted by equation 9.3, either in the total energy or in the friction shown in figure 9.7, presumably because the k values for this system are large. However, variations from linearity are seen in the friction for the constrained sliding of the KCl-KCl interface, while a linear variation is seen for the Fe-KCl interface (figure 9.5). This implies that the repulsive potential between adjacent KCl layers is more compliant than for the Fe-KCl interface.

Next we relate the total energy change to friction force, F_L. This is done by taking F^* in the P-T model for a sinusoidal sliding potential as the relevant force [194–196]. This gives: $F_L = F^* = \frac{\pi \Delta E_{tot}}{a}$, where a is the periodicity. Substituting from above gives a value of α of:

$$\alpha = \frac{\pi(d^0_{max} - d^0_{min})}{a}. \tag{9.4}$$

The difference between the maximum and minimum distance at zero load ($d^0_{max} - d^0_{min}$) can be obtained from the intercept of a linear fit to the load-dependent difference between those distances in the simulations. Figure 9.7 shows $d_{max} - d_{min}$ versus load and a linear fit to the data. The intercept of the fit line is 0.0174 nm and the slope is - 5.4 ± 0.2 × 10^{-5} m/N. Substituting the intercept and equilibrium lattice spacing (a = 0.5895 nm) into equation 9.4 gives α = 0.093. This value is somewhat less than, but of the same order as that obtained from the linear fit of the simulated friction vs. load data to equation 8.1 of 0.115.

This analysis applies to a perfectly sinusoidal potential, while the value of F^* has been found to depend on the shape of the potential, where the influence of potential shape has been modeled using a function of the form $sin^n(\frac{\pi x}{a})$ [197]. A fit to the sliding potential obtained from the simulations of the unconstrained KCl film yields a good fit with n = 3 to 4. The equation for F^* is modified as $F^* = \frac{n\pi\Delta E_{tot}}{a}(\frac{n-1}{n})^{\frac{n}{2}}(\frac{1}{n-1})^{\frac{1}{2}}$, which yields α = 0.107 for n = 3 and 0.121 for n = 4, now in excellent agreement with the simulated value, and experiment [159]. The implication of this finding is that, for a film where the structural change with load is negligible, the pressure-dependent shear strengths can be interpreted within the framework of the P-T model, where S_0 is due to the potential energy corrugation at the sliding interface, while the pressure dependence arises from the external work done on the system as the interlayer spacing changes during sliding. Quadratic terms are, in

principle, possible but are not seen for the unconstrained film since the compressive stiffness of the KCl-Fe interface is high. However, deviations in linearity are seen for the sliding of the constrained film where shear occurs at the KCl-KCl interface.

9.4 Conclusions

The origin of the commonly observed variation in shear strength with pressure that has been found experimentally for boundary films is explored using a model system consisting of KCl on iron. The simulation parameters to describe interactions between the iron and KCl were previously calibrated using experiments carried out in UHV to ensure the validity of the model. It is found that the structure of the film is influenced by the normal load and, in particular, can change the location of the shear plane, whether it occurs within the film or between the film and substrate, depending on the KCl lattice spacing. Simulations with rigid KCl layers, where the lattice constant could be varied independently of the load, revealed that increasing load can affect both the registry of the film and the interlayer spacing, and that both of these factors can affect friction leading to both an increase or a decrease in friction force with outer KCl lattice depending on the location of the shear plane. Carrying out the MD simulation of sliding for the equilibrium KCl structure shows that the shear strength depends approximately linearly on contact pressure with a calculated slope of 0.115 ± 0.004, in good agreement with the experimental value of 0.14 ± 0.02. For this case, shear is found to occur at the Fe-KCl interface at any load, so that no transfer of KCl is expected, as found experimentally. However, the rigid KCl layer results suggest that this is not universally the case and that the location of the shear plane could occur within the film in cases where the lattice constant of the outermost layer of the film is closer to that of the adjacent substrate. The pressure-dependent shear strength is interpreted using the P-T model where it is found that the constant term S_0 arises from the potential corrugation at the sliding interface, while the pressure-dependent term α originates from the external work carried out on the system due to the change in interlayer spacing at the sliding interface. While the results were obtained for a simple model system consisting of KCl on iron, it is anticipated that the general conclusions will apply equally well to more realistic boundary films.

Chapter 10

Recommendations for Future Research

In this chapter, to further explore the tribological properties of $AgTaO_3$ and its alternatives as high-temperature solid lubricants, we propose several research activities that could be performed in the future. Specifically, this research includes: (a) predicting the mechanical properties of $AgTaO_3$, (b) studying the velocity dependence of tribological behavior, and (c) exploring self-healing mechanisms of a Ta_2O_5+Ag/Ag_2O tribofilm. Each topic will be discussed in one of the following sections.

10.1 Modeling Mechanical Properties

Until recently, studies on the material properties of $AgTaO_3$ have been very limited. Mechanical properties of $AgTaO_3$, such as elastic modulus, shear modulus and hardness, are important but have not been explored systematically. These properties are important since they are closely related to the tribological performance of solid lubricant materials. In addition, quantitative characterization of those properties could be helpful in understanding the effects of, for instance, film composition and working environment on friction and wear. The research proposed in this section is discussed from a modeling perspective, in which the responses of material to external forces can be modeled via (i) nano-indentation and (ii) tensile strain simulations. These approaches have been extensively used on characterizing material properties for solids [198,199]. As a result, elastic modulus, hardness and yield/tensile/compressive strength for $AgTaO_3$ tribofilm can be obtained. Those material properties can be characterized before and after sliding as well as at different temperatures to identify the effects of film evolution and working environments.

The indentation simulation on an ideal crystal structure can be described as a hemispherical indenter moving towards and then away from a substrate material with a constant speed (see figure 10.1). The interaction strength between the substrate and the indenter is determined by a force constant K. Therefore, the normal force can be obtained by $F(r) = -K(r - R)^2$, where r is the distance from an atom in the substrate to the center of the indenter, and R is the radius of the indenter. By using the method presented by Oliver and Pharr [200], the force-distance curve can be fit to

$$F = a(d - d_f)^{3/2}, \tag{10.1}$$

where a and d_f are fitting parameters. To avoid the effect of plastic deformation on the calculation of material properties, a small indent depth is recommended ($\leq$10 % of the film thickness). Also,

the unloading curve should be used in those calculations for the same reason. A reduced modulus (E_r) and hardness (H) of a tribofilm can therefore be calculated via expressions of $E_r = \frac{S}{2}\sqrt{\frac{\pi}{A}}$ and $H = \frac{F_0}{A}$, respectively, where S is the contact stiffness, A is the projected contact area and F_0 is the maximum force. In the same fashion, E_r and H of a restructured film or a film with varied compositions can be obtained.

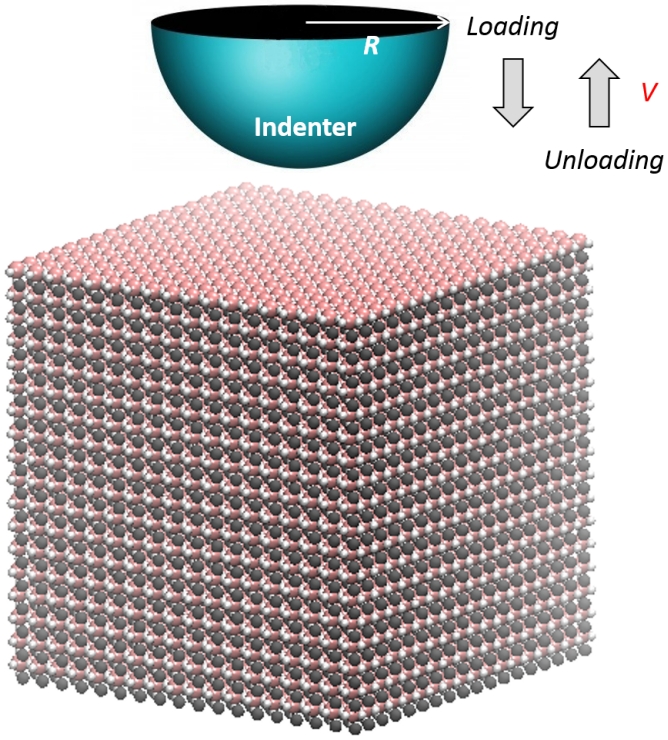

Figure 10.1: A snapshot of a possible configuration for the proposed indentation simulation. (Ag – grey, Ta – pink, and O – white)

Figure 10.2 shows a model system that can be potentially used to study effects of tension and compression on material properties. Atoms in the top and bottom layers are held rigid throughout the simulation, while atoms between the two layers are free to move. After equilibration of the system, external forces are applied on both of the rigid layers. Under those forces, the top layer will be moved gradually toward or away from the bottom layer in order to compress or stretch the structure. The uniaxial stress is then given as $\sigma = \frac{Nk_BT}{V} + \frac{\sum_i^N r_i \cdot f_i}{dV}$, where N is the number of atoms in the system, k_B is the Boltzmann constant, T is temperature, d is the dimensionality of the system, V is system volume, r is distance and f is interaction force. The strain rate (ε) is determined by calculating the average axial length, given $\varepsilon(t)_z = \frac{L_z(t) - L_z(0)}{L_z(t)}$, where $L_z(0)$ is the initial length of the model material and $L_z(t)$ is the mean length in the z direction. Then, the yield strength and

compressive/tensile strength can be obtained from the stress-strain curve. Specifically, the yield strength is the maximum stress before plastic deformation, and the compressive/tensile strength is the maximum stress before the material fails completely. The elastic modulus will be calculated as the slope of stress-strain curve, which can be compared with those calculated from the indentation simulations. Figure 10.3 shows a representative stress-strain relationship based on the model system shown in figure 10.2, from which the elastic modulus and yield strength of $AgTaO_3$ can be obtained.

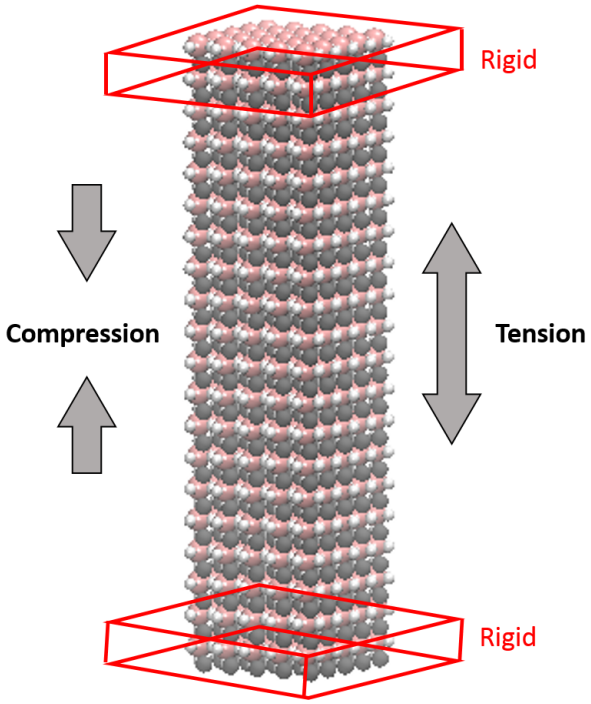

Figure 10.2: Snapshot of the proposed tension and compression simulation. The bottom layer is fixed, and top layer is rigid. (Atom colors are the same as those in figure 10.1)

To sum up, two model systems (i.e. nano-indentation and tensile strain) are proposed to use in the calculation of material and mechanical properties (elastic modulus, hardness, yield / tensile / compressive strength) of $AgTaO_3$ tribofilm. These properties are expected to be explored in terms of working environments, material evolution and film composition in order to fully characterize $AgTaO_3$. This study can be also applied on other materials such as Cu-Ta-O, which is valuable in the understanding of the lubricating mechanisms of solid lubricants for high temperature applications.

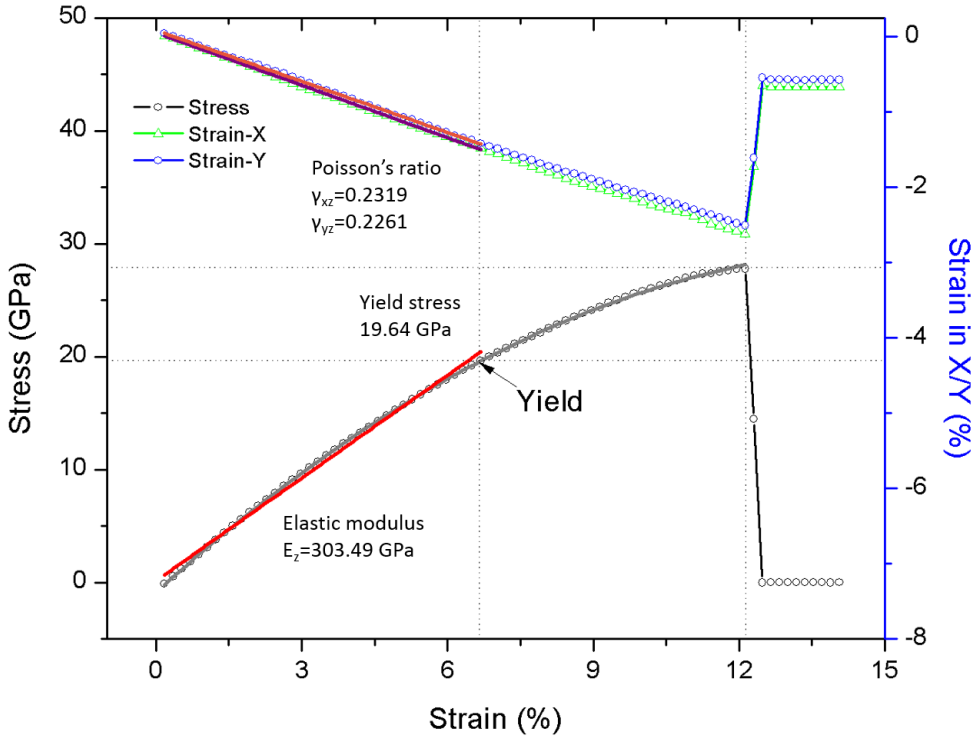

Figure 10.3: An example of stress-strain relationship from the model shown in figure 10.2.

10.2 Velocity Dependence of Solid Lubricant Friction

Velocity plays an important role in sliding contact problems [61, 201, 202]. Velocity dependence of friction has been reported on a variety of materials. In most cases, friction increases with velocity [196, 202–204] because the sliding time is insufficient for thermal activation occurring between tip and substrate at high speed. However, opposite trends have been also observed at some temperatures [205]. So far, the effect of sliding speed on the tribological behavior of $AgTaO_3$ still remains unclear. Given the importance of exploring this effect on the tribological performance of $AgTaO_3$ at elevated temperatures, we propose to use MD simulations and theoretical models to obtain details of frictional behavior of atoms in the interfacial contact during sliding process.

The MD model can be similar to the model system described in Chapter 5: a model tip apex slid against a $AgTaO_3$ tribofilm. The bottom layer of the tribofilm is fixed, and the tip apex slides at a constant speed. The sliding speed could be varied in a range from 0.1 to 100 m/s, and multiple temperatures could be applied. In each case, friction can be obtained by averaging the friction forces during the steady state. The shear stress distribution at the interfacial region can be also captured throughout the sliding process.

Contact between two surfaces could be formed at atomic level, referring to as single asperity contact. This contact mode has been recognized in many tribological systems and is applicable in the present work to describe the interactive behavior between tip apex and substrate. During sliding, dynamic behavior between the two contacting objects can be mathematically described in the framework of a simple yet robust model, the Prandtl-Tomlinson (PT) model [163, 164], which has been successfully used to address velocity dependence of friction originated from single asperity contact. The PT model simplifies the atomic force microscope tip-substrate system into a spring-mass system, whose total energy can be formulated as,

$$V(x, S) = U(x) + \frac{1}{2}k(S - x)^2. \tag{10.2}$$

The first term $U(x)$ on the right-hand side of this expression describes the corrugation potential. In most cases, it is assumed to have a sinusoidal form, $U(x) = -\frac{U_0}{2}cos(\frac{2\pi x}{a})$, where U_0 is the amplitude, x is the tip position, and a is the lattice spacing of the substrate. The second term in equation 10.2 is the elastic potential resulting from the interaction between the tip and support, where k is the spring stiffness (or physically speaking the combined stiffness of the cantilever and tip) and S is the position of a support moving at a constant velocity. Therefore, lateral force can be expressed as a function of the velocity of the tip apex (v).

The sliding process of single asperity contact can be further quantified using harmonic transition state theory (HTST), which is primarily used to quantify the reaction rates of elementary chemical reactions. Within HTST, the probability p that the tip resides in the initial local minimum (in the absence of back slips) can be obtained by solving:

$$\frac{dp}{dt} = -f_0 exp(\frac{-\Delta V}{k_B T})p, \tag{10.3}$$

where f_0 is the attempt frequency, ΔV is the energy barrier, k_B is the Boltzmann constant and T is the temperature. Both the energy barrier and attempt frequency are functions of friction force F, which can be further expressed as a function of velocity v. By substituting $\Delta V(F)$ and $f_0(F)$ into equation 10.3, the velocity dependence of friction can be obtained. This theoretical approach, involving both PT model and HTST, can be an ideal framework to characterize atomic single asperity contact sliding behavior. Complementing the MD study, this approach can be beneficial in the understanding of sliding mechanisms of $AgTaO_3$ tribofilm.

10.3 Self-Healing Behavior of a Ta_2O_5+Ag/Ag_2O Tribofilm

Material failure due to crack propagation and fracture is commonly observed in engineering practice. As one potential solution, certain ceramic oxides have been reported recently that exhibited the ability to restore and retain their intrinsic mechanical properties via repairing their inherent flaws and cracks, namely self-healing [206]. Given the observation of restructuring of the Ta_2O_5+Ag/$AgTaO_3$ tribofilm and Ag cluster migration during high-temperature sliding [130], self-healing mechanisms could be applicable to explain behavior of this type of materials. Therefore, in this section, the proposed research aims to explore and understand self-healing mechanisms in a model binary oxide / silver (or silver oxide) system using atomistic modeling.

The simulation model could be designed as a tribofilm with a notch/crack on its edge or in the center (figure 10.4 shows a representative tribofilm with a notch on its edge). In a high-temperature environment, pressure from different directions could be applied on the film surface to mimic external forces. Tribofilm with various of compositions (Ta_2O_5, Ag and Ag_2O) should be investigated. Self-healing behavior is expected to be largely attributed to the high-temperature induced enhanced Ag diffusion to the crack. Therefore, quantification of the evolution of Ag clusters should be a key, and this can be accomplished by following the method discussed in the previous sections. In addition, the effects of dislocation activity and grain boundary sliding should be examined since they may contribute to the tribofilm deformation. Eventually, mechanical and tribological properties of the healed material should be compared with those from tribofilms with defects.

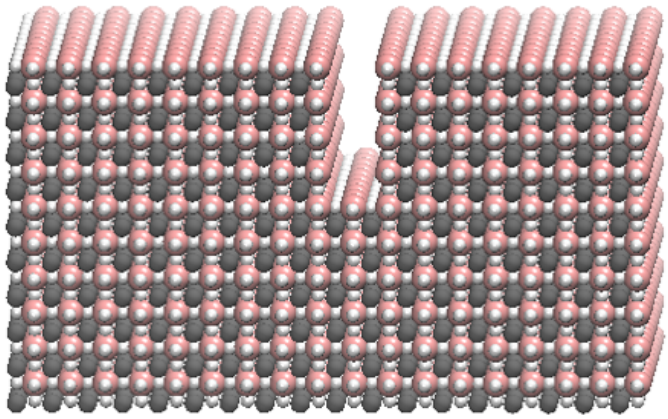

Figure 10.4: A snapshot of a tribofilm with an edge notch. (Atom colors are the same as those in figure 10.1)

10.4 Summary

In this work, we focused on investigating the tribological properties of solid lubricant materials, in which molecular dynamics simulation was used as the primary research tool. The lubricating mechanisms of high-temperature solid lubricant candidates, ternary oxides Ag/Cu-Ta-O, have been extensively explored in terms of intrinsic (surface termination and composition) and extrinsic (normal load and temperature) influences. All the MD simulations were performed based on newly developed interatomic potential parameters in the formalism of the modified embedded-atom method. To investigate lubricating solids in general, a model boundary lubricating system—potassium chloride and iron—was studied in a non-extreme environment, where both computational and theoretical models were applied. In this last chapter, potential research activities were proposed to complement

the studies carried out in this research. Specifically, the future work includes exploring the mechanical properties of $AgTaO_3$, studying the velocity dependence of friction, and quantifying self-healing behavior. We hope the accomplished and proposed research can provide insight into the lubricious nature of solid lubricant materials and benefit the development as well as design of novel lubricant materials in the future.

Bibliography

[1] G. E. Kugel, M. D. Fontana, M. Hafid, K. Roleder, A. Kania, and M. Pawelczyk. A Raman study of silver tantalate ($AgTaO_3$) and its structural phase transition sequence. *Journal of Physics C: Solid State Physics*, 20:1217–1230, 1987.

[2] H. Gao, A. Otero-de-la Roza, S. M. Aouadi, A. Martini, and E. R. Johnson. Chemical basis of the tribological properties of $AgTaO_3$ crystal surfaces. *Journal of Physical Chemistry C*, 118:17577–17584, 2014.

[3] M. I. Baskes. Modified embedded-atom potentials for cubic materials and impurities. *Physical Review B*, 46:2727–2742, 1992.

[4] R. W. G. Wyckoff. *Crystal Structures*. Wiley, New York, 1963.

[5] C. Muratore and A. A. Voevodin. Chameleon coatings: adaptive surfaces to reduce friction and wear in extreme environments. *Annual Review of Materials Research*, 39:297–324, 2009.

[6] M. R. Hilton and P. D. Fleischauer. Applications of solid lubricant films in spacecraft. *Surface and Coatings Technology*, 54-55, Part 2:435–441, 1992.

[7] M. J. Todd. Solid lubrication of ball bearings for spacecraft mechanisms. *Tribology International*, 15:331–337, 1982.

[8] H. E. Sliney. Solid lubricant materials for high temperaturesa review. *Tribology International*, 15(5):303–315, 1982.

[9] I. M. Allam. Solid lubricants for applications at elevated temperatures. *Journal of Materials Science*, 26:3977–3984, 1991.

[10] P. J. John and J. S. Zabinski. Sulfate based coatings for use as high temperature lubricants. *Tribology Letters*, 7:31–37, 1999.

[11] D. S. Stone, J. Migas, A. Martini, T. Smith, C. Muratore, A. A. Voevodin, and S. M. Aouadi. Adaptive NbN/Ag coatings for high temperature tribological applications. *Surface and Coatings Technology*, 206:4316–4321, 2012.

[12] S. Gupta, D. Filimonov, T. Palanisamy, T. El-Raghy, and M. W. Barsoum. Ta_2AlC and Cr_2AlC Ag-based composites–New solid lubricant materials for use over a wide temperature range against Ni-based superalloys and alumina. *Wear*, 262:1479–1489, 2007.

[13] C. Donnet and A. Erdemir. Solid lubricant coatings: Recent developments and future trends. *Tribology Letters*, 17:389–397, 2004.

[14] A. A. Voevodin and J. S. Zabinski. Nanocomposite and nanostructured tribological materials for space applications. *Composites Science and Technology*, 65:741–748, 2005.

[15] T. W. Scharf and S. V. Prasad. Solid lubricants: a review. *Journal of Materials Science*, 48:511–531, 2013.

[16] S. M. Aouadi, B. Luster, P. Kohli, C. Muratore, and A. A. Voevodin. Progress in the development of adaptive nitride-based coatings for high temperature tribological applications. *Surface and Coatings Technology*, 204:962–968, 2009.

[17] A. A Voevodin and J. S Zabinski. Supertough wear-resistant coatings with 'chameleon' surface adaptation. *Thin Solid Films*, 370:223–231, 2000.

[18] H. E. Sliney. Wide temperature spectrum self-lubricating coatings prepared by plasma spraying. *Thin Solid Films*, 64:211–217, 1979.

[19] A. Erdemir. *Modern Tribology Handbook, Vol. II*. CRC Press, Boca Raton, 2001.

[20] W. O. Winer. Molybdenum disulfide as a lubricant: A review of the fundamental knowledge. *Wear*, 10:422–452, 1967.

[21] J. P. G. Farr. Molybdenum disulphide in lubrication. A review. *Wear*, 35:1–22, 1975.

[22] S. V. Prasad, J. S. Zabinski, and N. T. McDevitt. Friction behavior of pulsed laser deposited tungsten disulfide films. *Tribology Transactions*, 38:57–62, 1995.

[23] P. J. Bryant, P. L. Gutshall, and L. H. Taylor. A study of mechanisms of graphite friction and wear. *Wear*, 7:118–126, 1964.

[24] R. H. Savage. Graphite lubrication. *Journal of Applied Physics*, 19:1–10, 1948.

[25] A. Wells and D. J. De Wet. The use of platinum in thin tribological coatings. *Wear*, 127:269–281, 1988.

[26] T. Spalvins and H. E. Sliney. Frictional behavior and adhesion of ag and au films applied to aluminum oxide by oxygen-ion assisted screen cage ion plating (scip). *NASA TM-106522*, 1994.

[27] O. O. Ajayi, A. Erdemir, J.-H. Hsieh, R. A. Erck, G. R. Fenske, and F. A. Nichols. Boundary film for structural ceramic materials. *Wear*, 162-164, Part B:1150–1155, 1993.

[28] A. Erdemir, O. O. Ajayi, G. R. Fenske, R. A. Erck, and J. H. Hsieh. The synergistic effects of solid and liquid lubrication on the tribological behavior of transformation-toughened ZrO_2 ceramics. *Tribology Transactions*, 35:287–297, 1992.

[29] C. Donnet and A. Erdemir. Historical developments and new trends in tribological and solid lubricant coatings. *Surface and Coatings Technology*, 180-181:76–84, 2004.

[30] J. R. Lince and P. D. Fleischauer. Solid lubrication for spacecraft mechanisms. *AEROSPACE REPORT*, No. TR-97(8565)-4:217105, 1997.

[31] H. E. Sliney. Rare earth fluorides and oxides–an exploratory study of their use as solid lubricants at temperatures to 1800 °F (1000 °C). *NASA TN D-5301*, 1969.

[32] A. Erdemir. A crystal chemical approach to the formulation of self-lubricating nanocomposite coatings. *Surface and Coatings Technology*, 200:1792–1796, 2005.

[33] A Erdemir. A crystal-chemical approach to lubrication by solid oxides. *Tribology Letters*, 8:97–102, 2000.

[34] W. Gulbinski and T. Suszko. Thin films of Mo_2N/Ag nanocomposite-the structure, mechanical and tribological properties. *Surface and Coatings Technology*, 201:1469–1476, 2006.

[35] S. M. Aouadi, Y. Paudel, B. Luster, S. Stadler, P. Kohli, C. Muratore, C. Hager, and A. A. Voevodin. Adaptive Mo_2N/MoS_2/Ag tribological nanocomposite coatings for aerospace applications. *Tribology Letters*, 29:95–103, 2008.

[36] D. Stone, J. Liu, D. P. Singh, C. Muratore, A. A. Voevodin, S. Mishra, C. Rebholz, Q. Ge, and S. M. Aouadi. Layered atomic structures of double oxides for low shear strength at high temperatures. *Scripta Materialia*, 62:735–738, 2010.

[37] V. Ageh, H. Mohseni, and T. W. Scharf. Lubricious zinc titanate coatings for high temperature applications. *Surface and Coatings Technology*, 237:241–247, 2013.

[38] H. Mohseni and T. W. Scharf. Atomic layer deposition of $ZnO/Al_2O_3/ZrO_2$ nanolaminates for improved thermal and wear resistance in carbon-carbon composites. *Journal of Vacuum Science & Technology A*, 30:01A149, 2012.

[39] M. B. Peterson, S. Z. Li, and S. F. Murray. Wear-resisting oxide films for 900 °C. Final report. *ANL/OTM/CR-5*, 1994.

[40] V. Brazdova, M. V. Ganduglia-Pirovano, and J. Sauer. Periodic density functional study on structural and vibrational properties of vanadium oxide aggregates. *Physical Review B*, 69:165420, 2004.

[41] G. Kresse, S. Surnev, M. G. Ramsey, and F. P. Netzer. First-principles calculations for V_xO_y grown on Pd(111). *Surface Science*, 492:329–344, 2001.

[42] M. V. Ganduglia-Pirovano and J. Sauer. Stability of reduced V_2O_5(111) surfaces. *Physical Review B*, 70:045422, 2004.

[43] N. A. Deskins, S. Kerisit, K. M. Rosso, and M. Dupuis. Molecular dynamics characterization of rutile-anatase interfaces. *The Journal of Physical Chemistry C*, 111:9290–9298, 2007.

[44] D. G. Schlom, L. Chen, X. Pan, A. Schmehl, and M. A. Zurbuchen. A thin film approach to engineering functionality into oxides. *Journal of the American Ceramic Society*, 91:2429–2454, 2008.

[45] C. Muratore and A. A. Voevodin. Molybdenum disulfide as a lubricant and catalyst in adaptive nanocomposite coatings. *Surface and Coatings Technology*, 201:4125–4130, 2006.

[46] S. M. Aouadi, Y. Paudel, W. J. Simonson, Q. Ge, P. Kohli, C. Muratore, and A. A. Voevodin. Tribological investigation of adaptive $Mo_2N/MoS_2/Ag$ coatings with high sulfur content. *Surface and Coatings Technology*, 203:1304–1309, 2009.

[47] S. Y. Li, J. A. Rodriguez, J. Hrbek, H. H. Huang, and G.-Q. Xu. Chemical and electronic properties of silver atoms supported on sulfur and molybdenum sulfide surfaces. *Surface Science*, 395:216–228, 1998.

[48] D. S. Stone, S. Harbin, H. Mohseni, J.-E. Mogonye, T. W. Scharf, C. Muratore, A. A. Voevodin, A. Martini, and S. M. Aouadi. Lubricious silver tantalate films for extreme temperature applications. *Surface and Coatings Technology*, 217:140–146, 2013.

[49] M. Valant, A. Axelsson, and N. Alford. Review of Ag(Nb, Ta)O_3 as a functional material. *Journal of the European Ceramic Society*, 27:2549–2560, 2007.

[50] H. P. Soon, H. Taniguchi, and M. Itoh. Dielectric and soft-mode behaviors of $AgTaO_3$. *Physical Review B*, 81:104105, 2010.

[51] M. H. Francombe and B. Lewis. Structural and electrical properties of silver niobate and silver tantalate. *Acta Crystallographica*, 11:175–178, 1958.

[52] M. Pawelczyk. Phase transitions in $AgTa_xNb_{1-x}O_3$ solid solutions. *Phase Transitions*, 8:273–292, 1987.

[53] Y. Wang, Q. Liu, and F. Zhao. Phase transition behavior and electrical properties of $[(K_{0.50}Na_{0.50})_{1-x}Ag_x](Nb_{1-x}Ta_x)O_3$ lead-free ceramics. *Journal of Alloys and Compounds*, 489:175–178, 2010.

[54] Y. Han, I. M. Reaney, R. L. Johnson-Wilke, M. B. Telli, D. S. Tinberg, I. Levin, D. D. Fong, T. T. Fister, S. K. Streiffer, and S. Trolier-McKinstry. Structural phase transitions in $AgTa_{0.5}Nb_{0.5}O_3$ thin films. *Journal of Applied Physics*, 107:123517, 2010.

[55] J. Suchanicz and A. Kania. Uniaxial pressure effect on dielectric properties of $AgTaO_3$ single crystals. *Ferroelectrics*, 393:21–26, 2009.

[56] J. F. Molinari, M. Ortiz, R. Radovitzky, and E. A. Repetto. Finite-element modeling of dry sliding wear in metals. *Engineering Computations*, 18:592–610, 2001.

[57] M. Amiri and M. M. Khonsari. On the thermodynamics of friction and wear–a review. *Entropy*, 12:1021, 2010.

[58] H. C. Meng and K. C. Ludema. Wear models and predictive equations: their form and content. *Wear*, 181183, Part 2:443–457, 1995.

[59] B. Bhushan. *Nanotribology and Nanomechanics I: Measurement Techniques and Nanomechanics*. Nanotribology and Nanomechanics. Springer, Berlin-Heidelberg, 2011.

[60] M. P. Allen and D. J. Tildesley. *Computer simulation of liquids*. Oxford University Press, New York, 1987.

[61] Y. Dong, Q. Li, and A. Martini. Molecular dynamics simulation of atomic friction: A review and guide. *Journal of Vacuum Science and Technology A*, 31:030801, 2013.

[62] A. Laio and M. Parrinello. Escaping free-energy minima. *Proceedings of the National Academy of Sciences*, 99:12562–12566, 2002.

[63] R. Martoňák, A. Laio, and M. Parrinello. Predicting crystal structures: The Parrinello-Rahman method revisited. *Physical Review Letters*, 90:075503, 2003.

[64] C. W. Yong, W. Smith, and K. Kendall. Surface contact studies of NaCl and TiO_2: molecular dynamics simulation studies. *Journal of Materials Chemistry*, 12:2807–2815, 2002.

[65] I. Gheewala, R. Smith, and S. D. Kenny. Nanoindentation and nanoscratching of rutile and anatase TiO_2 studied using molecular dynamics simulations. *Journal of Physics: Condensed Matter*, 20:354010, 2008.

[66] D. J. Mann and W. L. Hase. Computer simulation of sliding hydroxylated alumina surfaces. *Tribology Letters*, 7:153–159, 1999.

[67] O. A. Mazyar, H. Xie, and W. L. Hase. Nonequilibrium energy dissipation at the interface of sliding model hydroxylated α-alumina surfaces. *The Journal of Chemical Physics*, 122:094713, 2005.

[68] Q. Zhang, Y. Qi, L. G. Hector, T. Cagin, and W. A. Goddard. Atomic simulations of kinetic friction and its velocity dependence at Al/Al and α-Al_2O_3/α-Al_2O_3 interfaces. *Physical Review B*, 72:045406, 2005.

[69] D. Wei and Y. Zhang. Friction between α-Al_2O_3(0001) surfaces and the effects of surface hydroxylation. *Surface Science*, 603:L95–L98, 2009.

[70] Q. Zhang, Y. Qi, L. G. Hector, T. Cagin, and W. A. Goddard. Origin of static friction and its relationship to adhesion at the atomic scale. *Physical Review B*, 75:144114, 2007.

[71] D. J. Mann, L. Zhong, and W. L. Hase. Effect of surface stiffness on the friction of sliding model hydroxylated α-alumina surfaces. *The Journal of Physical Chemistry B*, 105:12032–12045, 2001.

[72] C. W. Yong, W. Smith, and K. Kendall. Molecular dynamics simulations of (001) MgO surface contacts: effects of tip structures and surface matching. *Nanotechnology*, 14:829, 2003.

[73] T. Trevethan and L. Kantorovich. Atomistic simulations of the adhesion hysteresis mechanism of atomic scale dissipation in non-contact atomic force microscopy. *Nanotechnology*, 15:S34–S39, 2004.

[74] T. Trevethan and L. Kantorovich. Stochastic mechanism of energy dissipation in noncontact atomic force microscopy studied using molecular dynamics with langevin boundary conditions. *Physical Review B*, 70:115411, 2004.

[75] Z. Hu and C. H. Turner. Initial surface reactions of TiO_2 atomic layer deposition onto SiO_2 surfaces: Density functional theory calculations. *The Journal of Physical Chemistry B*, 110:8337–8347, 2006.

[76] M. Chandross, E. B. Webb, M. J. Stevens, G. S. Grest, and S. H. Garofalini. Systematic study of the effect of disorder on nanotribology of self-assembled monolayers. *Physical Review Letters*, 93:166103, 2004.

[77] C. D. Lorenz, E. B. Webb, M. J. Stevens, M. Chandross, and G. S. Grest. Frictional dynamics of perfluorinated self-assembled monolayers on amorphous SiO_2. *Tribology Letters*, 19:93–98, 2005.

[78] O. A. Mazyar, G. K. Jennings, and C. McCabe. Frictional dynamics of alkylsilane monolayers on SiO_2: Effect of 1-n-butyl-3-methylimidazolium nitrate as a lubricant. *Langmuir*, 25:5103–5110, 2009.

[79] K. Chenoweth, A. C. T. van Duin, P. Persson, M.-J. Cheng, J. Oxgaard, and W. A. Goddard. Development and application of a reaxff reactive force field for oxidative dehydrogenation on vanadium oxide catalysts. *The Journal of Physical Chemistry C*, 112:14645–14654, 2008.

[80] Q. Zhang, T. Cagin, A. C. T. van Duin, W. A. Goddard, Y. Qi, and L. G. Hector. Adhesion and nonwetting-wetting transition in the Al/α-Al_2O_3 interface. *Physical Review B*, 69:045423, 2004.

[81] A. C. T. van Duin, A. Strachan, S. Stewman, Q. Zhang, X. Xu, and W. A. Goddard. ReaxFF SiO reactive force field for silicon and silicon oxide systems. *The Journal of Physical Chemistry A*, 107:3803–3811, 2003.

[82] H. Kato, H. Kobayashi, and A. Kudo. Role of Ag^+ in the band structures and photocatalytic properties of $AgMO_3$ (M: Ta and Nb) with the perovskite structure. *Journal of Physical Chemistry B*, 106:12441–12447, 2002.

[83] S. Cabuk and S. Simsek. First-principles studies of the electronic structure and optical properties of $AgBO_3$ (B=Nb,Ta) in the paraelectric phase. *Central European Journal of Physics*, 6:730–736, 2008.

[84] T. Katsumata, Y. Inaguma, M. Itoh, and K. Kawamura. Influence of covalent character on high Li ion conductivity in a perovskite-type Li ion conductor: Prediction from a molecular dynamics simulation of $La_{0.6}Li_{0.2}TiO_3$. *Chemistry of Materials*, 14:3930–3936, 2002.

[85] M. Sepliarsky, A. Asthagiri, S. R. Phillpot, M. G. Stachiotti, and R. L. Migoni. Atomic-level simulation of ferroelectricity in oxide materials. *Current Opinion in Solid State and Materials Science*, 9:107–113, 2005.

[86] T. Shimada, K. Wakahara, Y. Umeno, and T. Kitamura. Shell model potential for $PbTiO_3$ and its applicability to surfaces and domain walls. *Journal of Physics: Condensed Matter*, 20:325225, 2008.

[87] Y. Z. Wang, E. Bevillon, A. Chesnaud, G. Geneste, and G. Dezanneau. Atomistic simulation of pure and doped $BaSnO_3$. *The Journal of Physical Chemistry C*, 113:20486–20492, 2009.

[88] X. Q. Hu, G. F. Xie, and Y. Ma. A new optimization method for shell model interatomic potential parameters of perovskite ferroelectrics. *Physica B: Condensed Matter*, 405:2577–2580, 2010.

[89] C. L. Kuo and P. Clancy. Development of atomistic MEAM potentials for the silicon-oxygen-gold ternary system. *Modelling and Simulation in Materials Science and Engineering*, 13:1309, 2005.

[90] M. I. Baskes. Modified embedded atom method calculations of interfaces. *Report number: SAND-96-8484C*.

[91] B.-J. Lee, W.-S. Ko, H.-K. Kim, and E.-H. Kim. The modified embedded-atom method interatomic potentials and recent progress in atomistic simulations. *Calphad*, 34:510–522, 2010.

[92] S. M. Valone, M. I. Baskes, and R. L. Martin. Atomistic model of helium bubbles in gallium-stabilized plutonium alloys. *Physical Review B*, 73:214209, 2006.

[93] T. Ohira, Y. Inoue, K. Murata, and J. Murayama. Magnetite scale cluster adhesion on metal oxides surfaces: atomistic simulation study. *Applied Surface Science*, 171:175–188, 2001.

[94] H. K. Kim, W. S. Jung, and B. J. Lee. Modified embedded-atom method interatomic potentials for the Fe-Ti-C and Fe-Ti-N ternary systems. *Acta Materialia*, 57:3140–3147, 2009.

[95] K. H. Kang, I. Sa, J. C. Lee, E. Fleury, and B. J. Lee. Atomistic modeling of the Cu-Zr-Ag bulk metallic glass system. *Scripta Materialia*, 61:801–804, 2009.

[96] E. C. Do, Y.-H. Shin, and B.-J. Lee. Atomistic modeling of III-V nitrides: modified embedded-atom method interatomic potentials for GaN, InN and $Ga_{1-x}In_xN$. *Journal of Physics: Condensed Matter*, 21:325801, 2009.

[97] W.-S. Jung H.-K. Kim and B.-J. Lee. Modified embedded-atom method interatomic potentials for the Nb-C, Nb-N, Fe-Nb-C, and Fe-Nb-N system. *Journal of Materials Research*, 25:1288–1297, 2010.

[98] B. Jelinek, S. Groh, A. Moitra, M. F. Horstemeyer, J. Houze, S. G. Kim, G. J. Wagner, and M. I. Baskes. MEAM potential for Al, Si, Mg, Cu and Fe alloys. *Physical Review B*, 85:245102, 2012.

[99] S. Plimpton. Fast parallel algorithms for short-range molecular dynamics. *Journal of Computational Physics*, 117:1–19, 1995.

[100] K. P. Huber and G. Herzberg. *Molecular Spectra and Molecular Structure: IV. Constants of Diatomic Molecules*. Van Nostrand Reinhold company, New York, 1979.

[101] M. R. Baren. The Ag-Ta (silver-tantalum) system. *Journal of Phase Equilibria*, 9:244–245, 1988.

[102] H. E. Sliney. The use of silver in self-lubricating coatings for extreme temperatures. *ASLE Transactions*, 29:370–376, 1986.

[103] J. J. Hu, C. Muratore, and A. A. Voevodin. Silver diffusion and high-temperature lubrication mechanisms of YSZ-Ag-Mo based nanocomposite coatings. *Composites Science and Technology*, 67:336–347, 2007.

[104] J.-H. Wu, S. Karthikeyan, M. L. Falk, and D. A. Rigney. Tribological characteristics of diamond-like carbon (DLC) based nanocomposite coatings. *Wear*, 259:744–751, 2005.

[105] T. W. Scharf, P. G. Kotula, and S. V. Prasad. Friction and wear mechanisms in MoS_2/Sb_2O_3/Au nanocomposite coatings. *Acta Materialia*, 58:4100–4109, 2010.

[106] S. Karthikeyan, H. J. Kim, and D. A. Rigney. Velocity and strain-rate profiles in materials subjected to unlubricated sliding. *Physical Review Letters*, 95:106001, 2005.

[107] D. A. Rigney, X. Y. Fu, J. E. Hammerberg, B. L. Holian, and M. L. Falk. Examples of structural evolution during sliding and shear of ductile materials. *Scripta Materialia*, 49:977–983, 2003.

[108] R. S. Goeke, S. V. Prasad, T. W. Scharf, and P. G. Kotula. Synthesis of MoS_2-Au nanocomposite films by sputter deposition. *Report No. SAND2012-5081*, 2012.

[109] Q. Ma and D. R. Clarke. Size dependent hardness of silver single crystals. *Journal of Materials Research*, 10:853–863, 1995.

[110] E. Atanassova, P. Lytvyn, S. N. Dub, R. V. Konakova, V. F. Mitin, and D. Spassov. Nanomechanical properties of pure and doped Ta_2O_5 and the effect of microwave irradiation. *Journal of Physics D: Applied Physics*, 45:475304, 2012.

[111] F. P. Bowden and D. Tabor. *The Friction and Lubrication of Solids*. Oxford University Press, New York, 2001.

[112] Y. Mo, K. T. Turner, and I. Szlufarska. Friction laws at the nanoscale. *Nature*, 457:1116–1119, 2009.

[113] J. A. Harrison, C. T. White, R. J. Colton, and D. W. Brenner. Molecular-dynamics simulations of atomic-scale friction of diamond surfaces. *Physical Review B*, 46:9700–9708, 1992.

[114] D. S. Stone, H. Gao, C. Chantharangsi, C. Paksunchai, M. Bischof, D. Jaeger, A. Martini, T. W. Scharf, and S. M. Aouadi. Load-dependent high temperature tribological properties of silver tantalate coatings. *Surface and Coatings Technology*, 244:37–44, 2014.

[115] S. G. Vilt, Z. Leng, B. D. Booth, C. McCabe, and G. K. Jennings. Surface and frictional properties of two-component alkylsilane monolayers and hydroxyl-terminated monolayers on silicon. *The Journal of Physical Chemistry C*, 113:14972–14977, 2009.

[116] J. Ou, J. Wang, S. Liu, J. Zhou, and S. Yang. Self-assembly and tribological property of a novel 3-layer organic film on silicon wafer with polydopamine coating as the interlayer. *The Journal of Physical Chemistry C*, 113:20429–20434, 2009.

[117] J. D. Schall, G. Gao, and J. A. Harrison. Effects of adhesion and transfer film formation on the tribology of self-mated DLC contacts. *The Journal of Physical Chemistry C*, 114:5321–5330, 2010.

[118] Y. Wang, M. Arai, T. Sasaki, and C. Wang. First-principles study of the (001) surface of cubic $CaTiO_3$. *Physical Review B*, 73:035411, 2006.

[119] S. P. Chen. Compositional and physical changes on perovskite crystal surfaces. *Journal of Materials Research*, 13:1848–1852, 1998.

[120] E. Heifets, W. A. Goddard, E. A. Kotomin, R. I. Eglitis, and G. Borstel. *Ab initio* calculations of the $SrTiO_3$ (110) polar surface. *Physical Review B*, 69:035408, 2004.

[121] A. Asthagiri and D. S. Sholl. First principles study of Pt adhesion and growth on SrO- and TiO_2-terminated $SrTiO_3$(100). *The Journal of Chemical Physics*, 116:9914–9925, 2002.

[122] H. Tanaka, H. Tabata, and T. Kawai. Probing the surface forces of atomic layered $SrTiO_3$ films by atomic force microscopy. *Thin Solid Films*, 342:4–7, 1999.

[123] G. T. Gao, P. T. Mikulski, and J. A. Harrison. Molecular-scale tribology of amorphous carbon coatings: Effects of film thickness, adhesion, and long-range interactions. *Journal of the American Chemical Society*, 124:7202–7209, 2002.

[124] Y. Morita, T. Shibata, T. Onodera, R. Sahnoun, M. Koyama, H. Tsuboi, N. Hatakeyama, A. Endou, H. Takaba, M. Kubo, C. A. Del Carpio, and A. Miyamoto. Effect of surface termination on superlow friction of diamond film: A theoretical study. *Japanese Journal of Applied Physics*, 47:3032–3035, 2008.

[125] J. Feng, W. Zhang, and W. Jiang. *Ab initio* study of Ag/Al_2O_3 and Au/Al_2O_3 interfaces. *Physical Review B*, 72:115423, 2005.

[126] R. Astala, M. Kaukonen, R. M. Nieminen, and T. Heine. Nanoindentation of silicon surfaces: Molecular-dynamics simulations of atomic force microscopy. *Physical Review B*, 61:2973–2980, 2000.

[127] R. Meyer, Q. Ge, J. Lockemeyer, R. Yeates, M. Lemanski, D. Reinalda, and M. Neurock. An *ab initio* analysis of adsorption and diffusion of silver atoms on alumina surfaces. *Surface Science*, 601:134–145, 2007.

[128] H. Gao, D. S. Stone, H. Mohseni, S. M. Aouadi, T. W. Scharf, and A. Martini. Mechanistic studies of high temperature friction reduction in silver tantalate. *Applied Physics Letters*, 102:121603, 2013.

[129] K. Nagao, J. B. Neaton, and N. W. Ashcroft. First-principles study of adhesion at Cu/SiO_2 interfaces. *Physical Review B*, 68:125403, 2003.

[130] D. S. Stone, H. Gao, C. Chantharangsi, C. Paksunchai, M. Bischof, A. Martini, and S. M. Aouadi. Reconstruction mechanisms of tantalum oxide coatings with low concentrations of silver for high temperature tribological applications. *Applied Physics Letters*, 105:191607, 2014.

[131] P. J. Kelly, H. Li, K. A. Whitehead, J. Verran, R. D. Arnell, and I. Iordanova. A study of the antimicrobial and tribological properties of TiN/Ag nanocomposite coatings. *Surface and Coatings Technology*, 204:1137–1140, 2009.

[132] P. J. Kelly, H. Li, P. S. Benson, K. A. Whitehead, J. Verran, R. D. Arnell, and I. Iordanova. Comparison of the tribological and antimicrobial properties of CrN/Ag, ZrN/Ag, TiN/Ag, and TiN/Cu nanocomposite coatings. *Surface and Coatings Technology*, 205:1606–1610, 2010.

[133] E. Silva, M. Rebelo de Figueiredo, R. Franz, R. E. Galindo, C. Palacio, A. Espinosa, V. S. Calderon, C. Mitterer, and S. Carvalho. Structure-property relations in ZrCN coatings for tribological applications. *Surface and Coatings Technology*, 205:2134–2141, 2010.

[134] J. L. Endrino, R. E. Galindo, H.-S. Zhang, M. Allen, R. Gago, A. Espinosa, and A. Anders. Structure and properties of silver-containing a-C(H) films deposited by plasma immersion ion implantation. *Surface and Coatings Technology*, 202:3675–3682, 2008.

[135] J. C. Sanchez-Lopez, M. D. Abad, I. Carvalho, R. E. Galindo, N. Benito, S. Ribeiro, M. Henriques, A. Cavaleiro, and S. Carvalho. Influence of silver content on the tribomechanical behavior on Ag-TiCN bioactive coatings. *Surface and Coatings Technology*, 206:2192–2198, 2012.

[136] R. E. Riecker and L. C. Towle. Shear strength of grossly deformed Cu, Ag, and Au at high pressures and temperatures. *Journal of Applied Physics*, 38:5189–5194, 1967.

[137] S. Xu, X. Gao, M. Hu, J. Sun, D. Wang, F. Zhou, L. Weng, and W. Liu. Morphology evolution of Ag alloyed WS_2 films and the significantly enhanced mechanical and tribological properties. *Surface and Coatings Technology*, 238:197–206, 2014.

[138] T. W. Scharf, A. Rajendran, R. Banerjee, and F. Sequeda. Growth, structure and friction behavior of titanium doped tungsten disulphide (Ti-WS_2) nanocomposite thin films. *Thin Solid Films*, 517:5666–5675, 2009.

[139] S. M. Aouadi, H. Gao, A. Martini, T. W. Scharf, and C. Muratore. Lubricious oxide coatings for extreme temperature applications: A review. *Surface and Coatings Technology*, 257:266–277, 2014.

[140] K. L. Strong and J. S. Zabinski. Tribology of pulsed laser deposited thin films of cesium oxythiomolybdate (Cs_2MoOS_3). *Thin Solid Films*, 406:174–184, 2002.

[141] W. Gulbinski, T. Suszko, W. Sienicki, and B. Warcholinski. Tribological properties of silver- and copper-doped transition metal oxide coatings. *Wear*, 254:129–135, 2003.

[142] S. M. Aouadi, D. P. Singh, D. S. Stone, K. Polychronopoulou, F. Nahif, C. Rebholz, C. Muratore, and A. A. Voevodin. Adaptive VN/Ag nanocomposite coatings with lubricious behavior from 25 to 1000 °C. *Acta Materialia*, 58:5326–5331, 2010.

[143] X.-S. Liang, J.-H. Ouyang, Z.-G. Liu, and Z.-L. Yang. Friction and wear characteristics of $BaCr_2O_4$ ceramics at elevated temperatures in sliding against sintered alumina ball. *Tribology Letters*, 47:203–209, 2012.

[144] M. A. Baker, P. J. Kench, M. C. Joseph, C. Tsotsos, A. Leyland, and A. Matthews. The nanostructure and mechanical properties of PVD CrCu (N) coatings. *Surface and Coating Technology*, 162:222–227, 2003.

[145] J. L. He, Y. Setsuhara, I. Shimizu, and S. Miyake. Structure refinement and hardness enhancement of titanium nitride films by addition of copper. *Surface and Coating Technology*, 137:38–42, 2001.

[146] H. S. Myung, H. M. Lee, L. R. Shaginyan, and J. G. Han. Microstructure and mechanical properties of Cu doped TiN superhard nanocomposite coatings. *Surface and Coating Technology*, 163-164:591–596, 2003.

[147] J. G. Han, H. S. Myung, H. M. Lee, and L. R. Shaginyan. Microstructure and mechanical properties of Ti-Ag-N and Ti-Cr-N superhard nanostructured coatings. *Surface and Coating Technology*, 174-175:738–743, 2003.

[148] S. Duguey, R. Lebourgeois, C. Grattepain, J.-M. Heintz, and J.-P. Ganne. Study of copper substitutions in $Ag(Nb_xTa_{1-x})O_3$ solid solutions. *Journal of the European Ceramic Society*, 27:1171–1175, 2007.

[149] A. W. Sleight and C. T. Prewitt. Preparation of $CuNbO_3$ and $CuTaO_3$ at high pressure. *Materials Research Bulletin*, 5:207–211, 1970.

[150] J. M. Longo and A. W. Sleight. $CuTa_2O_6$–crystal growth and characterization. *Materials Research Bulletin*, 10:1273–1277, 1975.

[151] H. Yoshizawa, Y. Chen, and J. Israelachvili. Fundamental mechanisms of interfacial friction. 1. Relation between adhesion and friction. *Journal of Physical Chemistry*, 97:4128–4140, 1993.

[152] M. Hirano and K. Shinjo. Atomistic locking and friction. *Physical Review B*, 41:11837–11851, 1990.

[153] M. H. Muser, L. Wenning, and M. O. Robbins. Simple microscopic theory of amontons's laws for static friction. *Physical Review Letters*, 86:1295–1298, 2001.

[154] M. H. Muser. Structural lubricity: Role of dimension and symmetry. *Europhysics Letters*, 66:97–103, 2004.

[155] M. H. Muser and M. O. Robbins. Conditions for static friction between flat crystalline surfaces. *Physical Review B*, 61:2335–2342, 2000.

[156] M. Peyrard and S. Aubry. Critical behaviour at the transition by breaking of analyticity in the discrete frenkel-kontorova model. *Journal of Physics C: Solid State Physics*, 16:1593–1608, 1983.

[157] T. Filleter, W. Paul, and R. Bennewitz. Atomic structure and friction of ultrathin films of KBr on Cu(100). *Physical Review B*, 77:035430, 2008.

[158] A. Erdemir, R. A. Erck, and J. Robles. Relationship of hertzian contact pressure to friction behavior of self-lubricating boric acid films. *Surface and Coatings Technology*, 49:435–438, 1991.

[159] F. Gao, O. Furlong, P. V. Kotvis, and W. T. Tysoe. Pressure dependence of shear strengths of thin films on metal surfaces measured in ultrahigh vacuum. *Tribology Letters*, 31:99–106, 2008.

[160] M. H. Muser. Lubricants under high local pressure: Liquids act like solids. *Materialwissenschaft und Werkstofftechnik*, 35:603–609, 2004.

[161] B. J. Briscoe and D. C. B. Evans. The shear properties of langmuir-blodgett layers. *Proceedings of the Royal Society of London A: Mathematical, Physical and Engineering Sciences*, 380:389–407, 1982.

[162] M. Garvey, O. J. Furlong, M. Weinert, and W. T. Tysoe. Shear properties of potassium chloride films on iron obtained using density functional theory. *Journal of Physics: Condensed Matter*, 23:265003, 2011.

[163] L. Prandtl. Ein gedankenmodell zur kinetischen theorie der festen korper. *Journal of Applied Mathematics and Mechanics*, 8:85–106, 1928.

[164] G. A. Tomlinson. CVI. a molecular theory of friction. *Philosophical Magazine Series 7*, 7:905–939, 1929.

[165] E. Gnecco, R. Bennewitz, A. Socoliuc, and E. Meyer. Friction and wear on the atomic scale. *Wear*, 254:859–862, 2003.

[166] C. Fusco and A. Fasolino. Velocity dependence of atomic-scale friction: A comparative study of the one- and two-dimensional tomlinson model. *Physical Review B*, 71:045413, 2005.

[167] O. J. Furlong, S. J. Manzi, V. D. Pereyra, V. Bustos, and W. T. Tysoe. Monte carlo simulations for tomlinson sliding models for non-sinusoidal periodic potentials. *Tribology Letters*, 39:177–180, 2010.

[168] M. H. Muser. Velocity dependence of kinetic friction in the Prandtl-Tomlinson model. *Physical Review B*, 84:125419, 2011.

[169] J. A. Harrison and D. W. Brenner. Simulated tribochemistry: An atomic-scale view of the wear of diamond. *Journal of the American Chemical Society*, 116:10399–10402, 1994.

[170] D. W. Brenner, O. A. Shenderova, J. A. Harrison, S. J. Stuart, B. Ni, and S. B. Sinnott. A second-generation reactive empirical bond order (REBO) potential energy expression for hydrocarbons. *Journal of Physics: Condensed Matter*, 14:783–802, 2002.

[171] J. A. Harrison, G. Gao, J. D. Schall, M. T. Knippenberg, and P. T. Mikulski. Friction between solids. *Philosophical Transactions of the Royal Society of London A: Mathematical, Physical and Engineering Sciences*, 366:1469–1495, 2008.

[172] Y. Dong, Q. Li, J. Wu, and A. Martini. Friction, slip and structural inhomogeneity of the buried interface. *Modelling and Simulation in Materials Science and Engineering*, 19:065003, 2011.

[173] B. S. Sinnott, S.-J. Heo, W. D. Brenner, and A. J. Harrison. *Nanotribology and Nanomechanics: An Introduction*. Springer, Berlin-Heidelberg, 2008.

[174] I. Szlufarska, M. Chandross, and R. W. Carpick. Recent advances in single-asperity nanotribology. *Journal of Physics D: Applied Physics*, 41:123001, 2008.

[175] M. A. Van Hove and S. Y. Tong. *Surface crystallography by LEED: Theory, computation, and structural results*. Springer, New York, 1979.

[176] H. Zhang, J. R. Rustad, and J. F. Banfield. Interaction between water molecules and zinc sulfide nanoparticles studied by temperature-programmed desorption and molecular dynamics simulations. *The Journal of Physical Chemistry A*, 111:5008–5014, 2007.

[177] M. J. L. Sangster and M. Dixon. Interionic potentials in alkali halides and their use in simulations of the molten salts. *Advances in Physics*, 25:247–342, 1976.

[178] M. C. C. Ribeiro. Chemla effect in molten LiCl/KCl and LiF/KF mixtures. *The Journal of Physical Chemistry B*, 107:4392–4402, 2003.

[179] M. S. Daw and M. I. Baskes. Embedded-atom method: Derivation and application to impurities, surfaces, and other defects in metals. *Physical Review B*, 29:6443–6453, 1984.

[180] M. S. Daw and M. I. Baskes. Semiempirical, quantum mechanical calculation of hydrogen embrittlement in metals. *Physical Review Letters*, 50:1285–1288, 1983.

[181] M. I. Mendelev, S. Han, D. J. Srolovitz, G. J. Ackland, D. Y. Sun, and M. Asta. Development of new interatomic potentials appropriate for crystalline and liquid iron. *Philosophical Magazine*, 83:3977–3994, 2003.

[182] M. Garvey, M. Weinert, and W. T. Tysoe. On the pressure dependence of shear strengths in sliding, boundary-layer friction. *Tribology Letters*, 44:67–73, 2011.

[183] M. Garvey, M. Weinert, and W. T. Tysoe. On the film thickness dependence of shear strengths in sliding, boundary-layer friction. *Wear*, 274275:281–285, 2012.

[184] M. R. Sorensen, K. W. Jacobsen, and P. Stoltze. Simulations of atomic-scale sliding friction. *Physical Review B*, 53:2101–2113, 1996.

[185] S. A. Chambers. Epitaxial growth and properties of thin film oxides. *Surface Science Reports*, 39:105–180, 2000.

[186] Y. J. Shin, R. Stromberg, R. Nay, H. Huang, A. T. S. Wee, H. Yang, and C. S. Bhatia. Frictional characteristics of exfoliated and epitaxial graphene. *Carbon*, 49:4070–4073, 2011.

[187] F. Gao, P. V. Kotvis, and W. T. Tysoe. The frictional properties of thin inorganic halide films on iron measured in ultrahigh vacuum. *Tribology Letters*, 15:327–332, 2003.

[188] R. Bennewitz, M. Bammerlin, M. Guggisberg, C. Loppacher, A. Baratoff, E. Meyer, and H.-J. Gntherodt. Aspects of dynamic force microscopy on NaCl/Cu(111): resolution, tip-sample interactions and cantilever oscillation characteristics. *Surface and Interface Analysis*, 27:462–466, 1999.

[189] R. Bennewitz, S. Schar, E. Gnecco, O. Pfeiffer, M. Bammerlin, and E. Meyer. Atomic structure of alkali halide surfaces. *Applied Physics A*, 78:837–841, 2004.

[190] P. Steiner, E. Gnecco, T. Filleter, N. N. Gosvami, S. Maier, E. Meyer, and R. Bennewitz. Atomic friction investigations on ordered superstructures. *Tribology Letters*, 39:321–327, 2010.

[191] P. Steiner, R. Roth, E. Gnecco, A. Baratoff, and E. Meyer. Angular dependence of static and kinetic friction on alkali halide surfaces. *Physical Review B*, 82:205417, 2010.

[192] Y. Namai and H. Shindo. Frictional force microscopic anisotropy on (001) surfaces of alkali halides and MgO. *Japanese Journal of Applied Physics*, 39:4497–4500, 2000.

[193] D. Olson, H. Gao, C. Tang, W. T. Tysoe, and A. Martini. Pressure dependence of the interfacial structure of potassium chloride films on iron. *Thin Solid Films*, 593:150–157, 2015.

[194] H. Spikes and W. T. Tysoe. On the commonality between theoretical models for fluid and solid friction, wear and tribochemistry. *Tribology Letters*, 59:1–14, 2015.

[195] Y. Dong, A. Vadakkepatt, and A. Martini. Analytical models for atomic friction. *Tribology Letters*, 44:367–386, 2011.

[196] E. Riedo, E. Gnecco, R. Bennewitz, E. Meyer, and H. Brune. Interaction potential and hopping dynamics governing sliding friction. *Physical Review Letters*, 91:084502, 2003.

[197] O. J. Furlong, S. J. Manzi, A. Martini, and W. T. Tysoe. Influence of potential shape on constant-force atomic-scale sliding friction models. *Tribology Letters*, 60:1–9, 2015.

[198] R. Komanduri, N. Chandrasekaran, and L. M. Raff. MD simulation of indentation and scratching of single crystal aluminum. *Wear*, 240:113–143, 2000.

[199] R. Komanduri, N. Chandrasekaran, and L. M. Raff. Molecular dynamics (MD) simulation of uniaxial tension of some single-crystal cubic metals at nanolevel. *International Journal of Mechanical Sciences*, 43:2237–2260, 2001.

[200] W. C. Oliver and G. M. Pharr. An improved technique for determining hardness and elastic modulus using load and displacement sensing indentation experiments. *Journal of Materials Research*, 7:1564–1583, 1992.

[201] Q. Li, Y. Dong, D. Perez, A. Martini, and R. W. Carpick. Speed dependence of atomic stick-slip friction in optimally matched experiments and molecular dynamics simulations. *Physical Review Letters*, 106:126101, 2011.

[202] E. Gnecco, R. Bennewitz, T. Gyalog, C. Loppacher, M. Bammerlin, E. Meyer, and H.-J. Guntherodt. Velocity dependence of atomic friction. *Physical Review Letters*, 84:1172–1175, 2000.

[203] Y. Dong, H. Gao, and A. Martini. Suppression of atomic friction under cryogenic conditions: The role of athermal instability in AFM measurements. *Europhysics Letters*, 98:16002, 2012.

[204] L. Jansen, H. Holscher, H. Fuchs, and A. Schirmeisen. Temperature dependence of atomic-scale stick-slip friction. *Physical Review Letters*, 104:256101, 2010.

[205] I. Barel, M. Urbakh, L. Jansen, and A. Schirmeisen. Multibond dynamics of nanoscale friction: The role of temperature. *Physical Review Letters*, 104:066104, 2010.

[206] H. M. Andersson, M. W. Keller, J. S. Moore, N. R. Sottos, and S. White. *Self Healing Materials: An Alternative Approach to 20 Centuries of Materials Science*. Springer Netherlands, Dordrecht, 2007.

[207] P. P. Ewald. *Crystal structures, Supplement V* by R. W. G. Wyckoff. *Acta Crystallographica*, 15:173–174, 1962.

[208] S. Grazulis, D. Chateigner, R. T. Downs, A. F. T. Yokochi, M. Quiros, L. Lutterotti, E. Manakova, J. Butkus, P. Moeck, and A. Le Bail. Crystallography Open Database – an open-access collection of crystal structures. *Journal of Applied Crystallography*, 42:726–729, 2009.

[209] J. S. Zabinski, J. H. Sanders, J. Nainaparampil, and S. V. Prasad. Lubrication using a microstructurally engineered oxide: Performance and mechanisms. *Tribology Letters*, 8:103–116, 2000.

[210] P. A. Redhead. Thermal desorption of gases. *Vacuum*, 12:203–211, 1962.

[211] M. W. Chase. NIST-JANAF thermochemical tables. *Journal of Physical and Chemical Reference Data*, Monograph No. 9, 1998.

Appendix A

Appendices

A.1 $AgTaO_3$ MEAM Parameters

Table A.1: MEAM parameters Ag, Ta and O. All values are taken from previous work [3] except $\alpha, \beta^{(0)}, \beta^{(1)}$ and $\beta^{(2)}$ for Oxygen.

	E_c(eV)	a_0(Å)	A	α	$\beta^{(0)}$	$\beta^{(1)}$	$\beta^{(2)}$	$\beta^{(3)}$	$t^{(0)}$	$t^{(1)}$	$t^{(2)}$	$t^{(3)}$
Ag	2.850	2.88	1.06	5.89	4.46	2.2	6.0	2.2	1	5.54	2.45	1.29
Ta	8.089	2.86	0.99	4.90	3.71	1.0	1.0	1.0	1	4.69	3.35	-1.50
O	2.558	1.21	1.50	6.49	4.59	4.59	4.59	-	1	0.09	0.10	0.00

Table A.2: Properties of FCC Ag and BCC Ta predicted using MEAM parameters in table A.1 and compared to experimental values [4].

	FCC Ag		BCC Ta	
	MEAM	Expt.	MEAM	Expt.
a (Å)	4.09	4.09	3.31	3.31
E_c (eV)	-2.85	-2.95	-8.09	-8.10
C_{11} (GPa)	124.17	131.50	262.30	266.30
C_{12} (GPa)	93.53	97.30	156.18	158.20
B (GPa)	103.74	108.70	191.55	194.23

Table A.3: MEAM parameters for the binaries optimized to describe $AgTaO_3$. For all binaries, the structure is B1 and the cut off distance is 6.2 Å. The ternary screening parameters for all combinations of elements are C_{min}=2.0 and C_{max}=2.8. For the ratio ρ_0^1/ρ_0^2, superscripts 1 and 2 indicate the first and second element listed in the binary pair, respectively.

	Ag-O	Ta-O	Ag-Ta
ρ_0^1/ρ_0^2	0.14	0.26	0.54
E_c	2.985	6.845	-
r_e	2.274	2.202	2.660
α	6.274	5.085	5.060
ΔH_{B1}	-	-	-0.100

A.2 DFT-Calculated Material Properties for $AgTaO_3$

The research reported in this section was performed by our colleagues *A. Otero-de-la-Roza and E.R. Johnson*. The equilibrium lattice parameters and elastic constants of AgO and TaO (in their cubic B1 structures) are shown in table 2.1. To our knowledge, no experimental data exists on the B1 phase of AgO, but calculations indicate that it is a (meta)stable phase. In the case of TaO, the B1 phase has been observed experimentally [207, 208] and our cubic lattice constant (4.404 Å) agrees with experiment (4.42 Å), although the calculated C_{44} elastic constant (83.8 GPa) shows that it is predicted to be unstable to a rhombohedral deformation. The PBE cohesive energies per atom are also shown in table 2.1.

The equilibrium structure of the ternary system ($AgTaO_3$) is in very close agreement with experimental results. The structure is correctly predicted to be rhombohedral with only a slight deviation from the cubic symmetry. The primitive (rhombohedral) cell parameters are a = 5.55 Å and = 58.58°, to be compared to the experimental values [82] a = 5.58 Å and α = 59.43°. The structural properties in the cubic-like conventional cell are shown in table 2.2. The reason for the deviation from the cubic setting is a relative rotation of the octahedra, common to many perovskites, and is depicted in figure 2.1(c). Rotation of octahedra also explains the experimentally observed increase in symmetry at higher temperatures. The cohesive energy is 6.29 eV per atom, intermediate between AgO and TaO.

A.3 Complementary Experimental Results on Surface Termination Study

The research reported in this section was performed by our colleagues *S.M. Aouadi et al.*. Experimentally, a Model 670xi Scanning Auger Nanoprobe was subsequently used to determine the elemental composition inside and outside the wear track (the region of the surface worn away due to sliding). Figure A.1 shows the elemental composition scans for a sample tested under a 10 N load at 1023 K. Elemental maps measured using Auger electron spectroscopy (AES) in selected regions are shown as insets (a) and (b) in figure A.1. The corresponding measured elemental compositions are given next to the AES maps (insets (c) and (d)). These results reveal an increase in silver content closer to the edge of the track and a decrease in the amount of silver observed in the middle of the track. This suggests that friction is closely related to the wear of the materials surface and that wear results in a redistribution of silver. Our calculations, discussed in Section 5.3.1, confirm the picture of soft silver aggregates being formed by the additional mechanical energy and pushed by the probe to the edges of the wear track [48, 128].

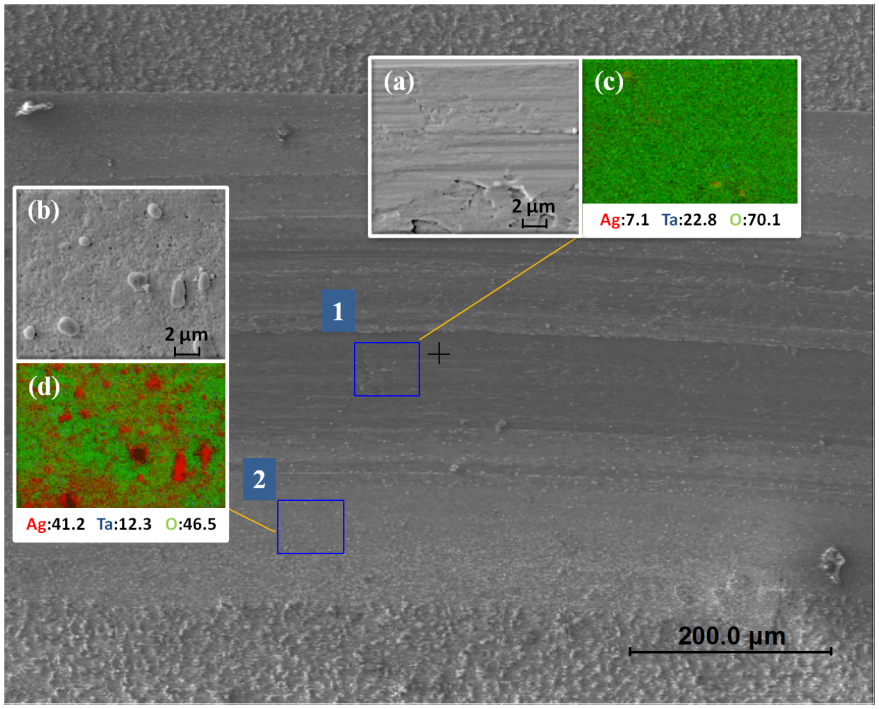

Figure A.1: Scanning Auger Nanoprobe images taken after sliding; wear tests were performed at 1023 K with a load of 10 N. Insets (a) and (b) are elemental maps measured by Auger electron spectroscopy in regions 1 and 2; insets (c) and (d) show percentage elemental compositions corresponding to the selected regions.

A.4 DFT-Calculated Potential Energy Surface and Binding Energy for AgO- and TaO_2-Terminated Surfaces

The research reported in this section was performed by our colleagues *A. Otero-de-la-Roza and E.R. Johnson*. Potential energy surfaces for migration of Ag on the AgO and TaO_2 surfaces from DFT are shown in figure A.2. The minimum energy configurations and shapes of the potential energy surfaces agree with those obtained using MD, except in that the Ag atom prefers being close, but not on top of, the O on the AgO surface. The results demonstrate that Ag migration on either surface is relatively facile, with barriers equal to 0.13 eV (AgO) and 0.17 eV (TaO_2). Sliding of Ag on AgO is easier than on TaO_2, which is consistent with the discussion in Section 5.3.3 and the observed frictional behavior of both surfaces. These results are in fair agreement with the MD energy landscapes in figure 5.7, although the barriers are significantly higher. The consistency is reassuring regarding the soundness of the potential used in the MD simulations. The calculated DFT barriers correspond to thermal energies in the range 1150-2300 K, which is consistent with experiment. Ag migration is also expected to be facilitated when the surface is subject to mechanical wear. Therefore, the barriers predicted by DFT and MD are in agreement with the observed formation of Ag clusters in the wear track from both experiment and MD. The ability of Ag to slide on both surfaces is not surprising, given the stability of the Ta octahedral motif, and the low formal charge on the Ag cation in the perovskite, which can also explain its tendency to aggregate.

DFT calculations of the binding energies show that a silver atom binds more strongly to the AgO surface than to the TaO_2 surface, although both adsorptions are favorable. The binding energies for Ag are 4.14 eV on AgO and 2.75 eV on TaO_2. Thus, Ag prefers to bind anywhere on the AgO surface (even at the least favorable site, directly on top of the surface Ag) than to the most favorable sites on the TaO_2 surface. This is consistent with the observed formation of Ag clusters. Silver aggregation is favored by the formation of metallic silver on the surface, which in turn is aided by the low formal charge of the silver atoms in $AgTaO_3$.

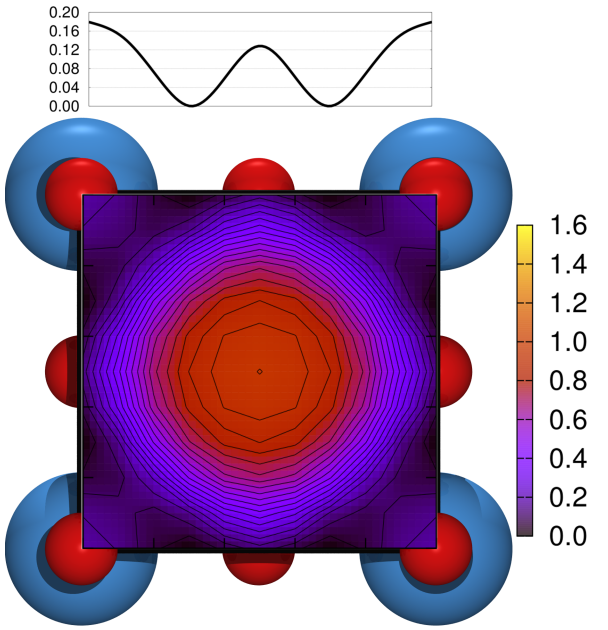

(a)

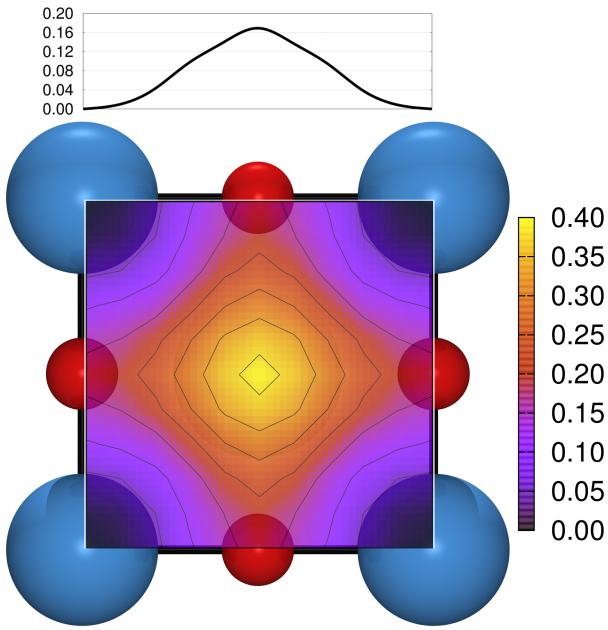

(b)

Figure A.2: Potential energy surfaces for Ag migration on AgO (left) and TaO_2 (right) surfaces. Energy are in eV and the scales are the same as those in figure 5.7.

A.5 Cu-Ta-O MEAM Parameters

Table A.4: MEAM parameters for Cu, Ta and O were taken from previous work [3].

	E_c(eV)	a_0(Å)	A	α_{edf}	$\beta^{(0)}$	$\beta^{(1)}$	$\beta^{(2)}$	$\beta^{(3)}$	$t^{(0)}$	$t^{(1)}$	$t^{(2)}$	$t^{(3)}$
Cu	3.54	3.62	1.07	5.11	3.63	2.20	6.00	2.20	1.00	4.37	2.49	2.95
Ta	8.09	3.30	0.99	4.90	3.71	1.00	1.00	1.00	1.00	6.09	3.35	-2.90
O	2.56	1.21	1.50	4.59	4.59	4.59	4.59	4.59	1.00	0.09	0.10	0.00

Table A.5: MEAM parameters for the binaries optimized to describe $CuTaO_3$ and $CuTa_2O_6$. For all binaries, the structure is B1 and the cut off distance is 6.2 Å. For the ratio ρ_0^1/ρ_0^2, superscripts 1 and 2 indicate the first and second element listed in the binary pair, respectively.

Parameter	Cu-O	Ta-O	Cu-Ta ($CuTaO_3$)	Cu-Ta ($CuTa_2O_6$)
ρ_0^1/ρ_0^2	0.025	0.704	0.035	0.035
E_c	4.530	8.650	-	-
r_e	2.064	2.205	5.895	7.189
α_{edf}	4.992	4.415	4.448	2.663
r_c	-	-	6.200	6.200
C_{max}	-	-	2.8	0.6
C_{min}	-	-	0.0	0.0

A.6 Experimental Characterization on $CuTa_2O_6$ Surface

The research reported in this section was performed by our colleagues *J. Gu, D.S. Stone and S.M. Aouadi*. The composition of the tribofilm is altered by the process of surface restructuring during contact sliding, which results in a change of the tribological performance of the lubricant material with increasing wear. To investigate this effect, figure A.3(a) shows the elemental mapping in the vicinity of the wear track in addition to a scanning electron microscope (SEM) micrograph of the selected region. The Cu content, shown in figure A.3(b), was found to decrease dramatically in the wear track as a result of the sliding process; the Ta content, shown in figure A.3(c), accumulated at the edges of the wear track. The observed elemental mapping is likely caused by formation of Cu or copper oxide clusters due to the dissociation of the $CuTa_2O_6$ phase in the wear track, in agreement with the simulations discussed in the following section. This ternary phase dissociation was less pronounced than in the $AgTaO_3$ coatings [2], since the Cu-O bonds are stronger than the Ag-O bonds and the energy that is required to decompose $CuTa_2O_6$ into binary oxides is much higher. Finally, the presence of a transfer film was confirmed by Raman spectroscopy, which was carried out on the Si_3O_4 ball after high-temperature sliding tests. This material transfer is consistent with observations on other ternary oxide materials that we and other authors have studied [139, 142, 209].

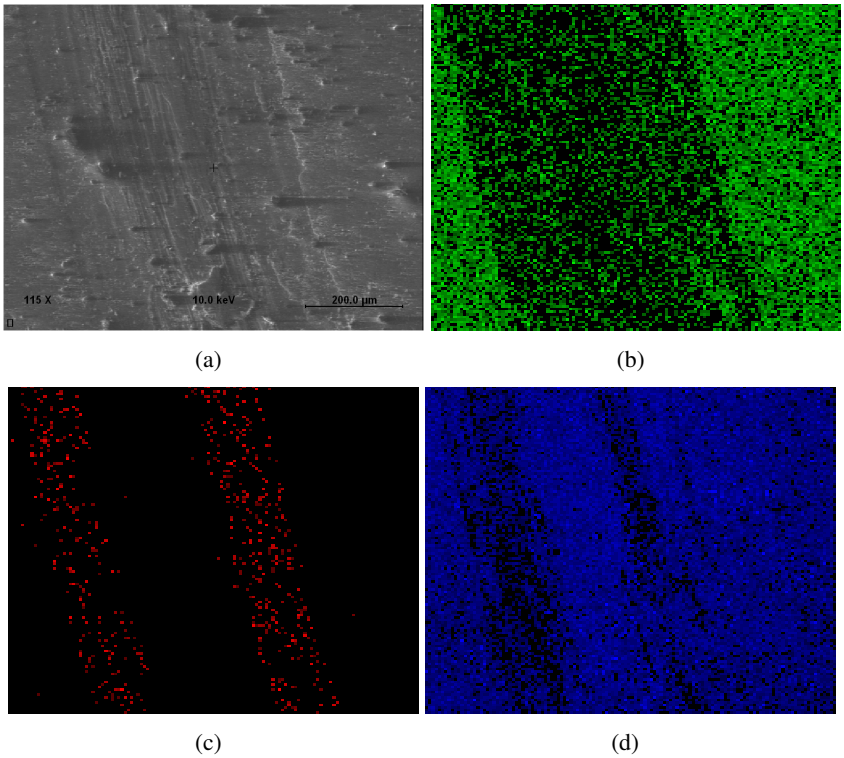

Figure A.3: Characterization of a selected area of the wear track after tribotesting at 750 °C. (a) SEM image and elemental mapping of (b) Copper, (c) Tantalum, and (d) Oxygen.

A.7 DFT-Calculated Ag/Cu Migration Energy

The research reported in this section was performed by our colleagues *A. Otero-de-la-Roza and E.R. Johnson*. Our DFT calculations indicate that the sliding of Cu on $CuTaO_3$ is more difficult than Ag on $AgTaO_3$. Figure A.4 shows the potential energy surfaces (PES) for the sliding of Cu on CuO-terminated $CuTaO_3$ and Ag on AgO-terminated $AgTaO_3$. The features of both PES are essentially the same: the energy minimum is located at the voids along the edges of the cell and the least-stable configuration is located above the underlying metal atoms. However, the energy barriers for the migration of Cu between minima are much higher than for Ag (by roughly a factor of 3), which suggests that the formation of metal aggregates responsible for lowering friction is not as facile as for $AgTaO_3$. This explains both its higher friction and its increased resistance to wear. Since $CuTa_2O_6$ is essentially isostructural to $CuTaO_3$ but with a lower Cu content, the difficulty in forming the metallic aggregates is increased by the lower availability of Cu at the surface.

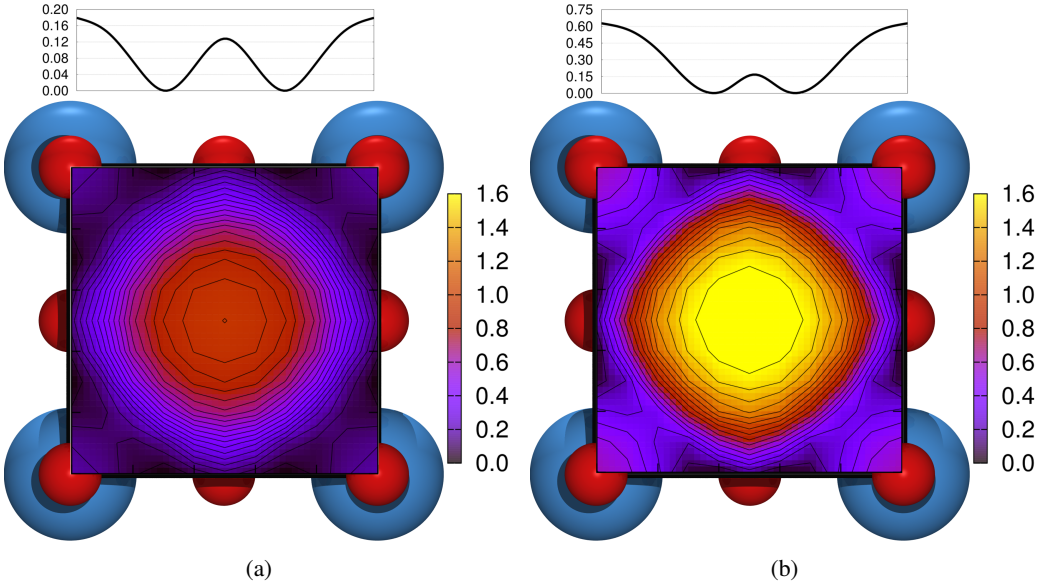

(a) (b)

Figure A.4: Potential energy surfaces for sliding Ag on a AgO-terminated $AgTaO_3$ surface (left) and of Cu on a CuO-terminated $CuTaO_3$ surface (right). The surface metal atom (Ag or Cu) occupies the center of the square. The energy scale for the colormap is the same; the units are eV. The data for $AgTaO_3$ is the same as in our previous work [2], but on a different energy scale.

A.8 Temperature-Programmed Desorption (TPD) Experiments in the Activation Energy Calculation

The research reported in this section was performed by our colleagues *D. Olson and W.T. Tysoe*. A series of temperature-programmed desorption data for KCl evaporated onto Fe(100) at 300 K collected using a heating rate of 5 K/s are displayed in figure A.5(a) while monitoring 39 amu. The desorption profiles are asymmetric indicating a desorption order of unity or less [210] and show a peak temperature that increases as a function of film thickness from ~639 K for the thinnest films up to ~690 K for a thick KCl layer. The inset to figure A.5(a) shows the integrated peak areas for each of the desorption profiles plotted versus the initial film thickness. The linearity of the plot indicates that KCl adsorbs with a constant sticking probability and that a constant flux is provided by the KCl dosing source.

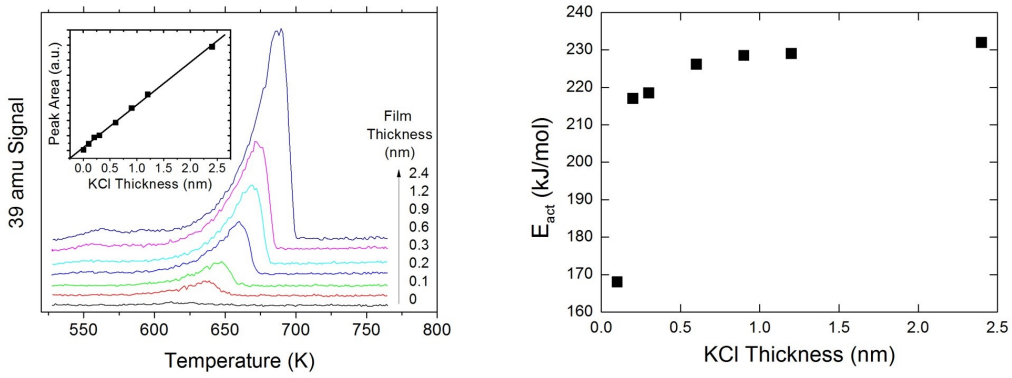

(a) (b)

Figure A.5: (a): Temperature-programmed desorption data collected by monitoring 39 amu for KCl adsorbed on a Fe(100) surface at 300 K collected using a heating rate of 5 K/s as a function of KCl film thickness. The inset shows a plot of the integrated peak area as a function of film thickness. (b) Plot of desorption activation energy as a function of films thickness obtained by fitting the desorption profiles shown in figure A.5(a).

The TPD data were fit by numerically integrating the rate equation:

$$-\frac{d\theta}{dt} = A\theta^n exp(-\frac{E_{act}(\theta)}{k_B T}) \tag{A.1}$$

where A is a pre-exponential factor, θ the coverage, n the reaction order, $E_{act}(\theta)$ the coverage-dependent desorption activation energy, k_B the Boltzmann constant and T, the temperature. The fit was carried out over small temperature steps using the measured linear heating rate, β = 5 K/s to yield:

$$-\frac{d\theta}{dT} = \frac{A}{\beta}\theta^n exp(-\frac{E_{act}(\theta)}{k_B T}) \tag{A.2}$$

The size of the temperature step was decreased until no changes in the fitting parameters were observed to ensure that the numerical integration of equation A.2 was accurate. The values

of A, n and $E_{act}(\theta)$ were systematically adjusted to provide the best fit to each desorption profile by minimizing the standard deviation between the theoretical fit and the experimental data. The reaction order n was found to be 0.5 ± 0.1 suggesting that desorption takes place on the perimeters of KCl patches on the surface. The resulting values of the desorption activation energies as a function of film thickness are displayed in figure A.5(b). This initially increases rapidly from a value of ~130 kJ/mol for the thinnest films, rising rapidly with increasing film thickness to reach an almost constant value of ~230 kJ/mol for films thicker than ~0.8 nm, in reasonable agreement with the heat of sublimation of KCl [211].

A.9 Low-Energy Electron Diffraction (LEED) Patterns

The research reported in this section was performed by our colleagues *D. Olson and W.T. Tysoe*. Low-energy electron diffraction images were obtained for thin KCl films to avoid sample charging, which was further minimized by keeping the beam current as low as possible. Figure A.6(a) shows the LEED pattern for clean Fe(100) collected using a beam energy of ~50 eV. This displays a square pattern expected of the Fe(100) face and is used to calibrate the spacing of KCl films using the standard lattice constant for Fe of 0.287 nm [4].

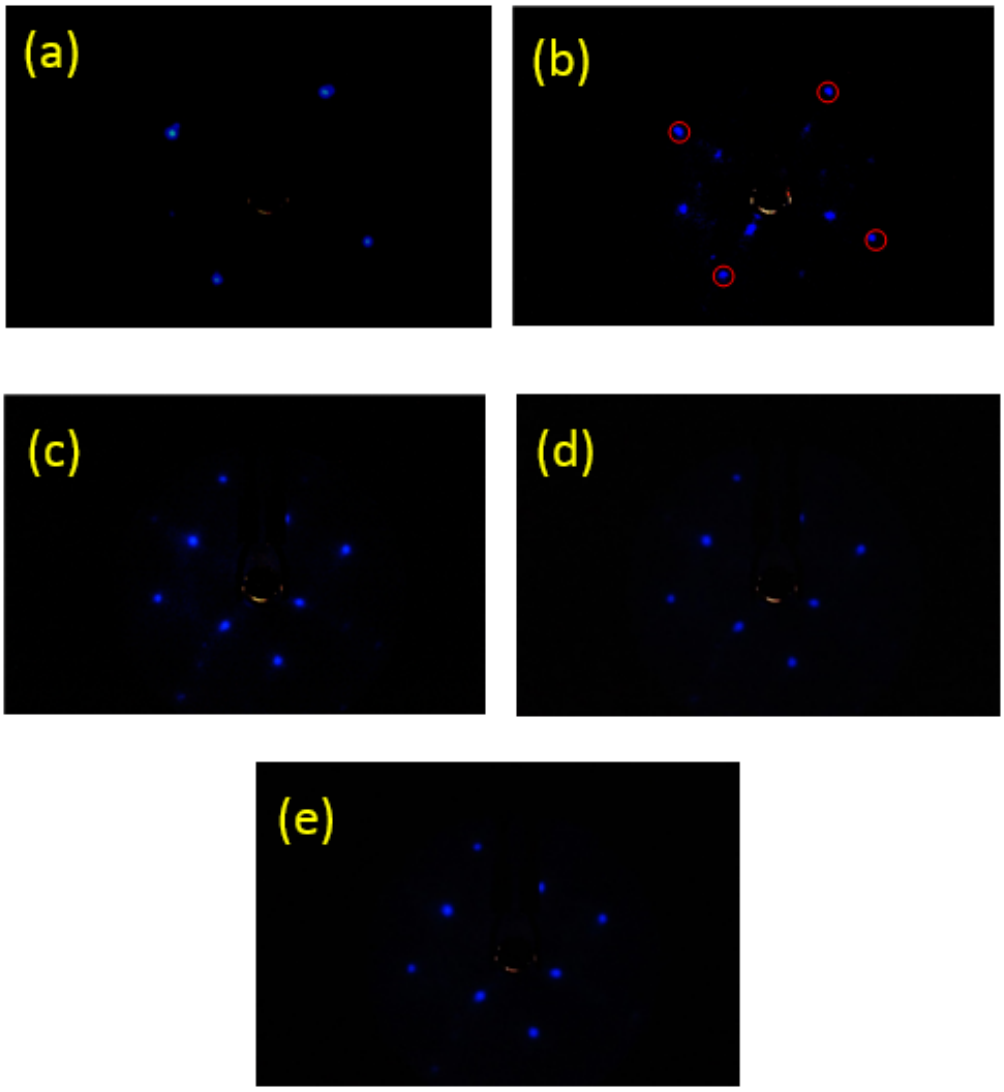

Figure A.6: LEED patterns collected using a beam energy of 50 eV for (a): a clean Fe(100) surface, (b) 1 ML of KCl on Fe(100). The spots due to the Fe(100) substrate are circled in red, while the additional features are due to KCl. (c) 2 ML of KCl of Fe(100) (d) 3 ML of KCl on Fe(100) and (e) 4 ML of KCl on Fe(100). The substrate spots are no longer visible in the last three diffraction patterns and the spots are due only to the KCl film.

Figure A.6(b) shows the corresponding LEED pattern for 1 monolayer (ML) of KCl deposited onto iron at ~500 K, also collected using the same beam energy of 50 eV, showing both the Fe(100) substrate spots and those due to KCl. Here the substrate spots are circled in red and yield the same spot spacing as in figure A.5(a) confirming that identical electron beam energies were used in both cases. The additional spots due to KCl are aligned with the Fe(100) substrate. Comparing the spot spacings with those of the underlying Fe(100) substrate gives the lattice constant for the KCl monolayer to yield a K-K (or Cl-Cl) distance of 0.48 ± 0.01 nm (compared with 0.4449 nm for pure KCl) [4]. This suggests that the first layer KCl is slightly expanded compared to the bulk KCl lattice.

Figure A.6(c-e) display the LEED pattern from two, three and four monolayers of KCl on Fe(100), again collected using a beam energy of 50 eV, where now the Fe(100) substrate diffraction spots are obscured. The LEED patterns are slightly distorted since the electron beam is not normal to the surface. However, the spacings between the diffraction spots are identical for all three films indicating that a bulk-like KCl film is formed when the film thickness is greater than or equal to two monolayers. In addition, the measured spot spacings are consistent with the bulk lattice structure of KCl. This implies that the interaction potential between the KCl film and the underlying Fe(100) lattice is small since a two-layer film of KCl provides sufficient elastic energy to overcome the small lattice distortion (of ~7 %) found for the first monolayer. Note that even the distorted first-monolayer film is not in registry with the substrate.